Coordination among proteins, lipids and water in membrane fusion and fission probed by solid-state NMR

by

Madeleine Sutherland

B.A. Biochemistry
Smith College, 2016

SUBMITTED TO THE DEPARTMENT OF CHEMISTRY IN PARTIAL FULFILLMENT OF THE REQUIREMENTS FOR THE DEGREE OF

DOCTOR OF PHILOSOPHY IN CHEMISTRY
AT THE
MASSACHUSETTS INSTITUTE OF TECHNOLOGY

May 2022

Signature of Author: _____
Department of Chemistry
December 2, 2021

Certified by: _____
Mei Hong
Professor of Chemistry
Thesis Supervisor

Accepted by: _____
Adam Willard
Associate Professor
Graduate Officer

This doctoral thesis has been examined by a committee of the

Department of Chemistry as follows:

Professor Adam Willard ……....
Thesis Committee Chair
Associate Professor of Chemistry

Professor Mei Hong ……...
Thesis Supervisor
Professor of Chemistry

Professor Laura Kiessling …….
Novartis Professor of Chemistry

Coordination among proteins, lipids and water in membrane fusion and fission probed by solid-state NMR

by

Madeleine Sutherland

Submitted to the Department of Chemistry
on December 2, 2021 in Partial Fulfillment of the
Requirements for the Degree of Doctor of Philosophy in
Chemistry

Abstract

For enveloped viruses such as HIV, influenza, and coronaviruses to enter host cells, the viral and cell envelopes must be fused together. Then, to exit the cell, a new virus particle will pinch off a piece of the host cell membrane. The two membranes must be physically separated to release the virus particle. This process is called “scission” in the context of viral exit and “fission” when simply discussing membrane division.

Viral membrane remodeling proteins catalyze membrane fusion and fission to bring about viral entry and exit from host cells – vital processes in the life cycle of enveloped viruses. The exact mechanism by which membrane remodeling proteins catalyze membrane fusion and fission is not yet fully understood. The membrane remodeling proteins may take any combination of the following actions to facilitate fusion and fission:

1. Directly altering the local curvature of the membrane
2. Altering the line tension at L_o/L_d phase boundaries
3. Forming protein clusters to act collectively on the membrane
4. Altering the local composition of the membrane at the site of fusion or fission
5. Physically disrupting the lipid assemblies, i.e. by inserting protein domains into the membrane and creating membrane defects

In this work, we examine the extent to which HIV’s membrane fusion protein gp41, and Influenza A’s membrane fission protein M2, utilize these five processes to carry out their functions. We use solid-state NMR techniques to probe intermolecular interactions along those lines, with an emphasis on curvature and clustering. The contributions of both proteins and lipids to these processes will be examined. The goal is to better understand the mechanisms of HIV entry and influenza release, which can hopefully guide the development of better therapeutics and vaccines.

Thesis Supervisor: Mei Hong
Title: Professor of Chemistry

List of Figures

List of Tables

I. Introduction

I.1. Motivation: HIV, Influenza, and unmet medical needs

At its height as an epidemic, HIV killed millions of people. For those who can access it, anti-retroviral therapy (ART) has transformed HIV into a manageable chronic condition. However, ART's severe adverse effects challenge treatment follow-through [1]. The WHO has catalogued gravely concerning global upward trends in HIV drug resistance; by 2019, *pretreatment* drug resistance rates surpassed 10% in 12 of the 18 reporting countries [2]. Along with inequities of access to existing treatment [3], these factors continue to motivate global investment in the search for effective vaccines and improved therapeutics [4].

Influenza is associated with an average of 35,000 deaths in the US alone each year, with vast variations between cycles, based on CDC data [5]; these figures include deaths from bacterial co-infections. A 2021 review article detailed how influenza has evaded any form of sterilizing immunity, and multiple lines of evidence suggest that previous infection and vaccination lead to immunoattenuation rather than reduced infection risk [6]. To protect vulnerable patients, rational improvements to vaccine design strategies are needed, i.e. cross-reactive vaccines or vaccines designed based on immune factors correlated with immunoattenuation. Unlike most respiratory infections, influenza has effective prophylactic and therapeutic drugs, though their effectiveness decreases if treatment commences too long after the onset of symptoms. As was recently reviewed [7], SARS-CoV-2's comparable viral dynamics to influenza suggest that lessons learned in the design and rollout of influenza therapeutics can be constructively applied to coronavirus therapeutics.

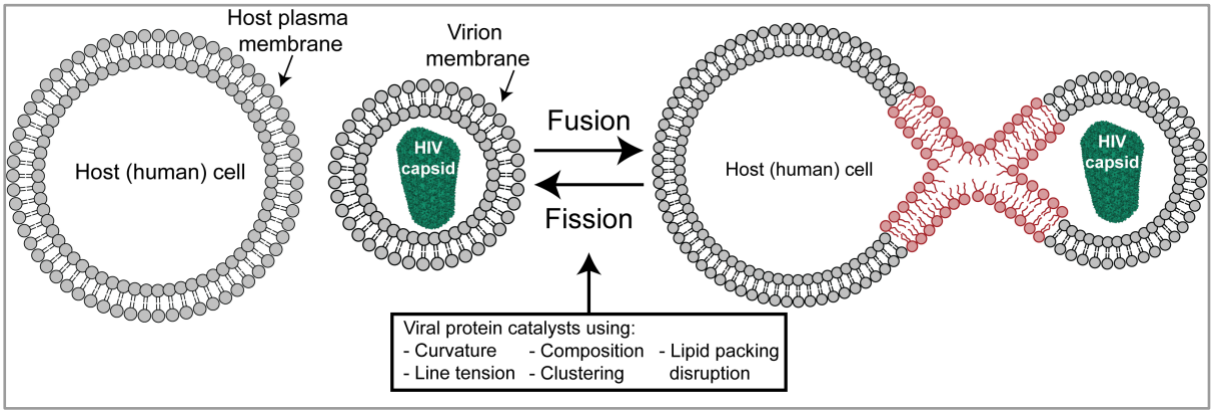

Figure I.1. Viral membrane fusion and fission.
In this example, an HIV virion (capsid: PDB 3J3Q [8]) must fuse its membrane with the host's membrane to gain entry into the host cell (*fusion*). In the reverse process, a newly made virus particle will pinch off a piece of the host cell membrane to make its virion membrane, then divide the membranes (*fission*) so that a free virus particle is released. Viral membrane remodeling proteins will facilitate this process using some combination of the effects named above.

I.2 Membrane remodeling biophysics

Membrane fusion and fission (**Figure I.1**) are essential steps in the life cycle of enveloped viruses. In this section, we outline relevant background information on the different modes of membrane remodeling named above (**Abstract**). While not exhaustive, this section should be sufficient to orient the reader to the different membrane effects that may play a role in the viral membrane fusion and fission events we are studying. These general principles can guide the interpretation of our experimental data in **Chapters 2-4**.

I.2.a. Membrane curvature

The most basic requirement of membrane fusion and fission is local deformation of the affected membranes through highly-curved intermediate states (**Figure 1.2**). Thus, membrane remodeling proteins' functions likely include direct or indirect modulation of local membrane curvature.

The curvature of lipid membranes can be described numerically as outlined by Chernomordik and Kozlov [9]. A given point on a monolayer or leaflet has two principal curvatures, c_1 and c_2, whose magnitude corresponds to the inverse radius of curvature, and whose sign is defined for lipid bilayers by convention (see **Figure I.2 a, b**):

- *Positive* principal curvature = curvature toward the polar lipid heads, such that heads are pushed apart from each other
- *Negative* principal curvature = curvature toward lipid tails, pushing lipid heads closer together.

The curvature of a monolayer can be conceptualized as the curvature of the surface connecting all the polar heads, and described mathematically as follows:

- The *total curvature* of a monolayer is the sum $J = c_1 + c_2$
- The *Gaussian curvature* of a monolayer is the product $K = c_1 \cdot c_2$

Therefore, *positive Gaussian* curvature appears in a leaflet that is budding in or out, such that the principal curvatures at a given point on the surface are of matching sign (**Figure 1.2 c**). On the other hand, *negative Gaussian* curvature can be described as "saddle-splay," with any point on the surface possessing principal curvatures c_1 and c_2 of opposite sign (**Figure 1.2 d**). The geometry of joining or parting two membranes in a fusion or fission event creates a requirement for negative Gaussian curvature, as shown for the contacting monolayers in the hemifusion "stalk" intermediate (**Figure 1.2 e**).

Certain lipid species can impart monolayers with spontaneous curvature, denoted J_s. Lipids with relatively small head groups relative to their tails, such as phosphoethanolamines, geometrically favor negative monolayer curvature [10]. Positive spontaneous curvature can arise from species with the opposite geometric profile such as lysophosphocholines [11], or from charge repulsion as was demonstrated for POPS [12]. Curiously, as will be discussed further in **Chapters II** and **IV**, our lab has repeatedly found that membranes composed in full or in part of POPE (16:0/18:1(9Z) PE) can be more easily deformed into geometries with *negative Gaussian* curvature by membrane remodeling peptides**.**

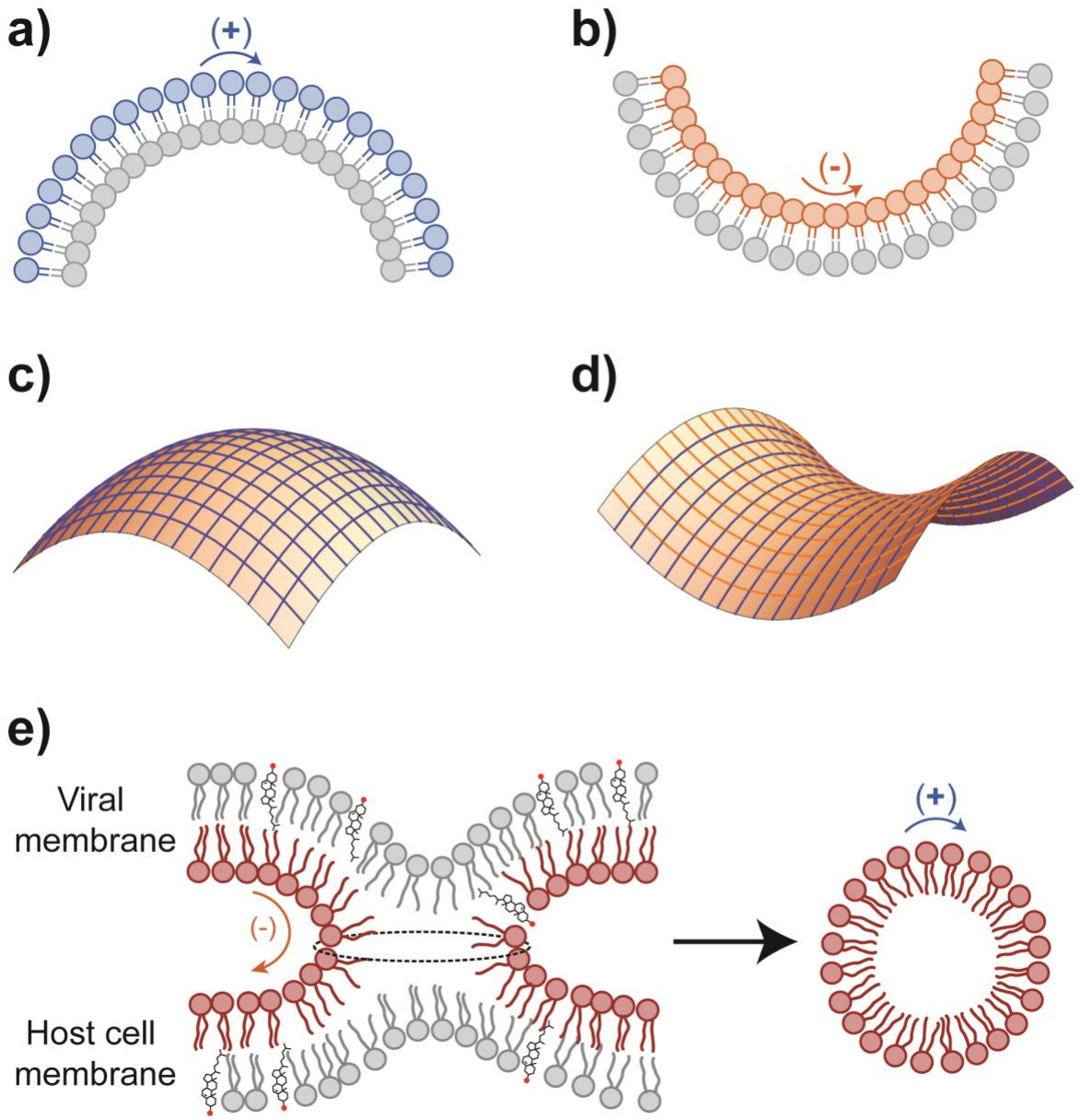

Figure I.2. Definitions and conventions for membrane curvature; relation to membrane fusion and fission.

(a) The blue monolayer of this bilayer cross section shows a (+) signed principal curvature, pushing the lipids' polar heads away from each other. (b) The orange monolayer of this bilayer cross section shows a (-) signed principal curvature, with polar heads squeezed together. In both (a) and (b), the grey monolayer shows an opposite-signed principal curvature from the colored monolayer. (c) A monolayer or leaflet with *positive* Gaussian curvature displays principal curvatures of the same sign anywhere on the surface, (-,-) or (+,+). (d) Conversely, when a monolayer surface displays principal curvatures of opposite signs (+,-), that surface is said to possess *negative* Gaussian curvature. (e) In the hemifusion intermediate states of membrane fusion and fission, the outer/contacting leaflets have fused into one (red) leaflet, which is shown to possess negative Gaussian curvature. The cross sections on the left and right are distinguished by a 90˚ rotation out of the plane of the paper.

Finally, the spontaneous curvature of a *bilayer* (J_s^B) can be thought of us the curvature of the inter-leaflet surface and is proportional to the difference in spontaneous curvatures between the outer and inner leaflets: $J_s^B \propto J_s^{out} - J_s^{in}$ [9]. Authors differ on the sign convention for bilayer curvature, but here for roughly spherical membranes such as those in our proteoliposomes, bilayer curvature will take the sign of the outer leaflet.

I.2.b. Line tension between lipid domains

There is a growing body of direct experimental evidence that the hypothetical membrane lipid assemblies which biochemists refer to as “lipid rafts” [13] may take a real form as **domains** of lipids in the liquid-ordered (L_o) phase [14], coexisting with surrounding liquid-disordered (L_d) domains. The L_o domains are characterized by high cholesterol and sphingomyelin content [14] and intermediate motion parameters: L_o lipids’ lateral mobility and rate of axisymmetric rotations are similar to a normal liquid-crystalline phase, while their acyl chain order is high (meaning chain motions have a small amplitude) similar to a gel phase [15]. Polyunsaturated phospholipids concentrate in liquid-disordered (L_d) domains, where cholesterol content is low (but non-zero [15]) and lipids are relatively loosely-packed and free-moving.

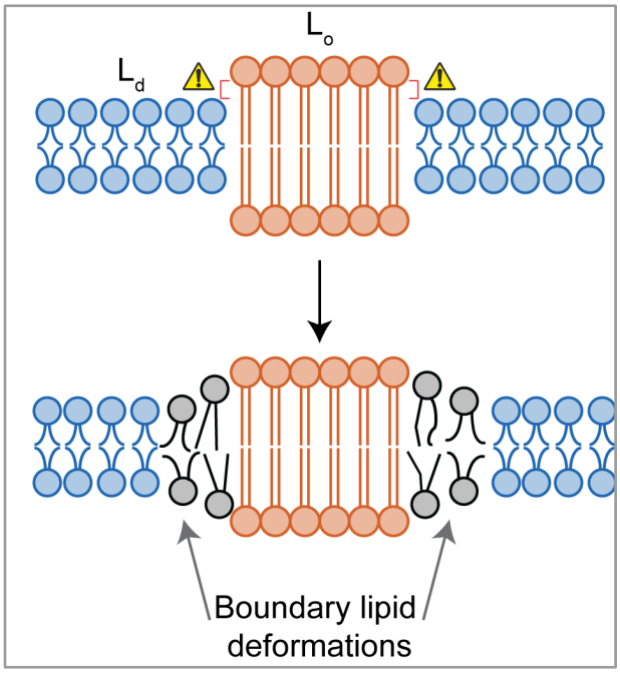

Figure I.3. Line tension and lipid deformations.
A membrane bilayer with lipids demixed into L_o and L_d domains could expose patches of the domain lipids’ hydrocarbon “tails” to the aqueous media (*top*), due to the height differential between domains. However, this is predicted to be so energetically costly that boundary lipids (from both phases) will theoretically exhibit tilt and splay deformations to obscure exposed hydrocarbons [16] (*bottom*).

AFM and X-ray scattering experiments have demonstrated that liquid-ordered (L_o) domains tend to be thicker than the surrounding liquid-disordered (L_d) domains; this leads to a height mismatch between the lipids all along the boundary between the domains [17] (See also **Figure I.3**). Because exposing hydrophobic fatty acid chains to aqueous media would have an immense energy penalty, it is widely predicted that lipids

along the L_o/L_d boundary deform by splay and tilt to remove the exposed hydrophobic surface (**Figure 1.3**) [16], and this distortion has an energy cost at every point along the boundary [17]. The force which scales with this energy is called “line tension.”

In the right experimental setup, line tension can be derived from measurements on lipid layers. Since energy along a domain boundary scales with the total perimeter of the enclosed (i.e. L_o) domains, such domains tend to adopt a circular shape. This arises from the geometric principle that the circle is the shape which encloses the most area per unit of perimeter (hence A/P will be highest for a circle). Therefore, when a domain is deformed by an applied shear force, line tension serves as the driving force for the domain to relax to a circular shape. Line tension (λ) is opposed by a known viscous drag, and equating these forces leads to a model for shape relaxation velocity (V) for a domain [18]:

$$V = \frac{3\lambda}{8\eta R},$$

where η is the viscosity of the aqueous subphase, and *R* is the radius of the domain. Domain radii can vary within a membrane, but line tension pushes small domains to merge into larger domains to minimize the total perimeter [17], while electrostatic repulsions between domains should disfavor merger. The balance between those two competing sets of forces is thought to regulate the size of L_o domains.

Drawing upon this model, Trabelsi and colleagues formed Langmuir monolayers of mixed fluorocarbon- and hydrocarbon-rich fatty acids, and showed that the hydrocarbon domains appeared as bright circles in Brewster angle micrographs [19]. They then used syringe needles to deform the circular domains into bolus shapes, measured their relaxation velocity, and backed out monolayer λ values from plots of domain relaxation velocity vs domain radius. In this same set of acyl monolayer experiments [19], an important and novel class of molecules were defined. *Linactants* were defined as molecules that:

1) Localize to the edges between domains, and
2) Reduce the line tension along those edges.

Thus, they are the 2D analogs of surfactants. Trabelsi and colleagues designed simple linactants: amphiphiles with mixed fluorocarbon/hydrocarbon chains, and showed that they reduced the measured line tension in their monolayers.

Linactants are of direct relevance to the systems in our studies. In one set of experiments with vesicles and supported lipid bilayers, adding linactant molecules to the DPPC/DOPC/DOPS/cholesterol (2:1:1:1) membranes both reduced L_o domain sizes (validating the additives as linactants), and reduced the efficiency of HIV fusion peptide (FP)-induced membrane fusion [20]. Influenza M2 was declared a “linactant” after fluorescence microscopy, *in situ* immunogold staining, and course-grain MD simulations showed that it met part (1) of the definition above – localizing to the L_o/L_d domain boundaries [21]. However, both HIV gp41 and Influenza M2’s direct effects on line tension (positive or negative) remains to be determined.

Table I.1: Experimental relations between line tension and other membrane properties
These properties were measured in DxPC:SM:cholesterol bilayers in [17].

Property	**Relation to line tension (λ)**
Demixing temperature (˚C)	Increases linearly
Log area distribution	Shifts to the right with higher λ
Domain area growth rate	Increases linearly
Domain circularity	Increases (~logarithmically)
Membrane curvature at L_o/L_d boundary	Increases

Relationships between line tension (λ) and other measurable observable parameters were demonstrated by Ana Garcia-Saéz and colleagues [17]. The authors constructed membranes of 2:2:1 DxPC : sphingolipid : cholesterol composition, where DxPC were di-unsaturated phosphocholine glycerophospholipids with varying acyl chain lengths. 3D AFM images of the membranes' topography indeed showed L_o domains were thicker, and the height differential between the L_o and L_d domains (δ) was larger for membranes with shorter-chain di-unsaturated lipid components. These measured height differentials were plugged into Kuzmin and colleagues' theoretical model [16] to back out line tension. The membranes were heated above their phase transition points and then slowly cooled to 21˚ over five minutes, and confocal micrographs taken at intervals showed the temperatures at which the membranes demixed into L_o and L_d domains. These "demixing temperatures" were positively linearly related to line tension. Additional measured membrane properties' demonstrated relationships with line tension are summarized in **Table I.1**. Most importantly, in this same study [17], fluorescence confocal images of hundreds of giant unilamellar vesicles (GUVs) showed that *vesicles with higher L_o/L_d height differentials (δ)* (and therefore higher line tension λ) *had more local membrane curvature at the boundary***.** In the moderate-λ regime, L_o domains were shown to form bell shapes with visible rings of negative Gaussian curvature, and one GUV even appeared to bud off to the inside and form an enclosed vesicle. Budding-out behavior was observed at high λ.

The take-home message: line tension is a measurable force that pushes enclosed L_o domains in lipid bilayers adopt large circular shapes, so as to minimize their total perimeter. Line tension can be altered by simply varying the composition of the membrane, which cells actively do, and many other membrane properties vary with line tension. Thus, line tension is likely to be a key parameter in regulating the architecture of raft-like L_o domains in cell and viral membranes. Since line tension and local curvature impact each other, *membrane remodeling proteins may alter line tension to induce curvature, or vice versa*.

Thus, a membrane remodeling protein can in theory cause fusogenic/scission-promoting curvature by one or both of these routes: either directly exerting a force upon the membrane, or by altering the line tension at the boundary between the L_o and L_d domains.

I.2.c. Protein clustering

For membrane proteins, transient assembly into functional clusters (homotypic or heterotypic) is commonly observed. For example, fluorescence microscopy data revealed Gag-restricted clustering of the HIV Env protein upon virus maturation [22]. Oxidation-sensitive co-clustering of the SNARE component syntaxin-1A and the pore-forming subunit of Ca^{2+} channel Cav1.2 was associated with the functional interactions between these proteins in exocytotic neurotransmitter release [23]. Intracellular membrane fusion between different organelles is accomplished by multiple SNARE proteins, which are clustered at the fusion site with the help of specific lipids [24-26]. For clathrin-coated vesicles (CCVs, prominent in intracellular membrane fusion/fission events), clusters of adapter proteins appear to have a key role in generating curved membranes and positioning the faces of the cage [27].

Some mechanistic models for membrane fusion and fission seem to have a strong potential for cooperative action of multiple membrane remodeling proteins. For example, biophysical evidence and modeling suggest that two-plus trimers of parainfluenzavirus-5 (PIV-5) F fusion proteins assemble to carry out fusion [28, 29]. By forming clusters, fusion and fission proteins could in principle exert stronger surface deformation and membrane disruption impacts. The presence or absence, energies, and functions of clusters of membrane remodeling proteins are still largely unknown. In **Chapters III** and **IV** we explore the possibility that HIV gp41 and influenza M2 form functional clusters to carry out their functions.

I.2.d. Lipid composition effects

As mentioned in **Section I.2.a**, certain lipid components of a membrane can favor positive or negative curvature. Further, it's well known that the amount of cholesterol has profound effects on the rigidity, phase transition temperatures and other physical properties of lipid membranes. During fusion and fission, especially at the hemifusion stalk stage (**Figure I.2 e**), the curvature requirements of the outer and inner leaflets of the fusion/dividing bilayers are different. Therefore, it is possible that viral membrane remodeling proteins can influence the *local* composition of one or both leaflets at the site of fusion.

Some observations relating to Influenza and HIV suggest the possibility that the viruses actively recruit certain lipid species. Asymmetry in the lipid composition between leaflets was discovered and catalogued first for human red blood cells (erythrocytes) [30]. Many other indirect lines of evidence supported leaflet asymmetry in other mammalian cell types as well as enveloped viruses [31]. The discovery of phospholipid translocases, and their ubiquity in mammalian cells, led to a consensus that composition asymmetry between leaflets is the default state for mammalian cells [32]. Observation of PE and PS species on the HIV virion outer leaflet belies at least partial loss of leaflet composition asymmetry in virions [33, 34]. Further, as will be discussed more below, virion membranes of both HIV (**Chapter II**) and influenza (**IV**) have dramatically different lipid compositions than the plasma membranes of the cells from which they're derived.

I.2.e. Disruption of lipid assembly

Membrane remodeling proteins can disrupt the packing of lipids in their surrounding membrane patches in several different ways. In addition to the subtler effects of membrane peptide insertion on the motion and order of the surrounding lipids, there are some dramatic effects of peptide insertion on lipid assembly.

Some fusogenic proteins and peptides insert into the contacting leaflets at a 45-90˚ angle with the bilayer normal, displacing and perturbing surrounding lipids. For various peptide constructs of the gp41 Fusion Peptide domain, which inserts into host membranes to initiate fusion, fusogenic activity was positively correlated with insertion depth [35]. We will explore the membrane composition dependence of insertion depth for the HIV gp41 membrane-proximal external region (**Chapter III**) and the M2 amphipathic helix domain (**Chapter IV**).

Additionally, in one mechanistic model for the PIV-5 F protein's function, the transmembrane fusion peptide (FP) and C-terminal TMD peptides form a "pinprick" in the membrane, lined with protein surfaces and lipid polar heads and filled with water, which then expands into a fusion pore [28]. As will be discussed further in **Chapter II**, our ^{1}H-^{31}P HETCOR NMR data along with Piai and colleagues' HDX data [36] support a model wherein the C-terminal portion of gp41's transmembrane domain creates water defects in the inner leaflet of the HIV membrane. Such defects have the potential to aid the merger of virion and cell inner leaflets, a step for which the driving force is particularly poorly understood.

I.3. Background: NMR tools for studying membrane protein assemblies

The NMR methodologies used in these studies took advantage of two major experimental phenomena: the high sensitivity of ^{19}F NMR, and the utility of spin diffusion to probe interactions over long distances. Building upon recent technological advances with these techniques, it was possible to observe interactions between nuclei on adjacent clustering peptides, document hydration and de-hydration of membranes undergoing remodeling, and probe the interactions between peptide sites and distant CH_3 ends on phospholipids. In this section, we review the physical principles that enable these observations.

I.3.a. Spin diffusion in NMR

Magic-angle spinning (MAS) solid state NMR offers many powerful methods for detecting magnetization transfer between nuclei over long distances. The methods for detecting such contacts employed in this work are all based on spin diffusion: relayed transfer of z magnetization between neighboring spins. As previously reviewed [37], this z magnetization can diffuse over several nanometers due to its long relaxation times, making spin diffusion ideal for detecting intermolecular interactions over long distances. We have previously taken advantage of this property to catalog the overall architecture of many biomedically relevant protein-membrane assemblies. Spin diffusion

pulse sequences generally involve exciting “source” spins, then allowing for a variable mixing time τ_m in which magnetization transfers from the source spin to the sink spin, followed by detection (see [38-40]).

In experiments where the source spins are well localized and the signal intensity is strong, source-sink distances can be extracted from spin diffusion buildup curves. In some systems, especially where spin diffusion is being measured between domains with slow interfacial transfer, as is the case for protein-lipid interactions [39], spin diffusion can be appropriately modeled on a 1D lattice of spins with magnetizations M_i. At t=0, all magnetization resides on the source spin, i.e. $M_1 = M_{tot}; M_{i\neq 1} = 0$, to model the effect of selective excitation (i.e. excitation followed by a T_2 filter to select for magnetization in the mobile domain). As given in Schmidt-Rohr and Spiess’ book [41], at each time step, each spin exchanges a portion of its magnetization with its neighbors according to:

$$\frac{\Delta M_i}{\Delta \mathrm{t}} = -\left(\Omega_i^l + \Omega_i^r\right)M_i + \Omega_{i+1}^l M_{i+1} + \Omega_{i-1}^r M_{i-1}$$

The transition rates between spin pairs, Ω (ms^{-1}), are related to the distances a (in nm) between neighboring spins in the array and the approximate diffusivity of the substance, D (in nm^2/ms) by $D = \Omega a^2$. The transition rates Ω also correspond to half the line width of the corresponding ^2H wideline spectrum, scaled by $\frac{1}{\sqrt{6}}$ for transfer in a single direction. Finally, in the above model we allow above for different transfer rates between different pairs of spins to allow for spins in different domains or substances being simulated to have different diffusivities, as these depend heavily on factors such as molecular mobility; transfer across interfacial (i.e. water/protein, water/membrane) gaps tends to be very slow [38]. Conservation of total magnetization is assured by $\Omega_i^r = \Omega_{i+1}^l$ and vice versa.

Because of this collective behavior, the magnetization at the sink spin builds up as a function of the mixing time τ_m. Therefore, plots of measured intensity of the sink species vs $\sqrt{\tau_m}$ show an initial lag phase, followed by build-up to a maximum representing when magnetization is equilibrated between the domains. This will be demonstrated later in the case of water-to-phospholipid magnetization transfer in proteoliposome samples (**Chapter II**). The lag is not apparent in plots of Intensity vs τ_m. In terms of data interpretation, the most important result from all this theory is that *faster intensity build-up corresponds to source and sink spins which are closer together*.

Distances between nuclei estimated in these experiments are accurate to a couple Å. Many such studies have been completed in our lab, in both the PDSD-HETCOR domain and in the CORD-assisted homonuclear SD domain. Thanks to this prior work, *new SD spectra and buildup curves can be associated with distance regimes*, even when exact distance extraction is prohibited by the experimental conditions.

I.3.b. Heteronuclear spin diffusion correlation experiments

In H-X heteronuclear spin diffusion correlation (HETCOR) experiments, the pulse sequence involves excitation of source ^{1}H spins (which can be made selective for mobile species by including a T_2 filter), followed by a variable spin diffusion period, τ_m, in which *z* magnetization transfers from source to sink ^{1}H spins. Subsequent transfer of magnetization to nearby X (^{13}C, ^{31}P, or ^{19}F) spins via cross polarization pulses (see [37-39]) allows for detection on those X nuclei. We have deployed this methodology in these studies to assess membrane hydration via spin diffusion from water ^{1}H's to membrane lipid phosphate head groups, and to probe the insertion of protein domains into membranes via spin diffusion from lipid CH_3 ^{1}H's to ^{19}F or ^{13}C sites on proteins.

1.3.b.1. Versatility of multinuclear spin diffusion experiments

Membrane remodeling proteins in viruses and cells do not operate in a vacuum, but coordinate with each other, membrane lipids and even surface water to bring about membrane fusion and fission. To detect such diverse interactions, heteronuclear spin diffusion correlation (HETCOR) experiments take advantage of both rapid spin diffusion between ^{1}H spins over long distances, and the specificity of isotopic labeling on species receiving intermolecular transfer.

The HETCOR method of measuring intermolecular interactions and distances was previously developed in our group to approximate the insertion depth of colicin Ia in membranes, as well as the architecture of DNA/membrane-lipid complexes [39]; in these early studies, sink magnetization buildup curves matched with spin diffusion simulations allowed for quantification of inter-molecular distances. Distances extracted from spin diffusion buildup curves using membrane lipids and water as sources and the protegrin-1 peptide as a sink showed that the peptide was well-inserted into bacteria-inner-leaflet-mimetic POPE/POPG membranes, but it was surface-bound in eukaryotic-like POPC/cholesterol membranes [42], thus helping explain the antimicrobial peptide's differential toxicity between bacteria and eukaryotic cells. Finally, in the case of delocalized spin diffusion between bound waters and a protein, the spin diffusion buildup rate is proportional to the water-exposed protein surface area. This principle enabled a study showing that the low-pH "open" state of the Influenza M2 channel has a larger water-exposed surface area [43] than the "closed" state.

I.3.c. Advantages of ^{19}F NMR for mid-range distance detection

Many modern problems in biophysics require us to determine the architecture of complex biological assemblies, from virus capsids to biofilms to cell walls and extracellular matrices to the membrane protein-membrane assemblies documented here. Such problems require detecting intermolecular interactions on the nanometer length scale. The ^{13}C and ^{15}N NMR methods that utilize internal labeling sites on proteins face inherent signal limitations due to the low gyromagnetic ratios (and therefore weak dipolar couplings) of ^{13}C and ^{15}N nuclei – in particular, interatomic distance measurements are limited to contacts over about 5-8 Å. As was recently reviewed by Grage and coworkers [44], ^{19}F NMR fills a critical gap between the aforementioned convenient but low-sensitivity ^{13}C and ^{15}N NMR methods on the one

hand, and on the other hand, fluorescence spectroscopy methods which can probe multi-nanometer distances but require sample labeling schemes that perturb the system much more than ^{19}F labels.

The advantages of ^{19}F NMR are myriad. There are no known ^{19}F species in naturally occurring biomolecules, so there's no background signal coming from the system. Incorporating ^{19}F into biomolecules leads to relatively gentle computed [45], structural [46] and functional [47] perturbation. Additionally, ^{19}F's large isotropic chemical shift range offers many labeling possibilities. Further, ^{19}F chemical shifts exhibit profound sensitivity to the local environment [44], such that for example, a recent ^{19}F NMR study of 4F-Phe-6,22 labeled glucagon was able to demonstrate greater solvent exposure at Phe6 than Phe22 [48]. Both the large chemical shift range and acute environmental sensitivity of ^{19}F have been attributed to the concentration of electrons in lone pairs (or, perhaps more precisely, lone pair-like FMOs), and chemical shift effects are dominated by changes in local electrostatic fields and van der Walls interactions [49]. Most importantly for this study, ^{19}F has the second highest gyromagnetic ratio of all abundant and stable nuclei, only 6% lower than that of ^{1}H spins. The natural result of that is higher internuclear dipolar couplings, since dipolar couplings between two spins *I* and *S* scale as $\omega_d \propto \frac{\gamma_I \gamma_S}{r_{IS}^3}$. This extends the range of detectable internuclear distances r_{IS} out to around 2 nm under optimal conditions.

I.3.d. Homonuclear ^{19}F-^{19}F spin diffusion for nanometer distance detection

Spin diffusion between ^{19}F nuclei, i.e. at labeled sites on adjacent peptides, can also be a powerful methodology for detecting long-range interactions. As recently reviewed by our group [50], there are two main methodologies employed for ^{19}F-^{19}F spin diffusion studies under MAS, for the two scenarios of (1) spectrally resolved spins vs (2) spins with the same chemical shift. For the first scenario, polarization transfer between spins of distinct isotropic chemical shift can be aided by Combined R_n^ν-Driven Spin Diffusion (CORD) irradiation scheme. The studies presented here fall in this regime, so the methodology will be discussed in greater depth below. For spins with equivalent isotropic chemical shift, anisotropic spin exchange can be probed by the Centerband-only Detection of Exchange (CODEX) and internuclear distances can be extracted by the exchange matrix formalism.

The CORD pulse sequences were originally developed for detection of polarization transfer between ^{13}C-^{13}C spin pairs; in proteins, CORD demonstrated broadband and uniform polarization transfer across the large carbon frequency range [40]. The CORD principle, as applied to ^{19}F-^{19}F spin diffusion, is as follows. The rate of spin diffusion between ^{19}F spins is proportional to the overlap integral between the zero-quantum line shapes of those spins, f_0. Dipolar interactions between ^{19}F and nearby ^{1}H spins are normally averaged out by magic-angle spinning. Applying π pulses synchronized to the rotor spinning period recouples that ^{1}H-^{19}F dipolar interaction, which in turn broadens the ^{19}F lines and increases f_0. Therefore, CORD irradiation can be especially beneficial for ^{19}F spin diffusion, wherein chemical shift differences are generally large.

Distance extraction has to be performed semi-empirically. One can measure 2D ^{19}F-^{19}F CORD spectra at various spin diffusion mixing times t_{mix}, and observe polarization transfer from spin A to spin B as the increase in the AB cross peak intensity (I_{AB}) with increasing t_{mix}. Normalized intensities can be fitted to a function like $I_{AB} = A(1 - \exp(-k_{SD}t_{mix}))$ where A and k_{SD} are the fitted plateau value and buildup constant, respectively.

Our group previously compared ^{19}F spin diffusion buildup curves, extracted from diagonal and cross peak intensities in 2D ^{19}F-^{19}F CORD experiments with varying mixing times, for various compounds with known intramolecular ^{19}F-^{19}F distances [51]. A plot of rate constants (k_{SD}) scaled by the squared difference of chemical shifts between the spins ($\Delta\delta_{iso}^2$) takes the form:

$$k_{SD}\Delta\delta_{iso}^2 = \frac{c}{r^6} = \frac{1}{2}\pi\omega_d^2 f_0$$

Here ω_d is the dipolar coupling constant, and c and f_0 are phenomenological constants. The f_0 term is derived from the overlap integral between the two zero-quantum line shapes. *Here, we assume we're in the regime of two peaks with well-resolved chemical shifts,* and let the Lorentzian term dominate. That term is given by

$$F_L(0) = \frac{g_0\sigma_\Sigma}{\pi(\Delta\delta_{iso}^2 + \sigma_\Sigma^2)} \simeq \frac{f_0}{\Delta\delta_{iso}^2}$$

With the latter asymptotic equivalence given by the assumption that the isotropic chemical shift difference ($\Delta\delta_{iso}$) dominates over the sum of half-linewidths (σ_Σ), such that

$$f_0 == \frac{g_0\sigma_\Sigma}{\pi}$$

Finally, g_0 comprises the phenomenological part of f_0: g_0 corrects for the impacts of magic angle spinning and CORD irradiation on the spin diffusion rate constant k_{SD}, and cannot be predicted.

The theory described above leads naturally to the applicability criteria for the ^{19}F-^{19}F CORD methodology. Our observed correspondence between $\Delta\delta_{iso}$-adjusted spin diffusion buildup rate constant and internuclear distance applies only in the weak-coupling limit, meaning the regime where the isotropic chemical shift difference ($\Delta\delta_{iso}$) substantially exceeds the ^{19}F-^{19}F dipolar couplings. This condition can be expected to hold for most structure-determination applications of ^{19}F NMR because using different fluorine labeling schemes at different sites yields large $\Delta\delta_{iso}$.

Importantly, it was found [51] that CORD irradiation increased the polarization transfer rate (for exchange between spins with distinct isotropic chemical shifts) >10-fold compared to PDSD, and a 16 Å contact between 3F-labeled Y3 and Y33 sites on the GB1 peptide appeared to constitute the outer distance detection limit. Master curves were constructed, relating the measured spin exchange rates k_{SD}, scaled by the squared isotropic chemical shift difference $\Delta\delta_{iso}^2$, to interatomic distances via

$$\log(k_{SD}\Delta\delta^2) = \log c - 6\log r$$

A 100-fold higher *c* value was fit for CF—CF_3 transfer compared to CF—CF, indicating that simultaneous transfer to three fluorines and rotational averaging of the ^{19}F CSA substantially speeds up spin diffusion. There were two cases where the plateau intensity values corresponding to the source and sink spins should have been primarily influenced by the interaction between those two spins, rather than other ^{19}F nearby spins influencing the source polarization decay rate:

1. F_P → CF_3 transfer in formyl-MLF, with sink/source plateau intensity ratio of ~2.5 and internuclear distance 8.9 Å
2. Y3/Y45 → Y33, with intensity ratios of ~10-11 and internuclear distances of 15.6 and 16.0 Å.

In the present work, we used this same methodology to successfully detect inter-molecular contacts between Phe47 sites on M2CD, alternately labeled with 4-^{19}F or 4-$C(^{19}F)_3$. If the t_{mix} value of 500 ms indeed represents the plateau, the sink/source intensity ratios of 0.32 in the clustering-friendly membranes may indicate an inter-site distance closer to the 9 Å regime (**Chapter IV**).

As our group recently reviewed [52], 2D ^{19}F isotropic spin exchange NMR has recently been applied to other biomolecular interactions. We used a 500-ms CORD spectrum to detect contacts between the ^{19}F-7-labeled cholesterol tails in lipid bilayers and two ^{19}F labeling sites of HIV gp41's Membrane-Proximal External Region [53], demonstrating direct cholesterol-gp41 interactions. Further, 2D 40 ms ^{19}F-^{19}F CORD spectra showed cross peaks between two different ^{19}F labeling types of cholesterol's tails, showing direct dimerization of cholesterol in the membrane [54]. Thus, ^{19}F-^{19}F spin diffusion under CORD has previously revealed a number of moderate-distance biomolecular interactions, making it a fitting choice of methodology for our viral membrane protein clustering studies (**Chapters III**, **IV**).

II. Interactions of HIV gp41's membrane-proximal external region and transmembrane domain with phospholipid membranes from ^{31}P NMR

By: Madeleine Sutherland, Byungsu Kwon, and Mei Hong; published in *BBA – Biomembranes* 1863, July 30, 2021

II. Abstract

HIV-1 entry into cells requires coordinated changes of the conformation and dynamics of both the fusion protein, gp41, and the lipids in the cell membrane and virus envelope. Commonly proposed features of membrane deformation during fusion include high membrane curvature, lipid disorder, and membrane surface dehydration. The virus envelope and target cell membrane contain a diverse set of phospholipids and cholesterol. To dissect how different lipids interact with gp41 to contribute to membrane fusion, here we use ^{31}P solid-state NMR spectroscopy to investigate the curvature, dynamics, and hydration of POPE, POPC and POPS membranes, with and without cholesterol, in the presence of a peptide comprising the membrane proximal external region (MPER) and transmembrane domain (TMD) of gp41. Static ^{31}P NMR spectra indicate that the MPER-TMD induces strong negative Gaussian curvature (NGC) to the POPE membrane but little curvature to POPC and POPC : POPS membranes. The NGC manifests as an isotropic peak in the static NMR spectra, whose intensity increases with the peptide concentration. Cholesterol inhibits the NGC formation and stabilizes the lamellar phase. Relative intensities of magic-angle spinning ^{31}P cross-polarization and direct-polarization spectra indicate that all three phospholipids become more mobile upon peptide binding. Finally, 2D ^{1}H-^{31}P correlation spectra show that the MPER-TMD enhances water ^{1}H polarization transfer to the lipids, indicating that the membrane surfaces become more hydrated. These results suggest that POPE is an essential component of the high-curvature fusion site, and lipid dynamic disorder is a general feature of membrane restructuring during fusion.

II.1. Introduction

HIV entry into target cells (i.e. CD4+ T-lymphocytes and macrophages) is mediated by the trimeric Env glycoprotein complex [55]. The gp120 component of the complex binds host cell CD4, CCR5 and CXCR4 receptors, and dissociates from gp41. Gp41 then proceeds to fuse the virus lipid envelope with the host cell membrane via a cascade of conformational changes [56, 57]. This membrane fusion involves an initial merger of the outer leaflets of the virus and cell membranes, followed by fusion of the inner leaflets, and subsequently the emergence and enlargement of a water-filled pore that permits the virus particle to enter the cell [58]. This virus-cell fusion involves intermediate, energetically unfavorable structural changes of two lipid membranes and the intervening water layer, and it is only possible due to the energetically favorable conformational changes of the fusion protein from a metastable prefusion state to an equilibrium post-fusion state [9, 59].

The protein-lipid structural changes involved in membrane fusion have been extensively studied, but many questions remain due to the conformational plasticity of these fusion complexes. On the protein side, gp41 transits through at least three conformational states: a prefusion state, an extended intermediate state where an N-terminal fusion peptide (FP) is inserted into the target cell membrane, and a post-fusion state. In the post-fusion state, the N- and C-terminal halves of the water-soluble portion of the protein are bent into a trimer of hairpins, pulling the target cell membrane and the virus envelope into close proximity [60]. Crystal structures of the prefusion and post-fusion states are known for gp41 and a number of other class I viral fusion proteins [61-64], while the intermediate states remain difficult to capture [65, 66]. Although post-fusion structures of the ectodomain are available for many viral fusion proteins, their biological relevance is still unclear, as these structures are usually obtained in the absence of the transmembrane domain (TMD) [62]. Recent NMR studies of the C-terminal region of gp41 that includes a membrane-proximal external region (MPER) and the TMD provided some of the missing information. In lipid bilayers that mimic the virus envelope, the MPER-TMD peptide forms trimers, with the MPER helix lying on the membrane surface while the TMD helix spanning the membrane [67] (**Fig. II.1**). In DMPC : DHPC bicelles, the MPER-TMD also shows a trimeric assembly based on intermolecular paramagnetic relaxation enhancement NMR data [68], but the MPER conformation differs from that obtained in lipid bilayers. When only the TMD is incorporated into bicelles, both monomeric and trimeric structures have been reported using solution NMR [69, 70], suggesting that the TMD structure might be sensitive to environmental effects such as peptide concentration, temperature, and bicelle size. In lipid bilayers, when the gp41 fusion peptide is covalently linked to the MPER-TMD in a chimera, no cross peaks were detected between the FP and TMD residues, indicating that the FP and TMD do not come into close molecular contact to form a helical bundle [71]. Therefore, these two hydrophobic ends of the protein, as engineered in the chimera, do not appear to form a tight six-helix bundle like the ectodomain. Similarly, a FP-TMD chimera of the parainfluenza virus 5 fusion protein F also does not exhibit correlation peaks between the FP residues and TMD residues [72]. These results open the question of how these N- and C-terminal hydrophobic domains restructure the lipid membrane to generate fusion intermediates and the fusion pore.

In addition to protein conformational changes, individual lipids need to interact with the proteins to incur membrane curvature and membrane dehydration during virus-cell fusion. Molecular details of this these protein-lipid interactions are still poorly understood. The main curvature effect that is believed to occur during membrane fusion is the negative Gaussian curvature (NGC) (Fig. II.1), where every point on a surface has opposite-signed principal curvatures [73, 74]. NGC is known to be important in many membrane-remodeling events such as fusion, scission, and pore formation [74-77], and can be characterized using small-angle X-ray scattering and solid-state ^{31}P NMR. Lipids with intrinsic curvature tendencies in membranes such as phosphatidylethanolamine (PE) and lysophosphocholine (LPC) promote and inhibit protein-free membrane fusion, respectively [9], but how these lipids interact with proteins to mediate membrane fusion has not been studied. Biochemical data show that negatively charged phosphatidylserine (PS) and cholesterol are both cofactors in Env-mediated HIV-cell fusion. The virion envelope and the target cell membranes both contain a high level of PS [33], and this PS enrichment is promoted by Env-receptor interaction [78].

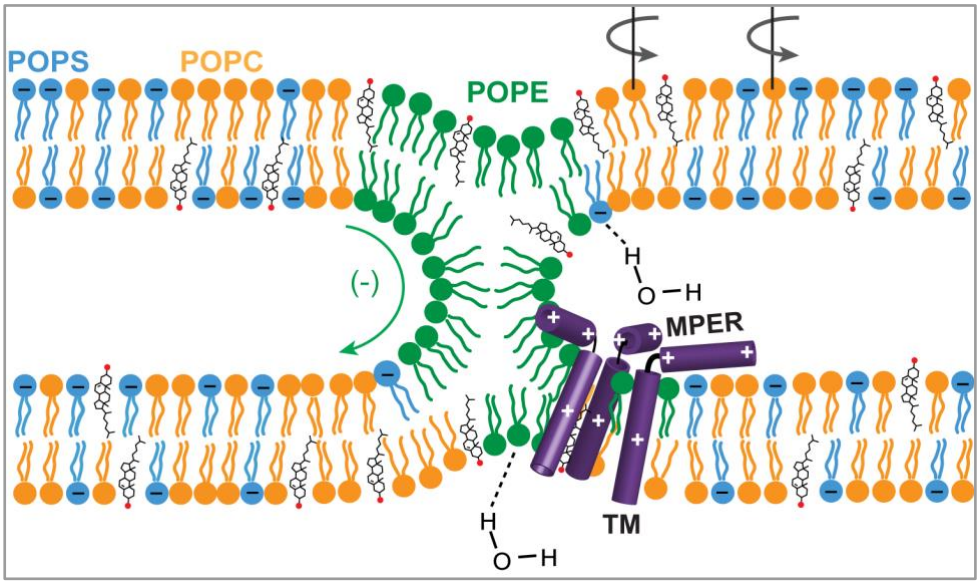

Figure II.1. Schematic model of the possible effects of gp41 MPER-TMD trimers on membrane structure and dynamics, to be investigated by the experiments shown in this work.
The peptide might coordinate with negative-curvature lipids such as POPE (green) to induce negative Gaussian curvature. The peptide might change lipid mobility and membrane surface hydration to charged lipids such as POPS (blue) and zwitterionic lipids such as POPC (orange). At neutral pH, MPER-TMD contains +3 charges. Two MPERTMD trimers are depicted schematically, but the data here do not probe whether multiple trimers are in close proximity.

HIV entry into cells also requires cholesterol in both the host cell and the virion membranes [79]. Removal of cholesterol abrogates gp41-mediated liposome fusion [80], and cholesterol-depleting drugs such as statins inhibit HIV entry into macrophages [81]. Cholesterol affects influenza virus fusion in a more complicated manner [82]. Increasing the cholesterol content in target cell membranes accelerates lipid and content mixing. In contrast, moderate reduction of the cholesterol level from the virus

envelope facilitates fusion while complete depletion of cholesterol slows fusion. This multiphasic effect was interpreted as resulting from the lateral organization of the membrane and cholesterol's effect on the mechanical properties of the membrane.

Table II.1. The lipid mole percentages in MT-4 plasma membranes and MT-4 derived HIV virions.
Adapted from quantitative mass spectrometry data of Lorizate and coworkers [83]

Lipids	MT-4 plasma membrane	MT-4 derived HIV
Cholesterol	32.4%	32.7%
Sphingolipids	13.9%	16.0%
PC	15.5%	7.9%
PE	9.7%	5.6%
pl-PE	12.3%	20.9%
PS	11.6%	15.2%
PI	4.4%	1.0%
PG	0.1%	0.7%
Total	100%	100%

To better understand the mechanisms of protein-mediated membrane fusion, many biophysical studies have employed synthetic lipid mixtures that contain 5–6 components to mimic the HIV-1 envelope composition [67, 71, 80, 84]. Derived from the host cell plasma membranes, the HIV envelope contains phosphocholine (PC), phosphoethanolamine (PE), phosphoserine (PS), sphingomyelin (SM), and cholesterol. The percentages of these lipids are somewhat different from those of the host cell plasma membrane (**Table II.1**) [83, 85]. The PC content is ~16% of all lipids in MT-4 plasma membranes but decreases by half (to ~8%) in the virion envelope. In comparison, PS and sphingolipid contents increase from the plasma membrane to the HIV-1 virion, while PE and plasmalogen (pl) PE lipids have counter-directional percentage changes. Cholesterol is enriched in the HIV envelope and is estimated to range from 32% to as much as 45% [83, 85]. For each HIV-1 virion, about 160,000 phospholipids and sphingolipids and about 130,000 cholesterol molecules [85] together solvate 10–19 Env trimers [86].

An implicit assumption in using complex lipid mixtures for studying membrane fusion is that the lipids are homogeneously distributed in the membrane to induce the biologically relevant protein structure and function. However, the average lipid composition of the whole membrane does not necessarily reflect which lipids are abundant at the fusion site. For example, cholesterol is known to be inhomogeneously distributed in biological membranes [87]. If both host cell and HIV membranes have an inhomogeneous distribution of lipids, one can obtain more mechanistic insights by studying gp41 interactions with specific lipids, which may be enriched near the gp41 trimers. Therefore, to understand the protein-lipid interplay that causes membrane fusion, simplified 2- or 3-component model membranes are useful.

Here we present a ^{31}P solid-state NMR study of the structural and dynamical response of POPE, POPC, POPS and cholesterol to the gp41 MPER-TMD peptide. Specifically, we investigate membrane curvature, membrane surface hydration, and lipid dynamics in the presence of MPER-TMD (**Fig. II.1**). MPER-TMD is an independent fusion-competent domain [67], and contains the epitopes for several broadly neutralizing antibodies (bnAbs) of HIV-1. We use static ^{31}P solid-state NMR lineshapes to detect nonlamellar membrane morphologies, direct-polarization (DP) and cross-polarization (CP) ^{31}P spectral intensities to probe lipid dynamics, and 2D ^{1}H-^{31}P correlation spectra to detect membrane hydration. These studies are conducted in one- to three-component lipid mixtures in order to assess the effects of gp41 on individual lipids. For some of the lipid mixtures, we varied the peptide-lipid molar ratio and lipid-cholesterol (CHOL) molar ratio to examine how the formation of nonlamellar phases depends on the lipid concentration. Our data show that POPE is the main lipid that generates NGC in the presence of gp41, that cholesterol inhibits this curvature effect, and that all phospholipids (PE, PS and PC) are more mobile and better hydrated in the presence of the peptide. These results give new and, in some cases, unexpected insights into the interplay between gp41 and lipids to cause membrane restructuring for virus-cell fusion.

II.2. Materials and Methods

II.2.a. Peptide synthesis

The MPER-TMD peptide used in this work corresponds to residues 665−704 of gp41 (KWASLW NWFNITNWLW YIKLFIMIVG GLVGLRIVFA VLSI) from HIV-1 clade B, HXB2 isolate (UniProtKB/Swiss-Prot: P04578.2) [88]. The peptide was synthesized using Fmoc solid-phase chemistry on a custom designed flow peptide synthesizer [89]. It was synthesized on the 0.05 mmol scale using H-Rink amide ChemMatrix resin (0.1 g at 0.5 mmol/g loading size). The resin was swelled in the reaction vessel for 5 min in ~5 mL of N, N-dimethylformamide (DMF) at 70 °C. A 20-fold excess (1 mmol) of unlabeled amino acid was singly coupled with a coupling time of 50 s. After the final coupling step, the peptide was deprotected and cleaved from the resin by addition of TFA : phenol : H2O : TIPS solution (88 : 5 : 5 : 2 by volume) for 3 h. The resin was filtered off, and the crude peptide was precipitated and triturated three times with cold diethyl ether and dissolved in 80% HFIP (1,1,1,3,3,3-hexafluoro-2-propanol) solution. Crude peptide was purified by reverse-phase HPLC using a Vydac C4 column with a linear gradient of 20-–99% channel A over 120 min at a flow rate of 15 mL/min (where channel A is 1:1 v/v acetonitrile:isopropanol and channel B is acetonitrile). MALDI-MS analysis verified the mass to be 4781.5 Da, in good agreement with the calculated mass of 4781.8 Da. The peptide synthesis and purification yield was ~14%. The purity of the peptide was >95% based on HPLC and MS data.

II.2.b. Preparation of proteoliposomes

Three phospholipids were used in this study: 1-palmitoyl-2-oleoyl-sn-glycero-3-phosphoethanolamine (POPE), 1-palmitoyl-2-oleoyl-sn-glycero-3-phosphocholine (POPC), and POPC : 1-palmitoyl-2-oleoyl-sn-glycero-3-phospho-l-serine (POPS) (7:3).

We chose POPX (X = C, E, S) lipids over saturated lipids such as DMPC in order to better mimic the acyl chain compositions of biological membranes. These lipids were mixed with cholesterol (CHOL) and with each other to produce several membrane mixtures: POPE, POPE : CHOL, POPC, POPC : CHOL, POPC : POPS (7:3), and POPC : POPS : CHOL (7:3:2). The CHOL concentrations in these membranes ranged from 0 to 17 mol% of total phospholipids, while the peptide monomer : phospholipid molar ratio (P/L) ranged from 0 to 1:10. A typical sample contained ~1 mg peptide, 5-–16 mg of lipids and cholesterol, and 4-10 mg of water to reach ~40% hydration by mass.

For each membrane sample, the appropriate mass of MPER-TMD was dissolved in ~500 µL TFE. Phospholipids and cholesterol were each dissolved in 200–500 µL chloroform. A drop of methanol was added when needed to fully dissolve POPE. The resulting homogeneous lipid solution was added to the peptide TFE solution. The lipid vial was rinsed with another ~200 µL chloroform, combined with the protein-lipid solution, then transferred to a 20-mL scintillation vial and incubated for 10 min at room temperature. The chloroform and TFE were then removed under nitrogen gas for 15–60 min, and the vial was covered with a Kimwipe and placed in a vacuum chamber for 30–60 min to remove residual solvent.

Proteoliposomes were prepared by resuspending the 5–16 mg peptide-lipid mixture in 2 mL buffer (10 mM pH 7.4 HEPES/NaOH buffer, 1 mM EDTA, and 0.1 mM NaN3), then homogenizing the vesicle solution by one of two methods. For POPC : POPS mixtures, we conducted 10–15 cycles of freeze-thaw between liquid nitrogen and 50 °C. For POPE-containing membranes, which do not homogenize well by the freeze-thawing method, we sonicated the vesicle solution at room temperature using a bath sonicator for at least three rounds of seven minutes each until the solution appeared homogeneous. The proteoliposome solutions were ultracentrifuged in a Beckman Coulter Optima LE-80 K centrifuge using a SW-60 swinging bucket rotor at a speed of 40,000–45,000 rpm (143,000–272,000 × g) at 4 °C for 4–5 h. The wet membrane pellet was slowly dried to a hydration level of 35–50% (w/w) in a desiccator, then spun into a 4 mm MAS rotor through a 5 mL pipette tip in a Thermo Sorvall ST 16R centrifuge.

II.2.c. Solid-state NMR experiments

All static and MAS NMR experiments were conducted on a Bruker 400 MHz (^{1}H Larmor frequency) wide-bore AVANCE III-HD spectrometer using a 4 mm MAS probe tuned to ^{1}H/^{31}P frequencies. For static 1D ^{31}P experiments, the number of scans varied between 1024 and 20,480 to obtain sufficient signal-to-noise ratios for membrane samples of different masses. Unless otherwise noted, ^{31}P NMR experiments were conducted at a set temperature of 298 K for static experiments and 293 K for MAS experiments. Typical radiofrequency (RF) field strengths were 30–50 kHz for 1H and 50 kHz for ^{31}P. The ^{31}P chemical shifts were referenced to the hydroxyapatite signal at 2.73 ppm on the phosphoric acid scale. 1D ^{31}P MAS cross-polarization (CP) and direct-polarization (DP) experiments used a ^{31}P RF field strength of 50 kHz, 3 ms CP at a 1H RF field of 50 kHz, and a ^{1}H decoupling field of 40–50 kHz, for 1024 scans. The ^{1}H chemical shifts were referenced to the lipid chain-end ω signal at 0.9 ppm. All MAS experiments were conducted under 5 kHz MAS. At this spinning frequency, a set

temperature of 290–300 K gives sample temperatures that are at most 5°C higher than the thermocouple reported temperature. The sample temperature is estimated from the water 1H chemical shifts measured on a POPC sample containing a small amount of DSS, and is consistent with the reported minimal heating at this MAS rate [90]. Water ^{1}H T_1 relaxation times were measured using the inversion recovery experiment with variable delays (τ) of 0.01, 0.05, 0.1, 0.25, 0.5, 0.75, 1, 1.75, 2.5, 3.25, and 4.0 s. Most samples contained two populations of water, corresponding to tightly bound versus loosely membrane-associated water [91]. Thus, we fit the inversion recovery intensities using a bi-exponential function $I(\tau) = A\left(1 - 2\,e^{-\frac{\tau}{T_{1a}}}\right) + (1 - A)\left(1 - 2\,e^{-\frac{\tau}{T_{1b}}}\right)$. The population factor A was at least 0.9 in each sample, so we used the larger T_1 value, which represents bulk water, to correct for the ^{1}H spin diffusion buildup intensities.

To measure the water accessibility of phospholipids, we conducted a 2D ^{1}H-^{31}P heteronuclear correlation (HETCOR) experiment with ^{1}H spin diffusion. The pulse sequence starts with four ^{31}P 90° pulses spaced by 2 ms each to saturate the ^{31}P magnetization, then a ^{1}H 90° excitation pulse and a ^{1}H T_2 filter ($2 * 0.745$ ms = 1.49 ms) to select for the water and lipid ^{1}H magnetization. The 2D experiments used 150 t_1 time points to reach a maximum evolution time of 15 ms, and 64–128 scans per t_1 increment. The ^{1}H chemical shift evolution period was followed by a variable mixing time τ_m, during which the water and lipid chain ^{1}H magnetization is transferred to lipid headgroup and glycerol protons, then detected on ^{31}P following CP. The ^{1}H-^{31}P HETCOR spectra were measured with ^{1}H spin diffusion mixing times of 4 to 900 ms to extract the spin diffusion buildup curves. The 2D HETCOR spectra for comparing water-^{31}P cross peak intensities were measured using 25 ms mixing for the POPC : POPS samples and 64 ms for the POPE samples.

All NMR spectra were plotted from TopSpin 3.6.1. For each static ^{31}P spectrum that exhibits a strong isotropic peak, we matched the 90°-edge intensities of the peptide-free control spectrum and the peptide-containing spectrum, then subtracted the control spectrum to obtain a difference spectrum that exhibits only the isotropic peak. The difference spectrum was integrated over the chemical shift range of the isotropic peak while the peptide-containing spectrum was integrated over the entire spectral range. The ratio of these integrated intensities represents the percentage of the isotropic peak in the peptide-containing spectrum.

To obtain spin diffusion buildup curves, we divided the water-POPS cross peak intensities as a function of τ_m by $e^{-\frac{\tau_m}{T_1}}$, using the aforementioned bulk-water 1H T_1 values, to correct for spin-lattice relaxation of water [38]. The T_1-corrected intensities were then normalized to the 900 ms value. Error bars reflect the propagated signal-to-noise ratios of the water-^{31}P cross peaks. The ^{31}P chemical shift anisotropy (CSA) values ($\Delta\sigma$) were read off as the difference between the downfield 0° edge (σ_{11}) of the powder pattern and the upfield 90° edge (σ_{33}).

II.3. Results

We first investigated gp41-induced membrane curvature using static ^{31}P NMR spectra. We compared POPE, POPC and POPC : POPS membranes with and without cholesterol and as a function of P/L ratios. POPE has intrinsic negative curvature, which makes POPE-containing membranes prone to develop NGC in the presence of various membrane-active peptides such as antimicrobial peptides [42, 73, 92] and influenza M2 [74]. POPC is abundant in eukaryotic membranes [93], whereas the negatively charged POPS has been implicated as a cofactor for HIV entry into macrophages [33]. The POPC : POPS (7:3) membrane is therefore useful for investigating the effect of negative membrane surface charge on fusion.

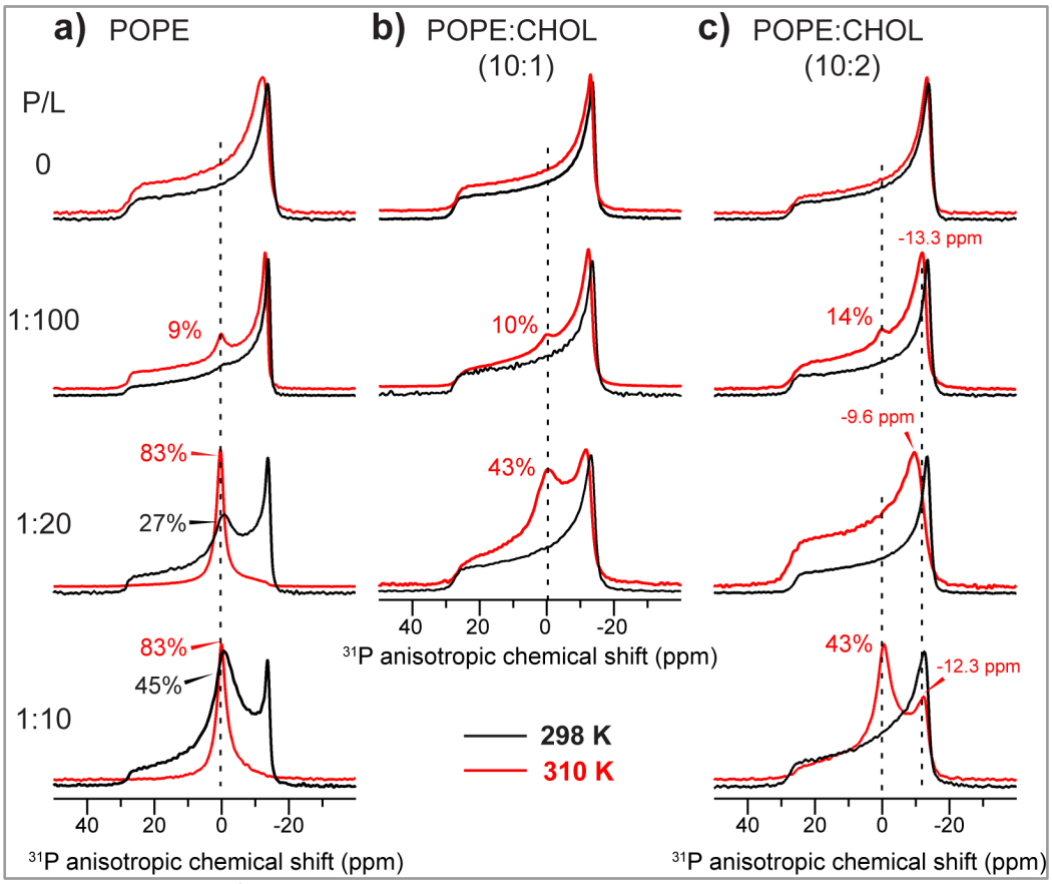

Figure II.2. Static ^{31}P NMR spectra of POPE membranes with varying cholesterol and peptide concentrations.

The P/L ratio increases from top to bottom (0 to 1:10), while the cholesterol concentration increases from the left to the right. Spectra were measured at 298 K (black) and 310 K (red). (**a**) ^{31}P spectra of CHOL-free POPE membranes. (**b**) ^{31}P spectra of POPE : CHOL (10 : 1) membranes. (**c**) ^{31}P spectra of POPE : CHOL (10 : 2) membranes. Dashed lines guide the eye to the POPE isotropic chemical shift. The approximate intensity fraction of the isotropic peak relative to the full spectrum is indicated for various spectra.

II.3.a. MPER-TMD changes the POPE membrane curvature in a cholesterol-dependent manner

Fig. II.2 shows the static ^{31}P NMR spectra of POPE membranes with varying concentrations of cholesterol and peptide. The ^{31}P spectra were measured at 298 K and 310 K to compare the membrane curvature near and well above the main phase transition temperature of POPE (25 °C). The peptide-free POPE membranes with and without cholesterol both show the expected uniaxial powder line shapes that are characteristic of a lamellar bilayer. **Table II.2** shows the ^{31}P CSA and the isotropic intensity fractions. Given the sensitivity of the high-temperature spectra to membrane defects, and the physiological relevance of 310 K for examining virus-cell fusion, we focus our spectral comparison on the 310 K data. At 310 K, the ^{31}P CSA of pure POPE membrane is 43.4 ppm, consistent with a liquid-crystalline membrane. Addition of the peptide at a P/L of 1:100 causes a small isotropic peak. This isotropic peak is reversible: cooling the membrane down to lower temperature suppressed the isotropic peak (data not shown), indicating that the isotropic peak results from a high-curvature membrane phase rather than formation of permanent morphologies such as membrane buds. Further increasing the peptide concentration to P/L = 1:20 dramatically changed the POPE spectra, causing a prominent isotropic peak that represents ~75% of the total spectral intensity. However, at 298 K this isotropic peak percentage decreases to ~15%. We attribute this large change in the isotropic peak intensities to faster lipid lateral diffusion at 310 K over the surface of the membrane, which should better sample the curvature of the POPE membrane.

Increasing the cholesterol concentrations in the POPE membrane reduced the isotropic ^{31}P intensity. In membranes containing 17% cholesterol, the isotropic peak is undetectable at P/L = 1:20. However, as the peptide concentration increased to P/L = 1:10, the isotropic peak increased to 64% even in the presence of 17% cholesterol. Moreover, the combination of peptide and cholesterol narrowed the ^{31}P CSA from 43-44 ppm down to 39–42 ppm by the Herzfeld-Berger convention (see **Table II.2**).

For long-chain phospholipids such as POPE and DOPE, the isotropic peak in the static ^{31}P spectra do not result from isotropic micelles but correspond to bicontinuous lipid cubic phases [77]. This has been shown by ^{31}P T_2 relaxation times and SAXS data [75]. These lipid cubic phases possess NGC on every point of the membrane surface. Due to their cubic symmetry, lipid lateral diffusion over these bicontinuous phases averages the ^{31}P chemical shift to its isotropic value. Since this translational diffusion occurs over tens of nanometers of the cubic phase dimension, the reorientational rate is slower than the local uniaxial diffusion rate of lipids or the tumbling of detergent micelles in solution. Therefore, the isotropic peak of cubic-phase lipids is usually much broader than the isotropic peak of micelles, and the ^{31}P T_2 relaxation times of cubic phase lipids are also much shorter than those of micelles. The isotropic peaks seen in our static ^{31}P spectra are relatively broad, which is consistent with the cubic-phase interpretation. In principle, these isotropic peaks could also reflect membrane buds. But given the non-spontaneous nature of membrane budding, this interpretation is less likely. Further experiments are needed to distinguish these possibilities. The increasing isotropic peak

intensity of the POPE membranes with increasing peptide concentration indicates that the NGC curvature induction is directly caused by gp41 MPER-TMD.

Table II.2. ^{31}P Chemical shift anisotropies and isotropic components of liposome membranes. ^{31}P chemical shift anisotropies ($\Delta\sigma=\delta_{11}-\delta_{33}$ by the Herzfeld-Berger convention) and percentages of the isotropic component in the static ^{31}P NMR spectra of lipid membranes with different peptide:lipid (P:L) mole ratios and at two temperatures.

		298 K		310 K	
Membrane	P:L ratio	Isotropic %	Δσ (ppm)	Isotropic %	Δσ (ppm)
POPE	0	0%	44.2	0%	43.4
	1:100	0%	43.5	9%	44.0
	1:20	27%	42.7	83%	44.4
	1:10	45%	43.3	83%	-
POPE : Chol (10:1)	0	0%	43.7	0%	43.0
	1:100	0%	42.3	10%	41.4
	1:20	0%	42.2	43%	41.2
POPE : Chol (10:2)	0	0%	43.6	0%	40.2
	1:100	0%	42.7	14%	41.6
	1:20	0%	41.2	0%	40.0
	1:10	0%	42.1	43%	39.3
POPC	1:100	0%	46.7	0%	45.2
	1:10	0%	45.1	0%	45.2
POPC : Chol (10:2)	1:100	0%	46.9	0%	45.4
	1:10	0%	45.8	0%	45.2
POPC : POPS (7:3)	1:100	0%	55.2, 44.1	0%	53.9, 42.6
	1:40	0%	51.7, 42.9	0%	52.7, 40.5
POPC : POPS : Chol (7:3:2)	1:100	0%	53.5, 44.0	0%	53.1, 42.6
	1:40	0%	52.1, 42.0	0%	51.9, 40.7

Interestingly, for the POPE : CHOL (10:2) membrane at 310 K, cholesterol's inhibitory effect on peptide-induced membrane curvature is not monotonic with the peptide concentration (**Fig. II.2c**). The isotropic peak is small at P/L = 1:100, undetectable at 1:20, and dominant at P/L = 1:10. This non-monotonic dependence on peptide concentration was reproducible. However, the 1:20 spectrum has a narrower ^{31}P CSA than the 1:100 and 1:10 spectra, manifested by the fact that the maximum of the powder pattern is shifted downfield by 2.4 ppm compared to the 1:100 spectrum. This observation suggests that the POPE lateral diffusion may be faster at 1:20 than at lower or higher P/L ratios, thus obscuring the isotropic peak.

II.3.b. MPER-TMD does not cause curvature to POPC and POPC:POPS membranes

To investigate whether MPER-TMD not only causes curvature to POPE membranes but also to lipid membranes without spontaneous negative curvature, we measured the ^{31}P static spectra of POPC and POPC : POPS (7:3) membranes without and with cholesterol (**Fig. II.3**). **Fig. II.3 a, b** shows that the gp41 peptide caused little nonlamellar morphology to POPC and POPC : CHOL membranes. Even at a high P/L of

1:10, only a small isotropic peak representing less than 7% of the spectral intensity is observed. Similarly, the POPC : POPS membranes showed little isotropic intensity, although at P/L = 1:40 a small isotropic peak is detected (Fig. II.3 c). This peak was removed by the addition of cholesterol (Fig. II.3 d).

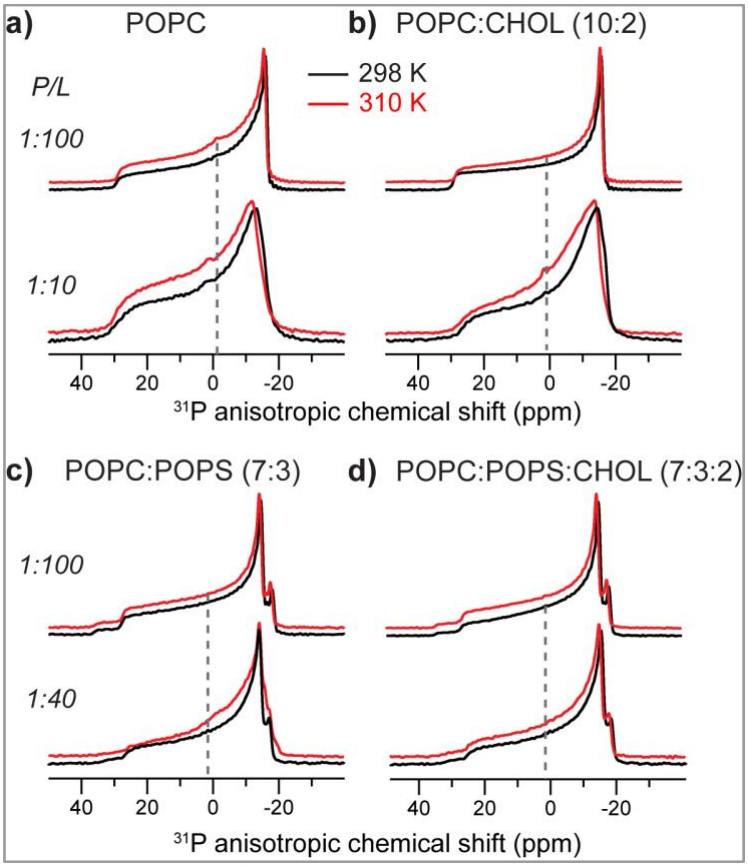

Figure II.3. Static ^{31}P NMR spectra of POPC and POPC : POPS membranes with varying MPER-TMD and cholesterol concentrations.
(**a**) POPC membrane. (**b**) POPC : CHOL (10:2) membrane. (**c**) POPC : POPS (7:3) membrane. (**d**) POPC : POPS : CHOL (7:3:2) membrane. The P/L molar ratios are 1:100, 1:40, or 1:10 as shown on the left of each spectrum. ^{31}P spectra were measured at 298 K (black lines) and 310 K (red lines). Dashed lines guide the eye to the isotropic chemical shift.

The use of POPS also allows us to investigate the effects of negative membrane surface charge on curvature generation. The ^{31}P spectra of POPC : POPS samples with 1:100 peptide reveal two powder patterns, with maximum intensities at −14.6 ppm and −18.1 ppm at 298 K (Fig. II.3 c; Table II.2). Based on the pure POPC spectra, we tentatively assign the smaller CSA to POPC and the larger CSA to POPS. In principle, the different CSAs could result from POPC and POPS phase separation into microdomains, as found in solid-supported POPC : POPS (4:1) bilayers in the presence of 1 mM calcium ions based on scanning force microscopy data [94]. However, differential scanning calorimetry data showed that, in the absence of calcium, PC and PS with similar acyl chains and at PS concentrations of 30 mol% do not phase separate above the phase transition temperature of the individual lipids [95]. Thus, the different ^{31}P CSAs more likely reflect distinct headgroup orientations and conformations of POPC

and POPS [96]. Addition of the peptide broadened the linewidths and obscured the two 90° edges, indicating that the peptide changed the lipid mobilities (*vide infra*).

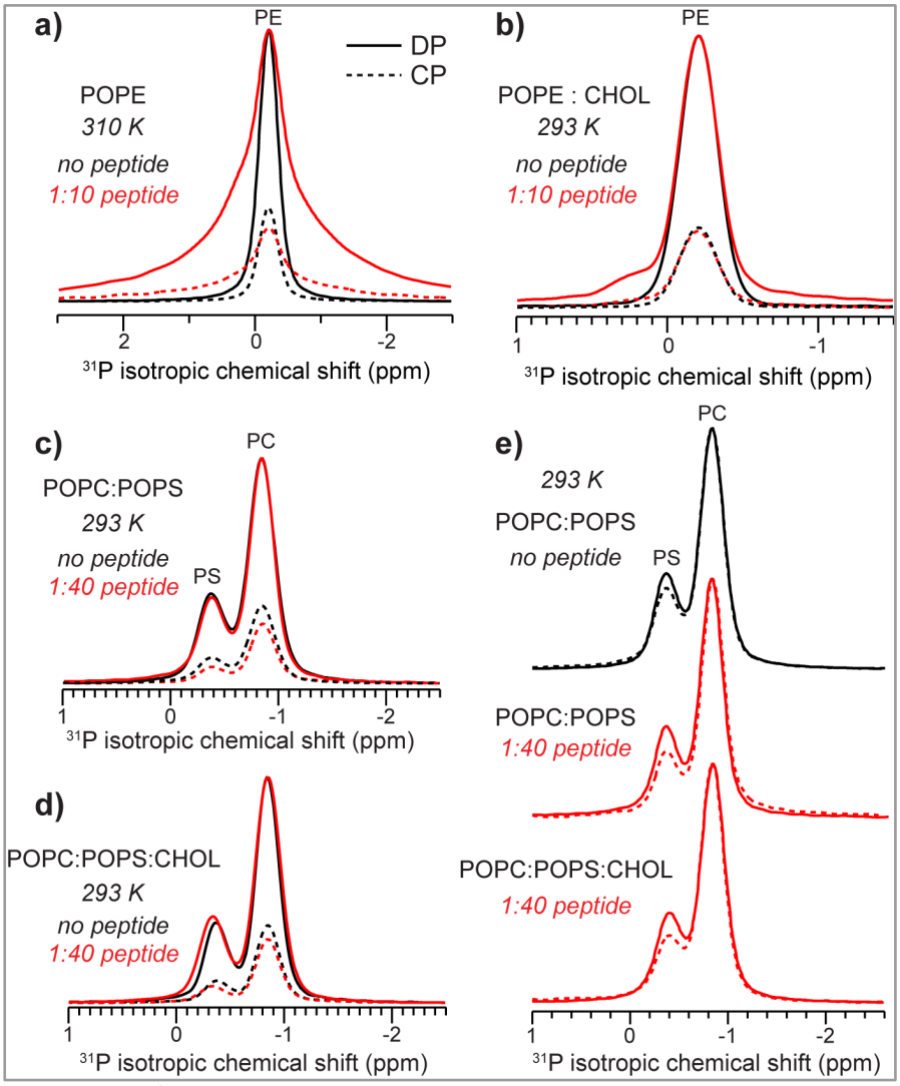

Figure II.4. ^{31}P CP-MAS and DP-MAS spectra showing the effects of the gp41 MPER-TMD on phospholipid dynamics.

The samples were spun at 5 kHz. Peptide-free spectra are shown in black while peptide-containing spectra are shown in red. For each panel, the peptide-free and peptide-containing DP spectra (solid lines) are scaled to match the intensities, so that the different intensities of the CP spectra (dashed lines) indicate the different CP efficiencies of the two samples. (**a**) POPE spectra measured at 310 K. MPER-TMD decreased the CP intensities relative to the DP intensities, indicating that the peptide increased POPE dynamics. (**b**) POPE : CHOL (10:2) spectra measured at 293 K. (**c**) POPC : POPS (7:3) spectra without and with the peptide. The peptide decreased the CP intensities of both POPC and POPS relative to the DP intensities, indicating that it increased lipid dynamics. (**d**) POPC : POPS : CHOL (7:3:2) spectra. The gp41 peptide decreased the CP efficiency like in (**c**). (**e**) DP and CP spectra of three POPC : POPS membranes: POPC : POPS (7:3) without the peptide, POPC : POPS (7:3) membrane with 1:40 peptide, and POPC : POPS : CHOL (7:3:2) with 1:40 peptide. When each pair of spectra are scaled to match the DP and CP intensities of the POPC peak at around -0.84 ppm, the POPS CP intensity decreased relative to the DP intensity, indicating that POPS mobility is preferentially enhanced compared to that of POPC by the peptide.

II.3.c. MPER-TMD increases the mobility of all phospholipids

In addition to membrane curvature, two other features of membrane fusion that have been postulated are increased lipid mobilities and dehydration of the membrane surface in fusion intermediates [97]. The increased lipid mobilities were proposed to result from the membrane curvature at the site of fusion and the disordering effect of the fusion protein. The dehydration barrier against two opposing lipid bilayers results from charge repulsion between polarized water molecules on the two membrane surfaces [9, 59, 98]. To investigate the effects of MPER-TMD on lipid dynamics, we measured ^{31}P DP and CP MAS spectra. The ^{31}P DP spectral intensities reflect the amounts of phospholipids in the sample, while the CP intensities are reduced for dynamic molecules due to motional averaging of the ^{1}H-^{31}P dipolar coupling. Therefore, a lower intensity ratio of CP to DP spectra indicates a higher mobility of phospholipids [99, 100].

Fig. II.4 compares the DP- and CP-MAS spectra of POPE and POPC : POPS membranes without and with MPER-TMD and with and without cholesterol. For the POPE membrane, addition of the peptide reduced the CP/DP intensity ratios at 310 K (**Fig. II.4 a**) and 293 K (data not shown), indicating that MPER-TMD increased the POPE mobility. When cholesterol is present, this intensity change is abolished (**Fig. II.4 b**): the peptide-containing sample exhibits the same CP/DP intensity ratio as the peptide-free membrane, indicating that cholesterol abrogates the peptide's ability to increase the POPE mobility. For POPC : POPS and POPC : POPS : CHOL membranes (**Fig. II.4 c, d**), the peptide lowered the CP intensities relative to the DP intensities, indicating that the peptide increased the dynamics of both POPC and POPS. However, the POPS CP intensities decreased more than those of POPC (**Fig. II.4 e**), indicating that POPS is disordered by gp41 more than POPC is. This observation is consistent with the preferential line broadening of the POPS signal in the static ^{31}P NMR spectra (**Fig. II.3 c**) and MAS DP spectra (**Fig. II.4 d**).

II.3.d. MPER-TMD increases membrane surface hydration

To investigate membrane surface hydration, we measured 2D ^{1}H-^{31}P correlation spectra with ^{1}H spin diffusion under MAS [101]. This experiment selects the dynamic water and lipid ^{1}H magnetization with a ^{1}H T_2 filter, then transfers the magnetization to ^{31}P for detection. The water ^{1}H polarization transfer is mediated by chemical exchange and spin diffusion. For proteoliposome mixtures with exchangeable protons in the lipid headgroup or near the membrane surface, the water-^{31}P cross peak intensity reflects the water accessibility and water dynamics of the membrane surface. Lipid protons also correlate with ^{31}P after spin diffusion [101], and the lipid ^{1}H chemical shifts can be readily assigned based on literature values [102, 103].

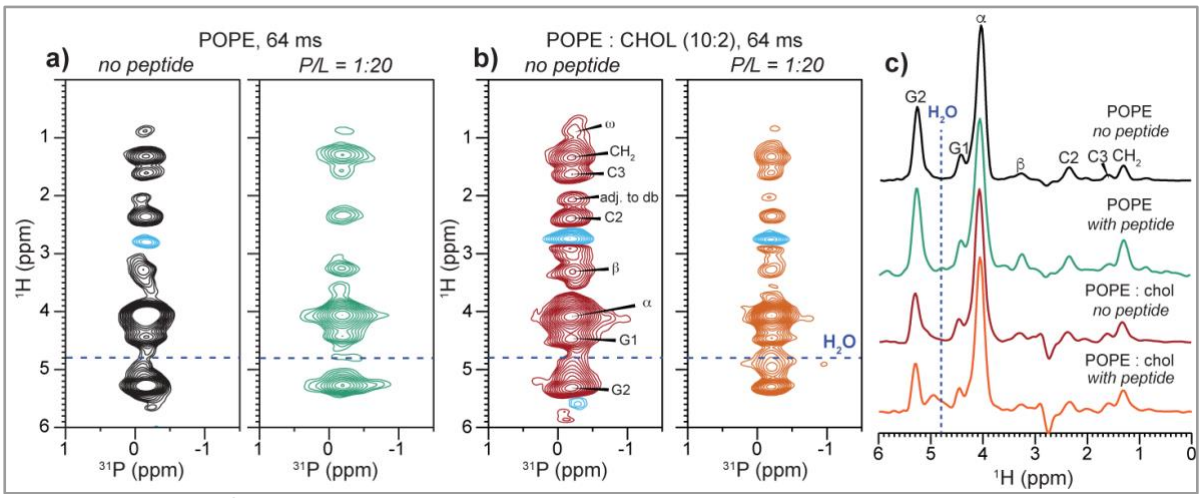

Figure II.5. 2D ^{1}H-^{31}P correlation spectra of POPE and POPE : CHOL (10:2) membranes without and with MPER-TMD, measured with a ^{1}H mixing time of 64 ms at 310 K.
(**a**) POPE membranes without (black) and with (green) the peptide at a P/L of 1/20. (**b**) POPE : CHOL membranes without (red) and with (orange) the peptide at a P/L of 1:20. (**c**) ^{1}H cross sections of the four 2D spectra. The peptide caused a broad water peak only in the membrane containing both the peptide and cholesterol.

Fig. II.5 shows the 2D HETCOR spectra of the POPE and POPE : CHOL (10:2) membranes in the absence and presence of MPER-TMD. With 64 ms ^{1}H mixing, all protons of the lipid headgroup, glycerol backbone, and acyl chains down to the chain-end ω, are detected. The highest cross peak intensities are observed for the headgroup Hα and the glycerol backbone G3, as expected due to their spatial proximity to the phosphate group. No water cross peak is observed for the POPE membranes either with or without the peptide (Fig. II.5 a). This is consistent with the generally low hydration of the POPE membrane surface, as also seen, for example, for POPE membranes containing the PIV5 fusion protein's transmembrane domain [75]. The addition of cholesterol changed the situation: while the peptide-free POPE : CHOL membrane still showed no cross peak, the peptide-bound sample exhibits a clear water cross peak (Fig. II.5 b), indicating increased hydration when both cholesterol and the peptide are present in the membrane. The water peak has a relatively broad linewidth of ~0.3 ppm, which may be attributed to chemical exchange of bound water with the POPE amino group and the low mobility of membrane surface water for the hydrogen-bonded POPE headgroups.

We investigated the hydration of POPC using the same 2D ^{1}H-^{31}P correlation experiment (Fig. II.6). Although the POPC headgroup itself has no exchangeable protons, with a long ^{1}H mixing time of 225 ms and due to relayed polarization transfer through POPS, cholesterol and the peptide, we can still detect water-^{31}P cross peaks [101]. Fig. II.6a–c show that in POPC : POPS membranes with and without cholesterol, the peptide dramatically increased the intensity of the water cross peak intensity to POPC. Similarly, for POPC membranes with and without cholesterol, the addition of MPER-TMD caused a water-^{31}P cross peak, whereas no water cross peak is detected in the absence of the peptide (Fig. II.6 d–f). Water to POPC magnetization transfer can occur as a result of increased membrane surface hydration by the peptide and/or

increased number of labile protons provided by the peptide. However, other viral fusion proteins' hydrophobic domains have been reported to show little water polarization transfer to POPC [104] (vide infra), suggesting that the higher water cross peak detected here likely reflects a true increase of POPC hydration by MPER-TMD.

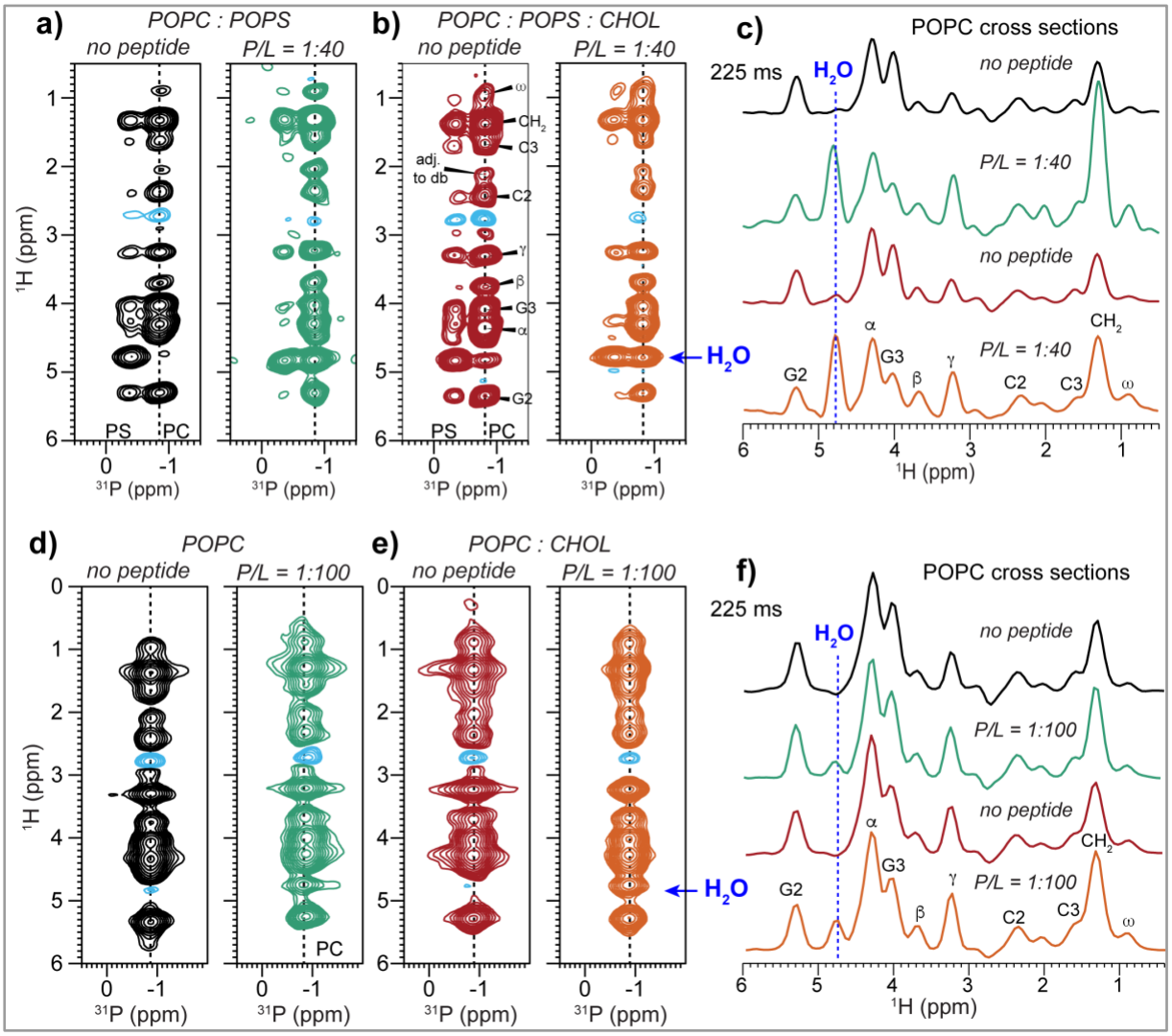

Figure II.6. 2D ^{1}H-^{31}P correlation spectra of POPC : POPS and POPC membranes without and with MPER-TMD.

The spectra were measured with a ^{1}H mixing time of 225 ms at 293 K. (**a**) POPC : POPS (7:3) membranes without and with the peptide. (**b**) POPC : POPS : CHOL (7:3:2) membranes without and with the peptide. (**c**) POPC ^{1}H cross sections of the 2D spectra in (**a**) and (**b**), extracted from a ^{31}P chemical shift of −0.83 ppm (corresponding to POPC). Blue dashed lines guide the eye to the water ^{1}H chemical shift. The peptide-free membranes show no or weak water cross peaks while the peptide-containing samples show strong water cross peaks. (**d**) POPC membranes without and with peptide. (**e**) POPC : CHOL (10:2) membranes without and with peptide. (**f**) POPC ^{1}H cross sections of the 2D spectra in (d) and (e). The peptide moderately increases the water cross peak intensity.

Fig. II.7 shows the 2D 1H-^{31}P correlation spectra of POPC : POPS membranes measured with a shorter ^{1}H spin diffusion mixing time of 25 ms to study POPS hydration. The addition of MPER-TMD clearly increased the water-POPS cross peak

intensities in the CHOL-free POPC : POPS membrane (Fig. II.7 a, b). The presence of cholesterol dampened this hydrating effect by the peptide (Fig. II.7 c, d). To quantify the cross peak intensity changes, we measured the 2D spectra as a function of the ^{1}H mixing time (Fig. II.8). In the cholesterol-free POPC : POPS membrane, the water-POPS cross peak intensity buildup rate clearly increased with the peptide concentration (Fig. II.8 a), indicating that MPER-TMD facilitates POPS hydration in the mixed membrane. However, when cholesterol is present in the membrane, the peptide had a more modest hydration effect (Fig. II.8 b): the water-POPS buildup rates increased with peptide concentration to a smaller extent than in the cholesterol-free membrane.

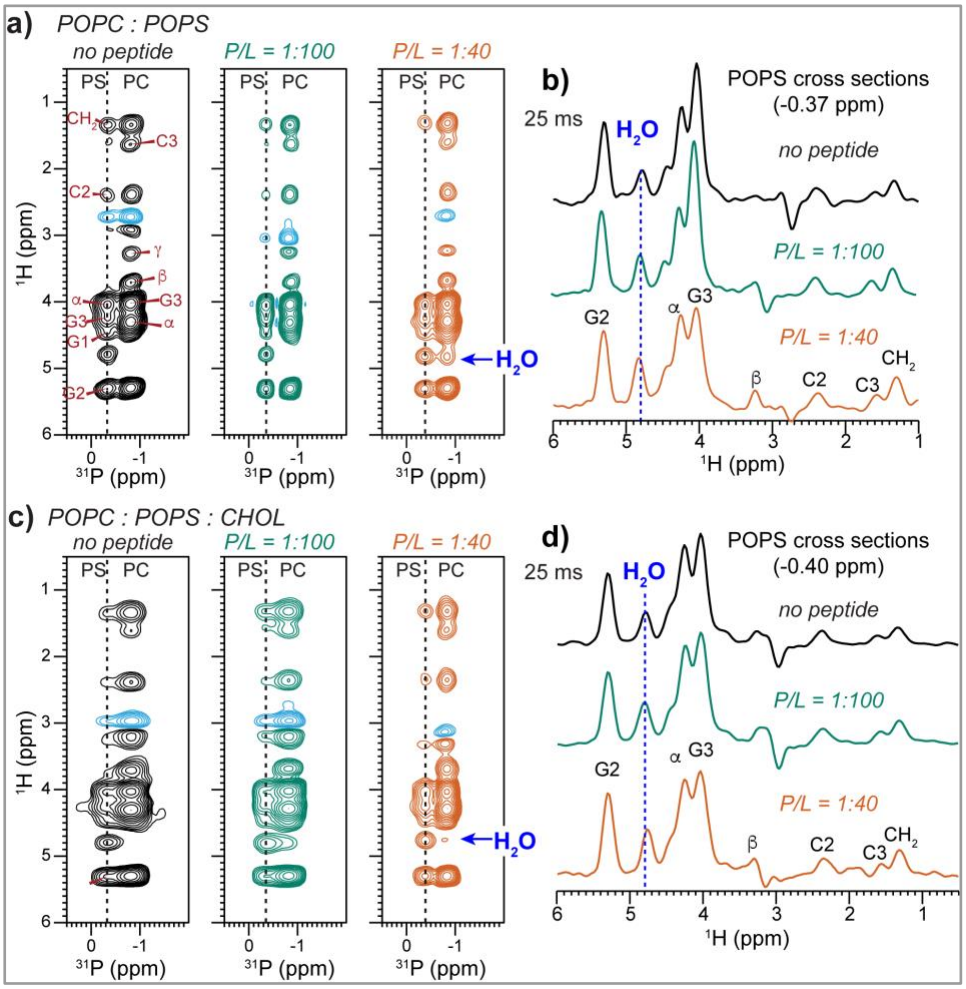

Figure II.7. 2D ^{1}H-^{31}P correlation spectra of POPC : POPS membranes without and with MPER-TMD and with and without cholesterol.

The spectra were measured with a ^{1}H mixing time of 25 ms at 293 K. (**a**) 2D spectra of POPC : POPS membranes without the peptide, with P : L of 1:100 (green) and 1:40 (orange). (**b**) POPS ^{1}H cross sections of the POPC : POPS membranes for the three samples shown in (**a**). (**c**) 2D spectra of POPC : POPS : CHOL (7:3:2) membranes without the peptide, with P : L = 1:100 and 1:40. (**d**) POPS ^{1}H cross sections of the POPC : POPS : CHOL membranes. The peptide moderately increased the water cross peak with POPS.

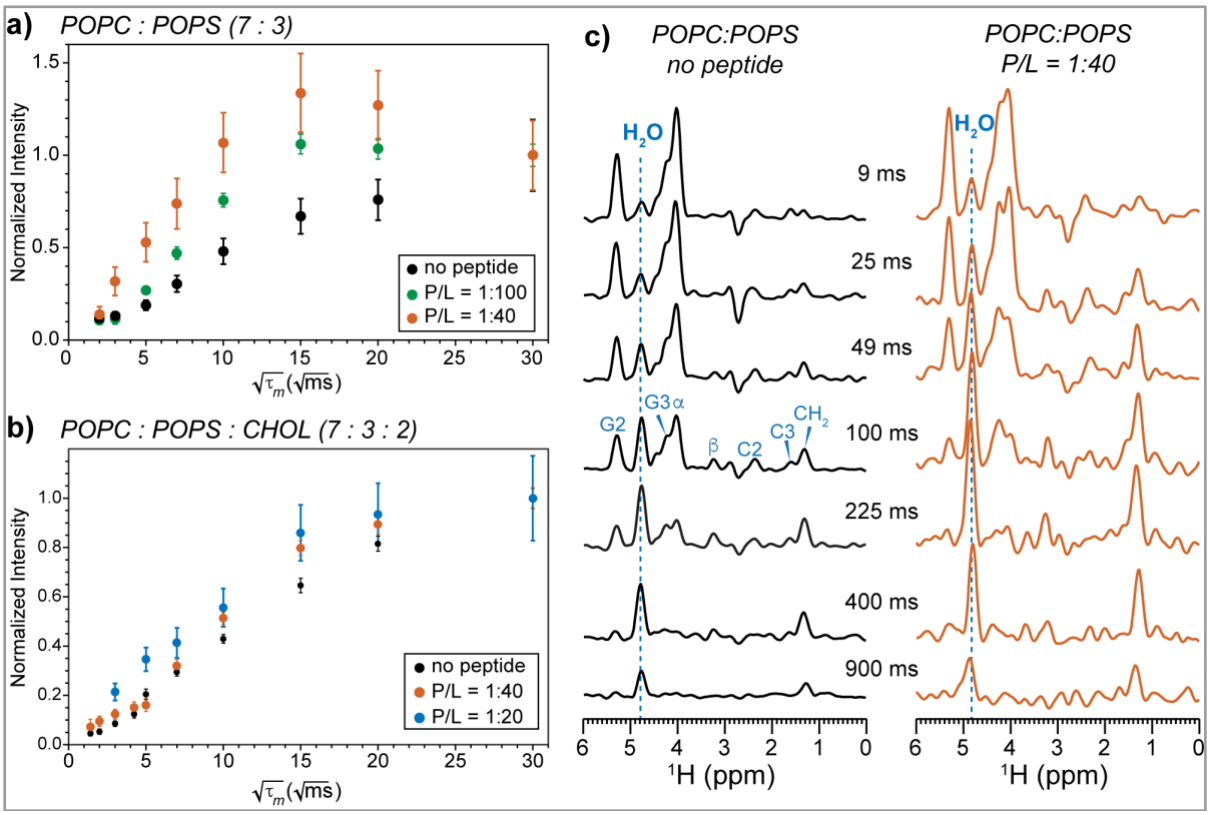

Figure II.8. Water ^{1}H magnetization transfer to POPS in POPC : POPS membranes containing varying concentrations of peptide and cholesterol.
The buildup curves were extracted from 2D ^{1}H-^{31}P HETCOR spectra measured as a function of mixing time. (**a**) Water-POPS ^{1}H-^{31}P cross peak intensities in the POPC : POPS (7:3) membranes without the peptide (black), with 1:100 peptide (green), and 1:40 peptide (orange). Intensities have been corrected for water ^{1}H spin-lattice (T_1) relaxation. Error bars were propagated from the experimental signal-to-noise ratios. (**b**) Water-POPS cross peak intensities in POPC : POPS : CHOL (7:3:2) membranes without the peptide (black) and with 1:40 peptide (orange), and with 1:20 peptide (blue). (**c**) POPS ^{1}H cross sections extracted from the 2D spectra of the POPC : POPS membrane (as in **Fig. II.7**) without the peptide and with peptide (data shown in panel a). Dashed blue lines guide the eye to the water ^{1}H chemical shift.

II.4. Discussion

The ^{31}P NMR data shown above describe several different effects of gp41 MPER-TMD on membrane structure and dynamics. First, static ^{31}P NMR line shapes indicate that POPE is the most conducive phospholipid to NGC formation, while cholesterol counters this curvature induction (**Figs. II.2**, **II.3**). The pronounced NGC of the peptide-containing POPE membrane is consistent with the intrinsic negative curvature of POPE [10], which can promote NGC in concert with the positive membrane curvature created by the surface-bound MPER. In comparison, cholesterol, which also exhibits moderate negative curvature, weakens the nonlamellar morphology, as shown by the attenuated isotropic ^{31}P peak (**Fig. II.2**). This effect suggests that the lipid shape is not the only determinant of NGC formation. We propose that a second factor for POPE-induced NGC is the hydrogen bonding of PE headgroups with each other, which dehydrates the membrane even in the absence of peptides, as seen in 2D ^{1}H-^{31}P correlation spectra (**Fig. II.5 a**).

Our approach deviates from those that replicate the overall lipid composition of the HIV membrane. When POPE is mixed with other lipids, including POPC, POPS, SM, and cholesterol, previous ^{31}P NMR spectra showed that the isotropic ^{31}P peak is largely removed [67][53, 71]. Thus, dilution of the negative-curvature POPE by bilayer-stabilizing lipids attenuates membrane-curvature generation by gp41. The local lipid composition at the site of virus-cell fusion might deviate from the average lipid composition of the plasma membrane and the virus envelope, and might also fluctuate because of the preferential partitioning of gp41 to the boundary of the L_d and L_o phases [80]. Thus, the two- or three-component membrane mixtures examined here give insights into the membrane curvature that would appear when gp41 is surrounded by one or two types of phospholipids.

The bilayer-stabilizing effect of cholesterol may result from the well-known rigidification of the membrane by cholesterol at high temperature. With 17% cholesterol in the POPE membrane (**Fig. II.2 c**), we found that the percentage of nonlamellar morphologies is low except at the highest peptide concentration of P/L = 1:10. In POPC : POPS membranes containing 17% cholesterol, no isotropic peak is observed at P/L ratios up to 1 : 40 (**Fig. II.3 d**). These results indicate that cholesterol weakens the peptide-induced membrane curvature at concentrations above ~17%. Thus, the requirement of cholesterol for membrane fusion and HIV infection [79, 80, 105] might be due to mechanisms other than curvature generation. One mechanism might be regulation of lipid mixing. Cholesterol is known to alter the spatial distributions of lipids in a concentration-dependent manner. High cholesterol concentrations (40–50%) promote homogeneous mixing in normally phase-separated membranes such as DSPC : DPPC mixtures [106] and DOPC : DPPC : CHOL mixtures [107], whereas moderate cholesterol levels promote phase separation. For example, cholesterol creates PC-rich microdomains in polyunsaturated PC : PS : PE mixtures [108]. By separating lipids into multiple phases with different chain orders, cholesterol can increase the hydrophobic mismatch and hence the line tension at the L_d and L_o boundary, thus facilitating fusion. Indeed, total internal reflection fluorescence microscopy data showed that the gp41 FP is localized at the L_d-L_o boundary in phase-separated SM and PS membranes that contain 25% cholesterol [80] and line tension at those boundaries may contribute to fusion [20]. These biophysical data and our ^{31}P NMR results together indicate that the total cholesterol content in the membrane needs to be sufficiently high to support phase separation but not so high as to create a homogeneous membrane. At the same time, the *local* cholesterol concentration near gp41 needs to be moderate to allow curvature induction.

A second mechanism for the requirement of cholesterol for fusion might be the recruitment of gp41 by cholesterol into raft regions of the membrane. A recent solid-state NMR and molecular dynamics simulation study of cholesterol-gp41 interactions found that cholesterol is in molecular contact with the MPER in lipid membranes [53]. Moreover, cholesterol self-associates into dimers and higher-order oligomers in lipid bilayers [54]. Thus, cholesterol could serve to bring multiple gp41 trimers into close proximity (**Fig. II.1**), facilitating virus-cell fusion. Finally, a biological mechanism by

which cholesterol might mediate membrane fusion is that the cell-surface receptors recognized by Env reside in cholesterol-rich domains, so cholesterol depletion may inhibit gp120 binding to the receptors [81, 109].

It is of interest to compare the curvature-inducing ability of gp41 MPER-TMD with that of other peptides involved in membrane fusion, such as gp41 FP and the PIV5 F protein's FP and TMD. ^{31}P NMR spectra of membranes containing these peptides indicate that MPER-TMD has weaker curvature-inducing ability than the HIV and PIV5 fusion peptides but similar curvature-inducing ability to the PIV5 TMD. The gp41 FP induced an isotropic peak to the static ^{31}P spectrum of an equimolar DOPC : DOPE : CHOL mixture, but did not induce an isotropic peak in the static spectrum of a virus-mimetic membrane (LM3) with less PE [84]. Thus, PE is synergistic with FP in causing membrane curvature. The gp41 FP induced an isotropic peak at a low P/L ratio of 1:50, indicating that it is more effective than the MPER-TMD in causing membrane curvature. The PIV5 FP generated high curvature to POPC membranes at a P/L of 1:15 [104] while MPER-TMD did not cause curvature to POPC membranes even at a higher P/L of 1:10. The influenza M2 protein, which has membrane scission activity, causes NGC in 30% cholesterol membranes at a P/L ratio of 1:15 [110]. In comparison, gp41 MPER-TMD has no such ability in the 33% cholesterol POPE membrane at a P/L ratio of 1:10, indicating that not all curvature-inducing peptides respond to cholesterol the same way. The PIV5 fusion protein TMD has a similar ability to gp41 MPER-TMD to cause curvature to PE membranes [75]. However, the PIV5 TMD does not possess a membrane-surface domain. Instead, its Val and Ile rich sequence adopts an unusual strand-helix-strand conformation, which was hypothesized to promote membrane curvature. Therefore, both the primary sequence and the three-dimensional structure impact membrane-curvature generation by these viral fusion protein hydrophobic domains.

The second conclusion from the current data is that gp41 MPER-TMD increases the dynamic disorder of multiple phospholipids, including PC, PE and PS. This is manifested by the lower CP intensities of the ^{31}P spectra relative to the DP spectra in the peptide-bound membranes, compared to peptide-free membranes (**Fig. II.4**). The increased lipid mobility and disorder is expected for fusion intermediates. Since POPE resides in high-curvature membranes, we interpret the increased dynamic disorder as due to faster reorientation of POPE. In comparison, POPS exhibits the lowest CP intensities among the three phospholipids and its static linewidth also appears to be preferentially broadened by the peptide (**Figs. II.3 c** and **II.4 d**). These observations suggest that POPS may undergo slower, intermediate-timescale, motion in the presence of the peptide. This interpretation is consistent with a model where electrostatic attraction between negatively charged POPS headgroups and positively charged K665 and K683 in the MPER might slow POPS motion relative to POPC and POPE.

The third finding of the current data is that MPER-TMD increased, rather than decreased, the hydration of all phospholipids, irrespective of membrane curvature. This hydration effect is manifested by the higher water-^{31}P cross peaks in 2D ^{1}H-^{31}P

correlation spectra (Figs. II.5, II.6, II.7) and faster water to POPS ^{1}H magnetization transfer rates (Fig. II.8). This enhanced water polarization transfer to lipids occurs *despite* the faster lipid motion. The POPE and POPS headgroups both contain exchangeable NH protons, thus water polarization transfer can proceed efficiently through chemical exchange and spin diffusion, regardless of the peptide. Both POPE and POPS showed higher cross peaks with water when the peptide is present, indicating increased hydration of the membrane surface. This increased hydration is opposite to the expectation for membrane fusion in the absence of proteins [98], where water expulsion is thought to be a necessary high-energy step. Instead, our data support a model wherein gp41 MPER-TMD reduces the dehydration energy barrier by coating the membrane surface with the MPER helices [67]. This potential alteration of the free energy of protein-free membrane fusion by reducing the dehydration barrier has also been proposed for other viral fusion proteins such as the PIV5 FP [28].

For gp41 MPER-TMD, another possible reason for the higher membrane hydration is the presence of a cationic arginine, R696, in the middle of the TMD (Fig. II.1). Hydrogen-deuterium exchange NMR data show that the C-terminal TMD residues are more accessible to water than the N-terminal residues [36]. This water pathway in the trimeric helical bundle might increase the membrane's hydration. Interestingly, MD simulations of the gp41 TMD in DPPC and DPPC : CHOL membranes reported fluctuations of membrane thickness up to 7 Å, which correlate with a water defect near the Arg residue [111]. Moreover, this water defect is better localized in the cholesterol-containing membrane than in the cholesterol-free membrane. Thus, gp41 MPER-TMD might increase membrane hydration through the cationic R696.

The membrane-hydrating effect of gp41 MPER-TMD is the opposite of the effect of the PIV5 fusion protein on the membrane. Based on 2D ^{1}H-^{31}P correlation NMR spectra, we found that the PIV5 FP dehydrates POPC [104] and DOPE membranes [29] but hydrates the POPC : POPG membrane. This trend correlates with the secondary structure of the PIV5 FP: the more α-helical the peptide, the higher the membrane hydration. For the PIV5 fusion protein TMD, the peptide maintains the hydration of POPC and POPC : POPG membranes but dehydrates the POPE membrane, in which the TMD adopts the β-strand conformation [75]. Thus, for both the FP and TMD of the PIV5 fusion protein, the β-sheet conformation is correlated with membrane dehydration. In comparison, the α-helical gp41 MPER-TMD hydrates the membrane, and the gp41 chimera that covalently links the FP and MPER-TMD also increases membrane surface hydration [71]. Taken together, these data suggest that α-helical fusion protein domains maintain and even increase the hydration of membrane surfaces. Only when β-strand conformations coat the membrane surface is dehydration observed.

In conclusion, the current ^{31}P solid-state NMR study shows that gp41 MPER-TMD relies on PE to induce the negative-Gaussian curvature that is required for hemifusion intermediates and fusion pores. This curvature-inducing action is accompanied by the peptide's ability to increase the dynamic disorder of the lipids, and by the attenuation of the dehydration barrier, both facilitating membrane merger. The observed bilayer-stabilizing effects of cholesterol suggest that cholesterol may not be

enriched at the fusion site, which is consistent with biochemical finding that HIV-cell fusion occurs at the boundary between cholesterol-rich and cholesterol-poor regions of the membrane. Future elucidation of the molecular mechanism and pathway of Env-mediated HIV-cell membrane fusion should take into account the specific peptide-lipid interactions observed here.

Acknowledgment

This work is supported by NIH grant GM066976 to M.H. This study made use of NMR spectrometers at the MIT-Harvard Center for Magnetic Resonance, which is supported by NIH grant P41 GM132079.

Conclusion: Assembling the puzzle

In this chapter, we have shown that the MPER-TMD region of gp41 increases the mobility of individual molecules (**Section II.3.c**) and introduces more water into the bilayer (likely through a membrane lipid packing defect; **Section II.3.d**). This validates the physical disruption mode of catalysis mentioned in **Section I.2.e**). We further showed that POPE membranes with and without a small amount of cholesterol, gp41 MPER-TMD can induce membrane curvature on its own (**Section II.3.a**), as discussed in **Section I.2.a**. The intriguing finding that cholesterol attenuates some of these gp41 functions suggests the possibility that gp41 may act differently between L_o and L_d domains, leaving open the possibility that gp41 alters line tension at the L_o-L_d domain boundaries (see **Section I.2.b**). This idea will be discussed further in the next study (**Chapter III**).

III. Cholesterol-mediated clustering of the HIV fusion protein gp41 in lipid bilayers

By Nhi Tran, Younghoon Oh, Madeleine Sutherland, Qiang Cui, and Mei Hong; revised for *J. Mol. Biol.*, October 26, 2021

III. Abstract

The envelope glycoprotein (Env) of the human immunodeficient virus (HIV-1) is known to cluster on the viral membrane surface to attach to target cells and cause membrane fusion for HIV-1 infection. However, the molecular structural mechanisms that drive Env clustering remain opaque. Here, we use solid-state NMR spectroscopy and molecular dynamics (MD) simulations to investigate nanometer-scale clustering of the membrane-proximal external region (MPER) and transmembrane domain (TMD) of gp41, the fusion protein component of Env. Using ^{19}F solid-state NMR experiments of mixed fluorinated peptides, we show that MPER-TMD trimers form clusters with interdigitated MPER helices in cholesterol-containing membranes. Inter-trimer ^{19}F-^{19}F cross peaks, which are indicative of spatial contacts within ~2 nm, are observed in cholesterol-rich virus-mimetic membranes but are suppressed in cholesterol-free model membranes. Water-peptide and lipid-peptide cross peaks in 2D ^{1}H-^{19}F correlation spectra indicate that the MPER is well embedded in model phosphocholine membranes but is more exposed to the surface of the virus-mimetic membrane. These experimental results are reproduced in coarse-grained and atomistic molecular dynamics simulations, which suggest that the effects of cholesterol on gp41 clustering is likely via indirect modulation of the MPER orientation. Cholesterol binding to the helix-turn-helix region of the MPER-TMD causes a parallel orientation of the MPER with the membrane surface, thus allowing MPERs of neighboring trimers to interact with each other to cause clustering. These solid-state NMR data and molecular dynamics simulations suggest that MPER and cholesterol cooperatively govern the clustering of gp41 trimers during virus-cell membrane fusion.

III.1. Introduction

HIV-1 entry into cells is mediated by the surface envelope glycoprotein Env, which consists of trimeric assemblies of gp120 and gp41 heterodimers [112]. Following attachment of gp120 to cell-surface receptors, gp41 undergoes large conformational changes to fuse the target cell membrane with the virus envelope. However, each HIV-1 particle contains only 7 to 14 copies of Env, in contrast to other enveloped viruses such as alphaviruses and influenza, which contain many more entry proteins [113, 114]. It has long been hypothesized that the low copy number of the HIV-1 entry protein may be compensated by a local clustering of the Env to accomplish the necessary membrane curvature for virus-cell fusion. Indeed, super-resolution microscopy and electron tomography data have captured Env clusters on the surface of the HIV-1 envelope and during virus-cell membrane fusion [115-117], and this clustering correlates with HIV-1 infectivity.

While the existence of Env clustering has been demonstrated by microscopy data, the molecular mechanism of this clustering is not yet well understood. So far, Env clustering has been investigated largely in terms of Env interaction with other HIV-1 proteins and with host cell receptors. In immature and non-infectious HIV-1 particles, the structural polyprotein Gag interacts with Env through the cytoplasmic tail (CT) of gp41. Disassembly of the Gag lattice during HIV-1 maturation allows Env diffusion in the lipid envelope to form clusters that engage with cell surface receptors [116, 117]. The gp41 CT also interacts with cholesterol, which may promote Env clustering to the cholesterol-rich domains of the lipid membrane [118]. Despite the role of the CT in HIV-1 maturation, CT-truncated Env may still be able to cluster in the membrane, since immature HIV-1 particles containing CT-truncated Env have been shown to have partial entry capability [116, 119, 120]. This observation suggests that alternative domains in gp41 may play important roles in Env clustering, independent of the cytoplasmic tail.

Gp41 contains a highly conserved membrane-proximal external region (MPER) immediately N-terminal to the transmembrane domain (TMD). This MPER forms an amphipathic α-helix on the surface of the lipid membrane [67, 121], and is required for viral membrane fusion. Biochemical studies showed that MPER peptides are able to destabilize lipid membranes and play a role in mediating lipid mixing during membrane fusion [122]. Analysis of ^{1}H and ^{13}C chemical shifts of POPC in the absence and presence of cholesterol and a pentapeptide of the MPER domain suggested that cholesterol promotes the insertion of this pentapeptide into the lipid membrane, and the peptide in turn sequesters cholesterol [123]. Fluorescence microscopy data showed that the MPER preferentially localizes to the boundaries of cholesterol-rich ordered phases [124]. Very recently, solid-state NMR data and MD simulations found that cholesterol molecules bind to the MPER-TMD peptides in lipid bilayers [125]. Together, these results suggest that cholesterol, which is required for HIV-1 infectivity [79, 105, 126, 127], might recruit MPER to raft-like lipid domains, in doing so causing clustering of the Env trimers.

Here we directly investigate the nanometer-scale separation of MPER-TMD trimers in lipid bilayers using 2D ^{19}F solid-state NMR experiments and molecular

dynamics simulations. We prepared membrane samples with peptide/lipid molar ratios (P/L) of 1:10 to 1:32. At these peptide concentrations, previous ^{19}F spin-counting experiments showed that the MPER-TMD peptides are fully trimerized [67]. But whether the trimers cluster in space was not known. We now show that multiple MPER-TMD trimers indeed self-associate on the nanometer scale, and we provide direct experimental evidence for the dependence of this clustering on membrane cholesterol as well as constraints on the geometry of the clustered trimers.

III.2. Materials and Methods

III.2.a. Synthesis and purification of isotopically labeled gp41 MPER-TMD

The MPER-TMD peptide used in this study corresponds to residues 661-704 of HIV-1 clade D gp41. The amino acid sequence is ^{661}LELDKWASLW NWFNITNWLW YIRLFISIVG GLVGLRIVFA VLSI^{704}. This sequence is similar to the peptide used in our recent study of gp41 interaction with cholesterol [125], except that we replaced M687 with Ser to prevent oxidation during peptide cleavage. Four fluorinated peptides were synthesized, each containing a single fluorinated residue at 4-CF_3-F673, 5-^{19}F-W670, 5-^{19}F-W666, and 4-CF_3-F663 (**Table III.1**). For the 4-CF_3-F673 labeled peptide, ^{13}C, ^{15}N-labeled L684 was also incorporated. For the 4-CF_3-F663 labeled peptide, U-^{13}C, ^{15}N-labeled I675 and L679 were also incorporated. These ^{13}C, ^{15}N labeled residues serve to verify the secondary structure of the peptide. The 5-^{19}F-W670 labeled peptide and 4-CF_3-F673 peptide were mixed in a 1:1 molar ratio to produce membrane samples 1 – 4. The 5-^{19}F-W666 labeled peptide and 4-CF_3-F663 labeled peptide were mixed in a 1:1 molar ratio to produce samples 5 and 6.

These MPER-TMD peptides were synthesized on a custom-built fast-flow peptide synthesizer [128] using Fmoc solid-phase peptide synthesis protocols. Synthesis proceeded at 70°C, with N, N-dimethylformamide (DMF) and the deprotection solution (25% piperidine) delivered at 20 ml/min. About 100 mg H-rink amide ChemMatrix resin with a loading of 0.5 mmol/g was swelled in the reaction vessel with DMF for 5 min. Fmoc-protected amino acids were activated with 1-[Bis(dimethylamino)methylene]-^{1}H-1,2,3-triazolo[4,5-b]pyridinium 3-oxide hexafluoro-phosphate (HATU) and N, N-Diisopropylethylamine (DIEA) prior to coupling with resin. The synthesis scale was 0.05 mmol, and ten-fold excess of unlabeled amino acids and four-fold excess of isotopically labeled amino acids were singly and triply coupled, respectively, using a coupling time of 50 and 70 s. The peptide was cleaved from the resin with TFA/phenol/H_2O/TIPS (88:5:5:2 v/v) for 3 h at room temperature. The resin was then filtered off and the crude peptide was precipitated and washed three times with chilled diethyl ether. The crude peptide was dried under vacuum overnight at room temperature.

Table III.1. HIV gp41 MPER-TMD peptides and membrane samples used in this study
In the sequences, residues given ^{19}F labels are bolded, underlined and in red. The U-^{13}C/^{15}N labeled residues are bolded and underlined.

Mixed peptide 1:

```
661        670        680        690        700
LELDKWASL WNWFNITNWL WYIRLFISIV GGLVGLRIVF AVLSI
LELDKWASL WNWFNITNWL WYIRLFISIV GGLVGLRIVF AVLSI
```

Membrane Samples	Peptide : Lipid : Chol molar ratio	Membrane composition
1	1:30:13	$VMS^{cluster}$
2	1:32:0	DMPC
3	1:10:4.5	VMS
4	1:32:0	POPE

Mixed peptide 2:

```
661        670        680        690        700
LEFDKWASL WNWFNITNWL WYIRLFISIV GGLVGLRIVF AVLSI
LEFDKWASL WNWFNITNWL WYIRLFISIV GGLVGLRIVF AVLSI
```

Membrane Samples	Peptide : Lipid : Chol molar ratio	Membrane composition
5	1:30:13	$VMS^{cluster}$
6	1:32:0	DMPC

Crude gp41 peptide was dissolved in trifluoroethanol (TFE) and purified by preparative reverse-phase HPLC using an organic solvent mixture/H_2O gradient. Solvent pumps A and B delivered 25:75 v/v acetonitrile : isopropanol in channel A and water in channel B at 15 ml/min. An isocratic gradient (5% A) was applied for one column volume (CV), followed by an initial linear gradient (5-60% A) over four CVs, and a final linear gradient (60-100% A) over 9 CVs. MALDI-MS was used to validate the peptide purity, with the measured masses showing good agreement with the calculated masses. The total yield of the peptide after purification was 15-20 mg (~8 %).

III.2.b. Membrane sample preparation

The gp41(661-704) peptides were reconstituted into virus-mimetic phospholipid membranes ($VMS^{cluster}$ and VMS), which consists of 1-palmitoyl-2-oleyl-sn-glycerol-3-phosphocholine (POPC), 1-palmitoyl-2-oleoyl-sn-glycero-3-phosphoethanolamine (POPE), 1-palmitoyl-2-oleoyl-sn-glycero-3-phospho-L-serine (POPS), sphingomyelin (SM), and cholesterol (chol). The POPC : POPE : POPS : SM : chol molar ratios are 15:20:15:20:30 for the $VMS^{cluster}$ membrane and 30:15:15:10:30 for the VMS membrane. The $VMS^{cluster}$ membrane was designed to mimic the lipid compositions of the HIV envelope [83, 85, 129], whereas the VMS membrane is more similar to the plasma membrane lipid composition. Two membrane samples (samples 1 and 5) were prepared with the $VMS^{cluster}$ membrane, where the peptide : (total phospholipid and SM) : chol molar ratio (P/L/C) was 1:30:13 (**Table III.1**). Control samples (samples 2 and 6) were prepared with the same peptides reconstituted in DMPC membranes at a P/L/C ratio of 1:32:0. Comparisons between samples 1 and 2 and between samples 5 and 6

allow us to investigate how the complex virus-mimetic membrane affects MPER-TMD trimer association. A VMS membrane sample (sample 3) with a higher P/L ratio of 1:10 was prepared to serve as a positive control for clustering, whereas a POPE sample (sample 4) with a P/L ratio of 1:32 further explores the impact of lipids on MPER-TMD clustering.

Phospholipids and SM were dissolved in chloroform and cholesterol was dissolved in a chloroform/methanol mixture. The peptides were dissolved in TFE and mixed with the lipid solution. The organic solvent was removed under nitrogen gas until a thin, dried lipid/peptide film was formed. This film was resuspended in HEPES buffer (10 mM HEPES, pH 7.5, 1 mM EDTA, 0.1 mM NaN_3) and subjected to ten freeze-thaw cycles between liquid nitrogen and a 45°C water bath to form homogenous multilamellar vesicles. The proteoliposome solution was dialyzed against the buffer (pH 7.5) for 2.5 days with five buffer changes to remove residual TFE. The proteoliposomes were spun at 55,000 rpm using a Beckman SW60T rotor at 4°C for 17 hours to obtain membrane pellets. The pellets were incubated in a desiccator until they reached a hydration level of ~40 wt% water and were then spun into magic-angle spinning (MAS) rotors for solid-state NMR experiments. Most membrane samples contained ~8 mg peptide, 30-40 mg

Table III.2. Parameters of the solid-state NMR experiments on the gp41 MPER-TMD membrane samples.

Experiment	NMR Parameters	Experimental Time	Membrane Samples
rotor synchronized 2D FF CORD	B_0 = 9.4 T, T_{set}=243 K, ν_{MAS}=10.332 kHz, SWH1 = 10.332 kHz, SWH2 = 93.75 kHz, ^{19}F carrier frequency = -68 ppm, ns=640, τ_{rd}=1.7 s, $t_{1,max}$= 1.65 ms, $t_{1,inc}$= 96.78 μs, τ_{dwell}=5.3 μs, τ_{acq} = 4.3 ms, τ_{HF}=1 ms, τ_{CORD} = 500 ms, $\nu_{1H,acq}$ =71.4 kHz	40 hrs each	1, 2, 5
		80 hrs	6
2D FF CORD	B_0 = 9.4 T, T_{set}=238-243 K, ν_{MAS}=10.0 kHz, SWH1 = 75 kHz, SWH1 = 93.75 kHz, ^{19}F carrier frequency = -83.6 ppm, ns=256-320, τ_{rd}=2 s, $t_{1,max}$= 0.7 ms, $t_{1,inc}$= 13.31 μs, τ_{dwell}=5.3 μs, τ_{acq} = 3.1 – 4.3 ms, τ_{HF}= 750 μs, τ_{CORD} = 500 ms, $\nu_{1H,acq}$ =35-50 kHz	89 hrs	3
		71 hrs	4
2D ^{1}H-^{19}F HETCOR with 100 ms ^{1}H spin diffusion	B_0 = 9.4 T, T_{set} (samples 1 and 5) = 275 K, T_{set} (samples 2 and 6) = 290 K, ν_{MAS}=9 kHz, SWH1 = 5 kHz, SWH1 = 93.75 kHz, ^{19}F carrier frequency = -83.6 ppm, ns=1024, τ_{rd}=1.5 s, $t_{1,max}$= 4.8 ms, $t_{1,inc}$= 200 us, τ_{dwell}=5.3 μs, τ_{acq} = 4.3 ms, τ_{HF}= 1 ms, T_2-filter duration = 222 μs, τ_{mix} = 100 ms, $\nu_{1H,acq}$=35-62.5 kHz	22 hrs each	1, 2
		45 hrs	5
		89 hrs	6

Symbols: B_0 = magnetic field; T_{set} = thermocouple-reported bearing gas temperature; ν_{MAS} = MAS frequency; SWH1: spectral width of the ω_1 dimension of the 2D spectra; SWH2: spectral width of the ω_2 dimension of the 2D spectra; ns = number of scans per t_1 slice of the 2D spectra; τ_{rd} = recycle delay; $t_{1,max}$ = maximum t_1 evolution time; $t_{1,inc}$ = increment or dwell time for the t_1 evolution period; τ_{dwell} = dwell time during direct acquisition of the FID; τ_{acq} = maximum acquisition time during direct detection; τ_{HF} = ^{1}H-^{19}F cross polarization contact time; τ_{CORD} = CORD mixing time. $\nu_{1H,\ acq}$ = ^{1}H decoupling field strength during detection.

lipids, and ~30 mg water. The high-concentration VMS sample (sample 3) contained ~5 mg peptide, ~10 mg lipids, and ~10 mg water.

III.2.c. Solid-state NMR spectroscopy

Solid-state NMR spectra were measured on a Bruker AVANCE III HD spectrometer at 9.4 T (400 MHz ^{1}H Larmor frequency) using a 4 mm HFX MAS probe. ^{19}F chemical shifts were externally referenced to the ^{19}F signal of Teflon at -122 ppm on the $CFCl_3$ scale. ^{13}C chemical shifts were externally referenced to the $^{13}C\alpha$ signal of glycine at 43.65 ppm on the tetramethylsilane scale. Typical radiofrequency (rf) field strengths were 62.5 kHz for ^{19}F and ^{13}C pulses, and 50-62.5 kHz for ^{1}H decoupling using the two-pulse phase-modulated (TPPM) sequence [130]. 1D ^{19}F cross-polarization (CP) spectra were measured at 303 K to 243 K under 10 kHz MAS.

2D ^{19}F-^{19}F correlation spectra were measured with a CORD [40] mixing time of 500 ms to investigate intermolecular contacts between MPER-TMD trimers (**Table III.2**). To freeze protein motion, we measured most of these spectra at 243 K, except for the VMS sample (sample 3), which was measured at 238 K. The MAS frequencies were 10.0 and 10.332 kHz. For 2D spectra measured under 10.332 kHz MAS, the indirect dimension was rotor-synchronized to remove spinning sidebands and hence increase spectral sensitivity. The spectral width of 10.332 kHz corresponds to a ^{19}F chemical shift range of 27.5 ppm. The ^{19}F carrier frequency was set to -68 ppm for these experiments, thus the 5-^{19}F-W670 and 5-^{19}F-W666 peaks at -125 ppm are folded to -70 ppm in the indirect dimension, whereas the CF_3 signal of F673 and F663 appears at its true isotropic chemical shift of -62 ppm.

III.2.d. Molecular dynamics simulations

To probe the effect of cholesterol on the conformation and association of gp41 trimers, we conducted coarse-grained (CG) and all-atom molecular dynamics simulations. Most of the discussions in the main text center on all-atom simulations, whereas the CG simulation details and results are summarized in the SI (Fig. S1, Fig. S2).

Table III.3. Membrane compositions and simulation temperatures for the systems studied with all-atom molecular dynamics simulations.

Membrane Model	Peptide : Lipid : Chol mole ratios	gp41 model and simulation temperature	
		A single trimer	Dimer of trimers
$VMS^{cluster}$	1 : 70 : 30	303 K, 280 K	303 K, 280 K
$VMS^{cluster}$ without cholesterol	1 : 93 : 0	303 K, 280 K	303 K, 280 K
DMPC	1 : 87 : 0	303 K, 280 K	303 K, 280 K

Three different membrane models were used in the simulations, including the $VMS^{cluster}$ membrane and the DMPC membrane used in the solid-state NMR experiments, and a $VMS^{cluster}$ membrane without cholesterol (**Table III.3**). The $VMS^{cluster}$ membrane contains POPC, POPE, POPS, PSM, and cholesterol with molar ratios of 15:20:15:20:30. To further understand the effect of cholesterol, we also compare the simulation results for $VMS^{cluster}$ membranes with and without cholesterols. For each membrane composition, two models of the MPER-TMD trimer were analyzed: a single trimer and a dimer of trimers. The structural model of the single trimer was adopted from the recent solid-state NMR study (PDB: 6DLN) [67], whereas the initial positions of the trimers in the dimer-of-trimer model were obtained from CG simulations. As described in the SI, these CG simulations revealed spontaneous clustering of the MPER-TMD trimers into three distinct geometries (Fig. S1). We then used all-atom simulations to further examine the dimer model that features the most extensive gp41-gp41 contacts and to probe the effects of cholesterol on trimer clustering.

In all-atom simulations of both single trimer and dimer-of-trimer models, the peptide : lipid molar ratio is lower than that in the solid-state NMR experiments **in order** to avoid self-association of the trimers through periodic boundary images. Since many solid-state NMR experiments were conducted at low temperatures, we conducted MD simulations at both 303 K and 280 K to better compare the simulations with the NMR results, as well as to probe the physiological relevance of the observed clustering.

Initial configurations for MD simulations were built using CHARMM-GUI [131, 132]. The protein-lipid systems were solvated with a 22.5-Å thick water layer on each side of the lipid bilayer. The gp41 trimers are placed in the lipid bilayer in a single orientation, with all MPER motifs interacting with the same membrane leaflet, to mimic the situation in the virus membrane. The CHARMM36 force field [133, 134] and the TIP3P model [135] were used to describe protein-lipid mixture and water, respectively. Na^+ and Cl^- ions were introduced to neutralize the system and maintain a concentration of 150 mM. All systems were equilibrated for at least 300 ns with the Highly Mobile Membrane Mimetic (HMMM) model [136] to facilitate the re-distribution of membrane components around the protein. Three configurations from the HMMM simulation were randomly selected, then converted to full-chain lipid membrane systems using CHARMM-GUI [137] and equilibrated for another 100 ns. During HMMM and equilibration following the conversion to full-chain lipids, all heavy atoms of the proteins were subjected to weak restraints. The production runs were free of any restraints and lasted for at least 200 ns for each system and the initial configuration. To help verify the robustness of the observed trends, especially the impact of cholesterol on the association of gp41 trimers, we also conducted dimer-of-trimer simulations in DMPC and cholesterol-free $VMS^{cluster}$ membranes, by starting with the tight dimer structure obtained by the end of MD simulations of the $VMS^{cluster}$ membrane.

All HMMM, equilibration and production simulations were performed under constant pressure and temperature using the Parrinello-Rahman barostat [138] and Nosè-Hoover thermostat [139, 140]. Bonds involving hydrogen atoms were constrained

using the LINCS algorithm [141], which enables an integration time step of 2 fs. All simulations were carried out using the GROMACS-2018.3 simulation package [142].

III.3. Results

III.3.a. MPER-TMD trimers co-localize in cholesterol-containing membranes

To investigate whether the MPER-TMD trimers cluster on the nanometer scale in lipid bilayers, we employed 2D ^{19}F-^{19}F spin diffusion correlation experiments. ^{19}F spin diffusion is able to detect distances up to ~2 nm due to the high gyromagnetic ratio of the ^{19}F spin and the resulting strong dipolar couplings [51]. Thus, if the fluorinated MPER residues from different trimers approach each other to within ~2 nm, we should observe inter-trimer correlation peaks. Most membrane samples prepared in this study have a peptide monomer : lipid molar ratio of about 1:30 (**Table III.1**). This peptide concentration was chosen to allow sufficient separation between the MPER-TMD trimers if they are homogeneously distributed in the membrane while still permitting enough sensitivity for the NMR experiments. To investigate whether peptide clustering depends on the lipid composition of the membrane, we compare MPER-TMD bound to a cholesterol-containing virus-mimetic membrane (VMS^{cluster}) versus the one-component DMPC and POPE membranes.

To maximally ensure that the measured intermolecular ^{19}F-^{19}F distances are between different trimers rather than within each trimer, we placed fluorinated residues at the N-terminal end of the MPER in one pair of mixed labeled samples and in the middle of the MPER helix in the other pair of mixed labeled samples. The first mixed-labeled sample contains 5-F-W670 and 4-CF_3-F673 while the second mixed-labeled sample contains 5F-W666 and 4-CF_3-F663 (**Fig. III.1**, **Table III.1**). Based on a recently reported solid-state NMR structural model of trimeric MPER-TMD in lipid bilayers [67], the distances between W670 and F673 labeling sites on different protomers within the same trimer are 2.5-3.7 nm, and thus the inter-monomer F663 – W666 distance within the same trimer is expected to be at least 4 nm. These intra-trimer distances significantly exceed the measurable ^{19}F-^{19}F distance upper limit of ~2 nm [51]. Thus, we do not expect to detect intra-trimer distances from these fluorinated residues. This assumption will be tested by measuring the ^{19}F-^{19}F correlation spectra of MPER-TMD in different membranes. If the ^{19}F labels are not sufficiently separated

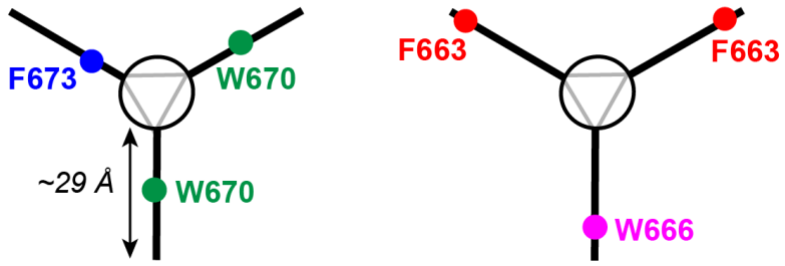

Figure III.1. Schematic diagram of the dimension of MPER-TMD trimers and positions of fluorinated residues in the two mixed-labeled peptide samples.
Each trimer, which has an MPER length of ~29 Å, is associated with a lipid area of ~29 nm^2 in each lipid leaflet at a P/L ratio of 1 : 30. If the trimers are uniformly distributed in the lipid membrane, then there is a sufficient number of lipid molecules to prevent interdigitation of two trimers.

within each trimer, then we expect to detect ^{19}F-^{19}F cross peaks for all membrane compositions instead of only some of the membranes.

The NMR structural model indicates that the overall MPER helix length is about 29 Å, measured from L661 Cα to W680 Cα (Fig. III.1) At the P/L ratio of ~1:30, each trimer is on average solvated by about 45 lipid molecules in each leaflet, which occupy an area of ~29 nm^2. We estimate that this should be sufficient to separate the trimers if they are homogeneously distributed in the membrane instead of inhomogeneously clustered. This hypothesis can again be tested by measuring 2D ^{19}F-^{19}F correlation spectra in different lipid membranes. If the peptide concentration at a P/L of 1:30 is too high and causes close approach of trimers in all membranes, then ^{19}F-^{19}F correlation signals will be detected for all membrane compositions instead of only some of the membranes.

Fig. III.2 a shows the 1D ^{19}F CP spectra of the two mixed labeled samples in the VMS^{cluster} membrane. The 4-CF_3-labeled Phe residues show isotropic chemical shifts of -62 ppm whereas the 5-^{19}F-labeled Trp residues show isotropic chemical shifts of about -125 ppm (Fig. III.2 a). The high sensitivity of the trifluoromethyl ^{19}F NMR signal facilitates the detection of long-range cross peaks [51]. 2D ^{13}C-^{13}C correlation spectra (Fig. III.2b, c) of L684, L679, and I675 in the MPER show α-helical chemical shifts, confirming the helical conformation of the peptides in these membranes.

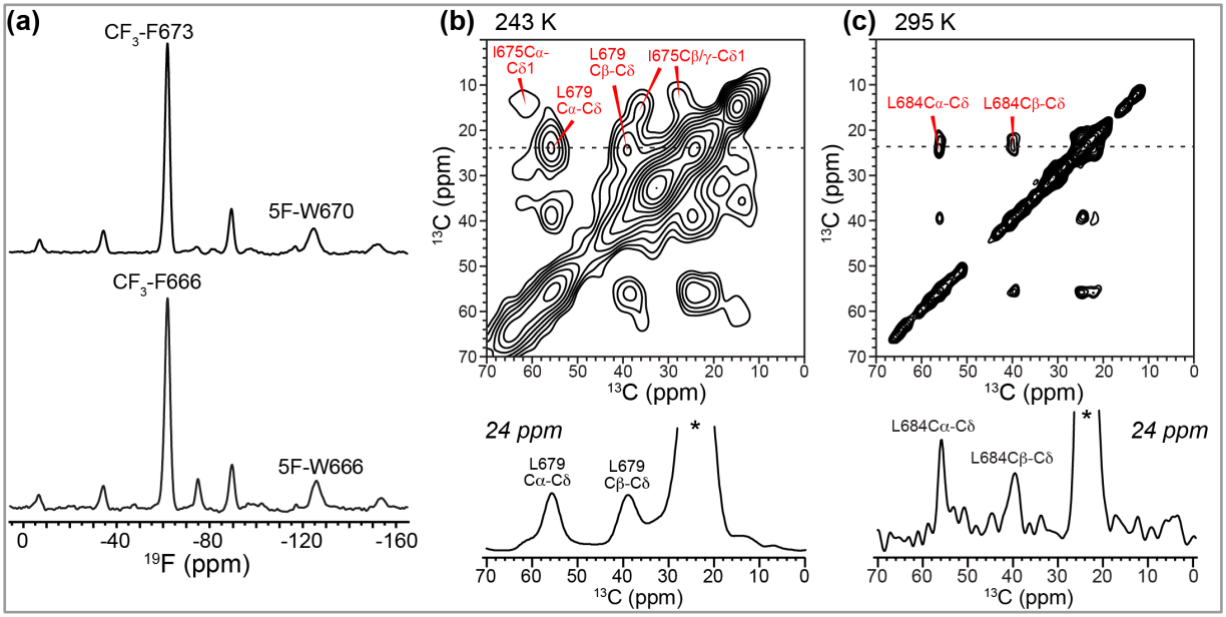

Figure III.2. Characterization of the MPER-TMD conformation in the VMS^{cluster} membrane by ^{19}F and ^{13}C NMR.
(**a**) 1D ^{19}F CP spectra of mixed CF_3-F673 and 5F-W670 labeled peptides (sample 1) and mixed CF_3-F663 and 5F-W666 labeled peptides (sample 5) in the VMS^{cluster} membrane. The spectra were measured at 243 K under 10.3 kHz MAS. (**b**) 2D ^{13}C-^{13}C correlation spectrum of I675 and L679 ^{13}C-labeled MPER-TMD in the VMS^{cluster} membrane (sample 5) at 243 K under 9 kHz MAS. The 24-ppm cross section is shown below, where the asterisk indicates the diagonal peak. (**c**) 2D ^{13}C-^{13}C correlation spectrum of L684 ^{13}C-labeled MPER-TMD in the VMS^{cluster} membrane (sample 1) at 295 K under 9 kHz MAS. The 24-ppm cross section is shown below.

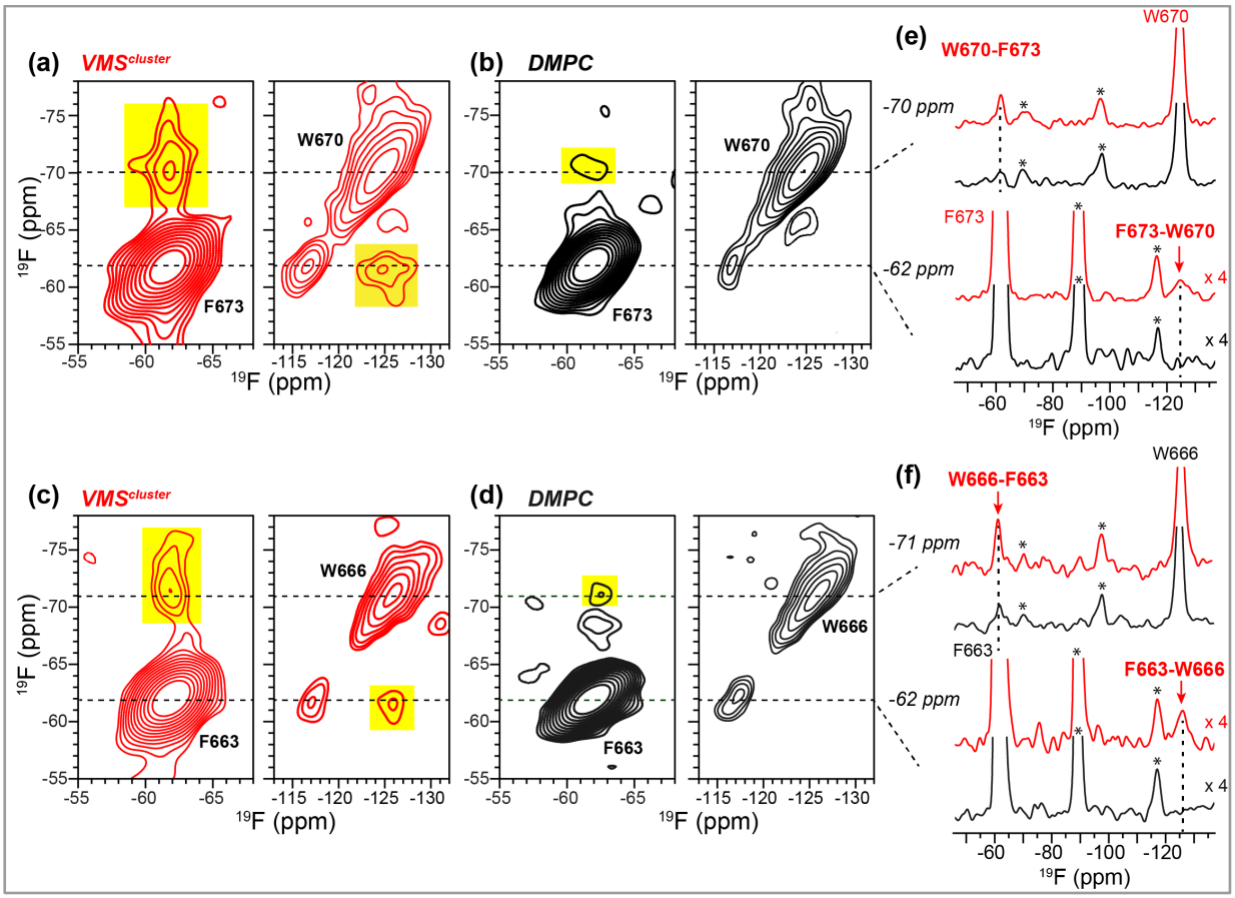

Figure III.3. 500 ms 2D ^{19}F-^{19}F correlation spectra of mixed fluorinated gp41 trimers.
(a) 2D spectrum of mixed 5F-W670 and CF_3-F673 labeled peptides in the VMS^{cluster} membrane at P/L = 1:30 (sample 1). **(b)** 2D spectrum of mixed 5F-W670 and CF_3-F673 labeled peptides in DMPC at P/L = 1:32 (sample 2). (**c**) 2D spectrum of mixed 5F-W666 and CF_3-F663 labeled peptides in the VMS^{cluster} membrane at P/L = 1:30 (sample 5). **(d)** 2D spectrum of 5F-W666 and CF_3-F663 mixed labeled peptide in DMPC at P/L = 1:32 (sample 6). Cross peaks are highlighted in yellow. **(e)** 1D ^{19}F cross sections of 5F-W670 and CF_3-F673 from the 2D spectra of the VMS^{cluster} sample and DMPC sample in (**a**) and (**b**). Asterisks indicate spinning sidebands. **(f)** 1D ^{19}F cross sections of W666 and F663 from the 2D spectra of the VMS^{cluster} sample and the DMPC sample in (**c**) and (**d**). All 2D spectra were measured at 243 K where protein motions were frozen.

Fig. III.3 shows the 500 ms 2D ^{19}F-^{19}F spin diffusion spectra of fluorinated MPER-TMD in VMS^{cluster} and DMPC membranes. These 2D spectra were measured with rotor synchronization for the indirect dimension to increase the spectral sensitivity. The 5F-Trp chemical shifts appear at folded positions of -70 ppm in the indirect dimension of these 2D spectra. We observed clear correlation signals between W670 and F673 in the VMS^{cluster} membrane, but the cross peaks are absent in the DMPC membrane (Fig. III.3 a, b). This contrast shows that intra-trimer distances are indeed too long to be measured, and moreover the MPER-TMD trimers approach each other in the cholesterol-containing VMS^{cluster} membrane. Similarly, correlation peaks between W666 and F663 are clearly observed in the VMS^{cluster} membrane but are much weaker in the DMPC membrane (Fig. III.3 c, d). These results indicate that multiple MPER-

TMD trimers cluster in the cholesterol-containing VMS^{cluster} membrane but not in the DMPC bilayer. We also measured 2D correlation spectra of POPE-bound peptide and observed no intermolecular cross peaks between W670 and F673 (Fig. S3). As a positive control, 2D spectra of the peptide in the VMS^{cluster} membrane at a higher P/L ratio of 1:10 showed clear cross peaks between W670 and F673, as expected (Fig. S3).

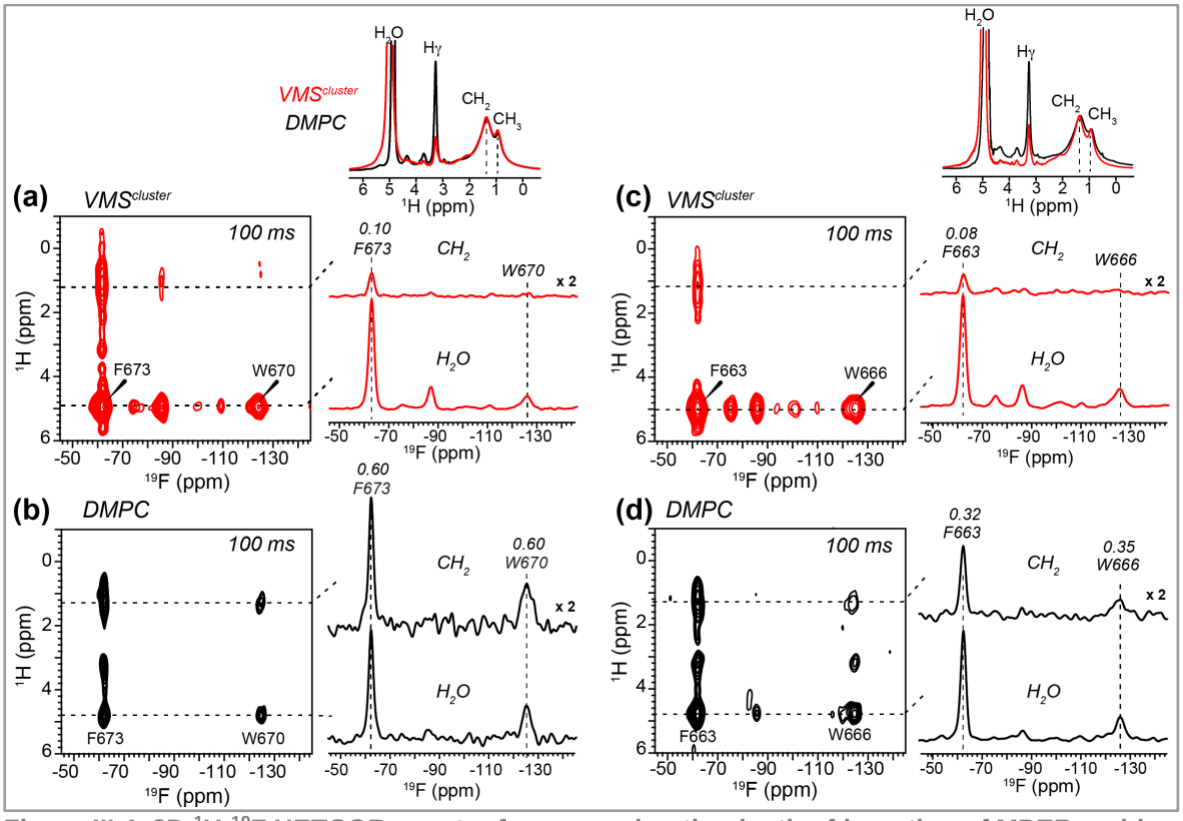

Figure III.4. 2D ^{1}H-^{19}F HETCOR spectra for measuring the depth of insertion of MPER residues in different lipid membranes.
(**a**) 2D spectrum of mixed 5F-W670 and CF_3-F673 labeled peptide in the VMS^{cluster} membrane at P/L = 1:30. (**b**) 2D spectrum of mixed 5F-W670 and CF_3-F673 labeled peptide in the DMPC membrane at P/L = 1:32. (**c**) 2D spectrum of mixed 5F-W666 and CF_3-F663 labeled peptide in the VMS^{cluster} membrane. (**d**) 2D spectrum of mixed 5F-W666 and CF_3-F663 labeled peptide in the DMPC bilayer. 1D ^{19}F cross sections at the lipid CH_2 and water ^{1}H chemical shifts are shown on the right of each 2D spectrum. The two DMPC samples show much higher lipid cross peaks compared to the VMS^{cluster} samples. The VMS^{cluster} 2D spectra (**a, c**) were measured at 275 K whereas the DMPC 2D spectra (**b, d**) were measured at 290 K. 1D ^{1}H spectra of the two types of membranes at these temperatures show similar ^{1}H linewidths for the lipid chain CH_2 peak, indicating that the lipid chain dynamics is similar at these temperatures.

For the VMS^{cluster}-membrane bound sample, the cross-peak intensities are not symmetric: the magnetization transfer from 5F-Trp to CF_3-Phe (-70 ppm row) is higher than the reverse transfer from CF_3-Phe to 5F-Trp (-62 ppm row). We attribute these asymmetric cross peak intensities to the reduction of long-range ^{19}F-^{19}F dipolar coupling by the rotating CF_3 group, as previously shown for model compounds [51]. The close approach of W670 and F673 between two trimers, as well as the close approach of W666 and F663, suggest that two trimers interdigitate in the VMS^{cluster} membrane (Fig.

III.5 a, b), so that an MPER helix of one trimer packs in antiparallel with an MPER helix of a second trimer.

III.3.b. The MPER resides on the membrane surface in cholesterol-containing membranes

Since different MPER structural models have been proposed in micelles, bicelles and bilayers [67, 143-145], the MPER conformation is likely sensitive to the membrane environment. This suggests that clustering of the MPER-TMD trimers might perturb the MPER conformation, for example by squeezing the helix out of the membrane-water interface, whereas well separated and isolated trimers might allow the MPER to insert more deeply into the membrane. To test this hypothesis, we measured the depth of insertion of the MPER using 2D ^{1}H-^{19}F correlation experiments with ^{1}H spin diffusion [146, 147]. Specifically, we measured the lipid-peptide and water-peptide ^{1}H-^{19}F cross peak intensities to probe the depth of insertion of the fluorinated residues.

Fig. III.4 shows 2D ^{1}H-^{19}F correlation spectra of the MPER-TMD peptides in VMS^{cluster} and DMPC membranes with 100 ms ^{1}H spin diffusion. The spectra were measured at 290 K for the DMPC samples and 275 K for the VMS^{cluster} samples to reach similar lipid chain dynamics and ^{1}H spin diffusion coefficients. This is verified by 1D ^{1}H MAS spectra of the two types of membrane samples, which show similar linewidths for the lipid CH_2, CH_3 and $H\gamma$ signals. At 290 K, fully hydrated pure DMPC membrane exists in the rippled ($P_{\beta'}$) phase [148]; however, the peptide likely broadens the L_α-to-$P_{\beta'}$ phase transition. In both membranes, the CF_3-Phe and 5F-Trp signals show correlation peaks with the water and lipid CH_2 proton signals at 4.8 ppm and 1.2 ppm, respectively. Therefore, the MPER helix partitions to the membrane-water interface, in good agreement with the previous ^{13}C NMR spectra [67]. However, the relative intensities of the lipid and water cross peaks differ dramatically between the two membrane environments. The lipid-peptide cross peak intensities are 32-60% of the water-peptide cross-peak intensities in the DMPC membrane, but decrease to only 7-10% of the water-peptide cross peak intensities in the VMS^{cluster} membrane. This indicates that the MPER is much more deeply inserted into the DMPC bilayer than the VMS^{cluster} membrane. Moreover, in the DMPC membrane, the lipid cross peak intensities are high for C-terminal residues of the MPER but low for N-terminal residues, with an intensity trend of F673 > W670 > W666 > F663. This trend indicates that the MPER helix is tilted from the membrane plane, with the N-terminus more exposed to the aqueous solution while the C-terminus more immersed in the membrane (Fig. III.5 c, d). In contrast, in the VMS^{cluster} membrane, the four fluorinated residues show similarly weak lipid cross peak intensities, indicating that the MPER helix is parallel to the plane of the VMS^{cluster} membrane and is shallowly immersed.

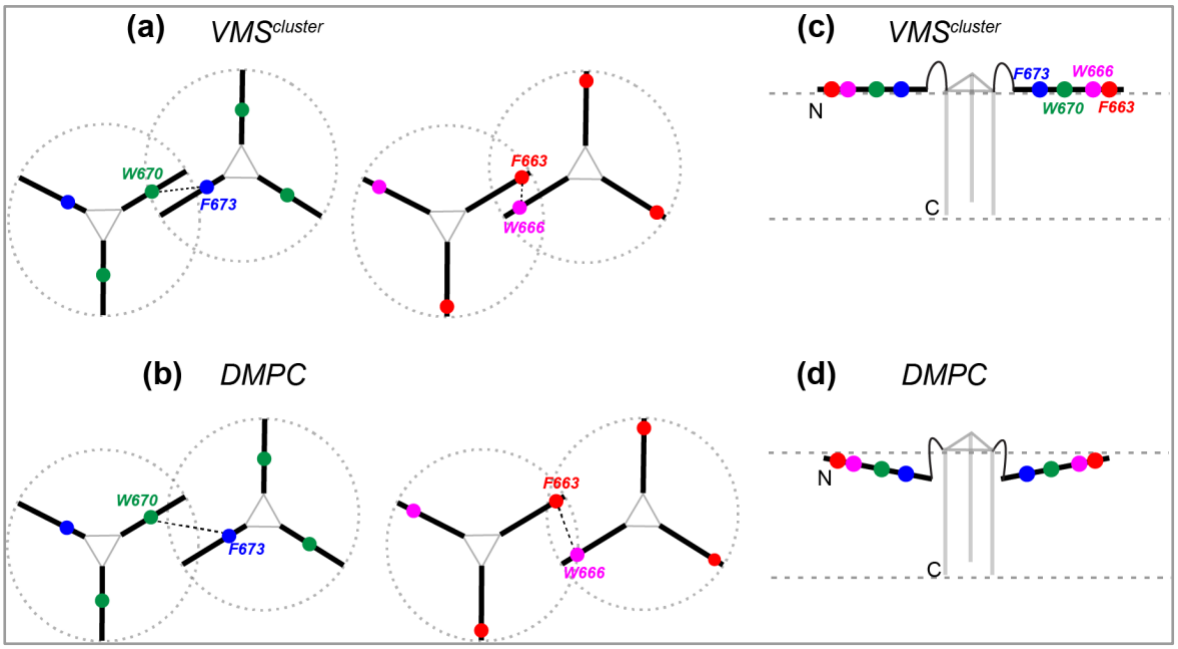

Figure III.5. Models of gp41 MPER-TMD trimer clustering
(a, b) and MPER depth of insertion (**c, d**) in lipid membranes. (**a, c**) VMS^{cluster} membrane. (**b, d**) DMPC membrane. Two gp41 trimers cluster to cause partial interdigitation of the MPER. The trimers approach each other more closely in the VMS^{cluster} membrane than in the DMPC membrane. The MPER helices are more deeply inserted in the DMPC bilayer than in the VMS^{cluster} membrane.

III.3.c. Molecular dynamics capture trimer association and MPER orientation in cholesterol-containing membranes

To quantify the effect of the membrane composition on the orientation and depth of insertion of the MPER, we conducted all-atom molecular dynamics simulations, and evaluated the average Z positions of each amino acid residue of the peptide relative to the bilayer center. **Fig. III.6** shows the results of the simulations for a single gp41 trimer. At 303 K, the center of MPER lies at 19 and 12 Å from the bilayer center in the VMS^{cluster} and DMPC membranes, respectively (**Fig. III.6 a, c**). The VMS^{cluster} membrane is only 5.1 Å thicker than the DMPC bilayer: the distance from the membrane center to the average phosphorus position in each leaflet is 22.8 Å for the VMS^{cluster} membrane and 17.7 Å for DMPC at 303 K. Thus, these results indicate that the MPER is less embedded in the VMS^{cluster} membrane than in the DMPC bilayer, consistent with the solid-state NMR data. In addition, the MPER orientation is more parallel to the membrane surface in the VMS^{cluster} membrane: the average angle θ between the helix axis and the bilayer normal is 70˚ in the VMS^{cluster} membrane but decreases to 45˚ in the DMPC membrane (**Fig. III.6 d-f**). This orientational change is consistent with the depth difference of the peptide between the two membranes.

To test whether these differences in MPER orientation and depth of insertion are due to cholesterol, we carried out simulations in a modified, cholesterol-free, VMS^{cluster} membrane. As shown in **Figs. III.6 b** and **III.6 d**, excluding cholesterol from the membrane led to a pronounced decrease of the average Z positions of MPER residues as well as a reduction of the θ angle compared to the results in the cholesterol-

containing VMS^{cluster} membrane. As illustrated by the snapshots in **Fig. III.6 e**, binding of cholesterol to the helix-turn-helix region of the peptide tends to orient the MPER parallel to the membrane surface, and reduces its insertion into the hydrophobic region of the bilayer. These trends are qualitatively maintained in the 280 K simulations (Fig. S4, Fig. S5), although the orientational difference is smaller in the low-temperature simulations, in part because the DMPC membrane is in the gel phase at 280 K (Fig. S6). These simulations thus support the physiological relevance of the solid-state NMR measurements at low temperatures.

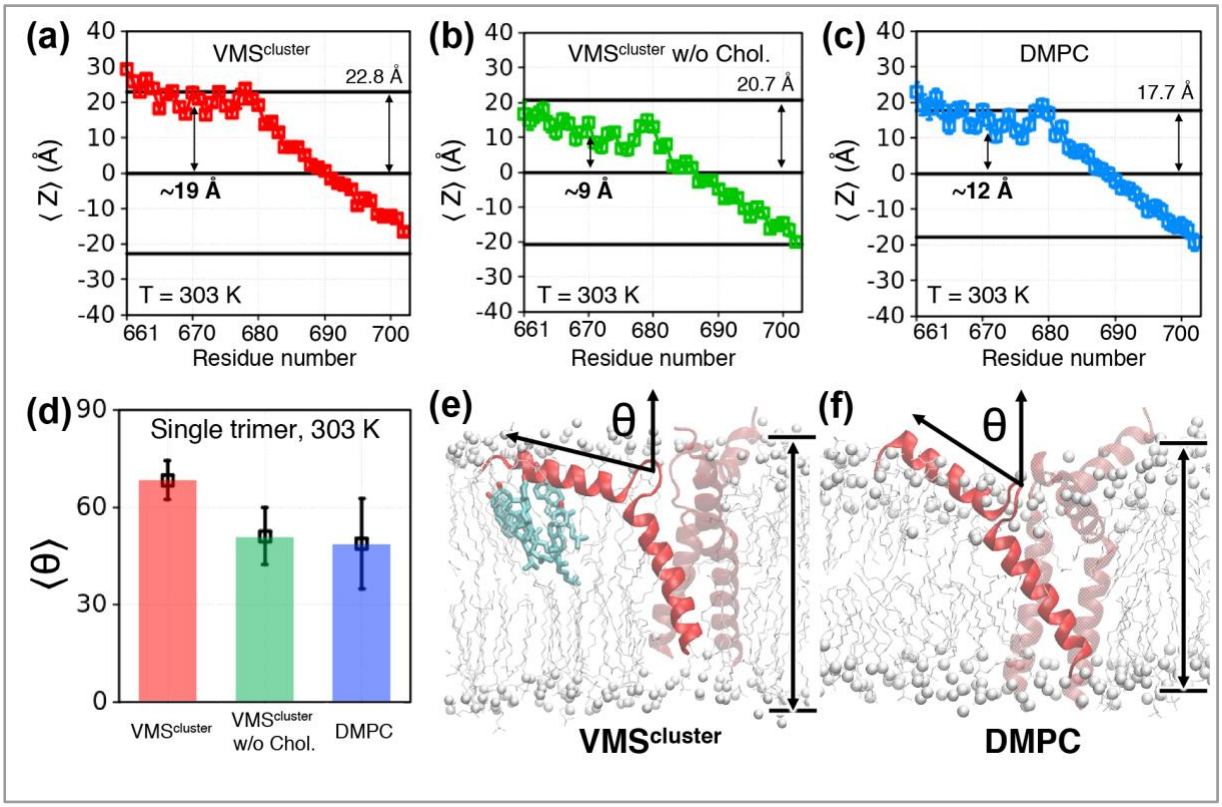

Figure III.6. All-atom simulations at 303 K of a single gp41 MPER-TMD trimer indicate that the MPER orientation is perturbed by cholesterol.
Simulations at 280 K give qualitatively similar results and are summarized in Fig. S4. (**a-c**) Z coordinates of all atoms in each residue, averaged over three peptide chains along independent MD trajectories. A single gp41 trimer is embedded in the (**a**) VMS^{cluster} membrane, (**b**) cholesterol-free VMS^{cluster} membrane, and (**c**) DMPC membrane. Statistical errors of the Z coordinates are similar in magnitude as the size of each box symbol. The membrane center is taken to be Z = 0, and the membrane thickness, defined by the location of P atoms in the two leaflets, is indicated by horizontal solid lines. (**d**) Average angle θ between the MPER helix and the membrane normal, which is defined as the Z axis of the simulation box. The Cα atoms of the first and last 4 residues (L661-D664 and A677-W680) of MPER are used to define the helical axis. (**e, f**) Snapshots from VMS^{cluster} and DMPC simulations illustrate the different locations of the MPER and the locations of nearby (within 2.5 Å of MPER) cholesterol molecules in the VMS^{cluster} membrane. Phosphate atoms are shown as white spheres and lipid tails are shown as thin lines.

All-atom molecular dynamics simulations reveal that multiple MPER-TMD trimers indeed cluster in the membrane; moreover, this self-association is facilitated by cholesterol. To characterize the separation between two trimers, we monitored two quantities: the distribution of pairwise distances between all Cα atoms in adjacent

MPERs, and the distribution of distances between W680 Cα distances in adjacent MPERs (Fig. III.7 a). The latter is particularly robust against MPER lateral fluctuations, since W680 is near the turn between the MPER and the TMD. Both these distance parameters are more stable than the inter-trimer W670-F673 and W666-F663 distances measured in the 2D ^{19}F-^{19}F correlation NMR experiments, which are sensitive to fluctuations of the MPER helix at the sluggish membrane-water interface.

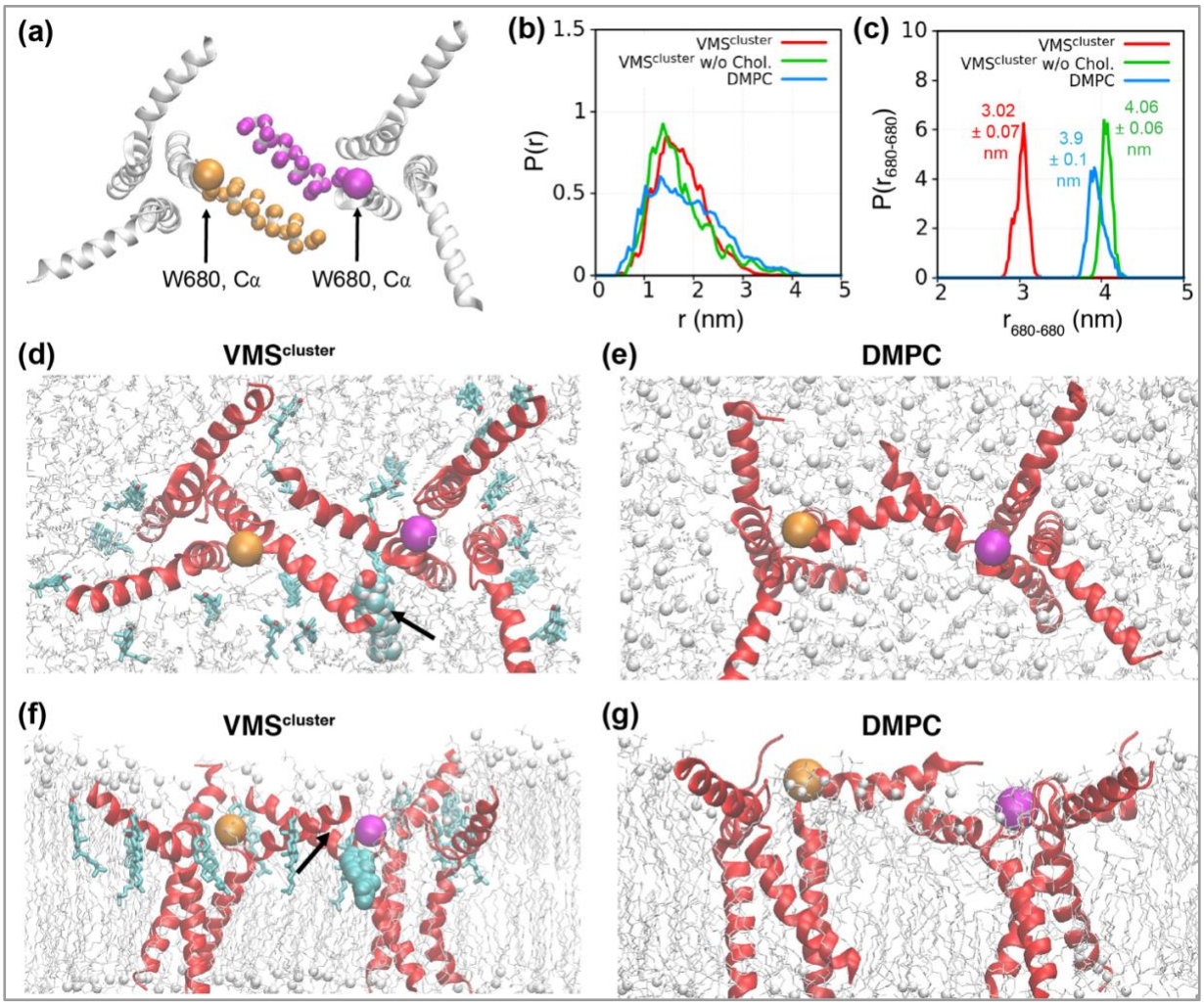

Figure III.7. Association of two MPER-TMD trimers in all-atom simulations at 303 K.
(**a**) Snapshot illustrating the displacement of two gp41 trimers from the simulations. Small spheres indicate the Cα atoms in adjacent MPERs whereas big spheres represent the Cα atoms of W680 near the C-terminal end of the MPER. (**b**) Probability distribution of pairwise distances between all Cα atoms in adjacent MPERs of two gp41 trimers, as shown in panel (a). (**c**) Probability distribution of W680-W680 Cα-Cα distances between two gp41 trimers, as shown in panel (a). The results at 280 K are qualitatively similar and are shown in Fig. S4. (**d, e**) Top view of snapshots for the dimer of trimers in the VMS^{cluster} and DMPC membranes, respectively. Cholesterols within 5 Å of any atoms of MPER are shown, and in some cases, cholesterol is observed to interact with both MPERs. (**f, g**) Sideview of the snapshots. These snapshots indicate that close MPER contacts form only through inter-trimer interactions, supporting the result of the solid-state NMR analysis (**Fig. III.5**).

Fig. III.7 b shows that the Cα-Cα distance distribution is broader in the DMPC membrane than in the VMS^{cluster} membrane, suggesting that two MPERs from two trimers are more tightly associated in the VMS^{cluster} membrane. The distance distributions between adjacent W680 Cα atoms (Fig. III.7 c) show an even clearer trend: the average separation is 3.0 nm in the VMS^{cluster} membrane, which increases to 3.9 nm in the DMPC membrane and 4.1 nm in the cholesterol-free VMS^{cluster} membrane. Therefore, the MPER-TMD trimers cluster more tightly in cholesterol-containing membranes than in cholesterol-free membranes. Moreover, when the clustered dimer of trimers in the VMS^{cluster} membrane is embedded in cholesterol-free membranes, the distance between the two trimers quickly increased in independent simulations (Fig. S7**)**. As the snapshot in Fig. III.7 d, f illustrates, cholesterol molecules occasionally interact simultaneously with the MPER motifs from two trimers. CG simulations (Fig. S2) confirm this favorable interaction between gp41 and cholesterol, showing an enhancement of the cholesterol concentration near gp41 compared to the bulk.

III.4. Discussion

These solid-state NMR data (Fig. III.3, III.4) and molecular dynamics simulations provide direct experimental evidence for the clustering of gp41 MPER-TMD trimers in lipid bilayers. The 2D ^{19}F-^{19}F spin diffusion NMR spectra, which are sensitive to inter-fluorine distances up to ~2 nm [51], give residue-specific information about trimer-trimer association on the nanometer scale. The observation of ^{19}F-^{19}F correlation peaks between W670 and F673 at the center of two different MPER helices, and between F663 and W666 near the N-terminus of two MPER helices, indicates that multiple trimers cluster to intercalate their MPER helices (Fig. III.5). Importantly, these ^{19}F-^{19}F correlation peaks are observed in the cholesterol-containing VMS^{cluster} membrane but are mostly suppressed in the DMPC membrane at the same P/L molar ratios (Fig. III.3). This difference indicates that these intermolecular cross peaks do not result from the same trimer nor reflect the average separation of homogeneously distributed trimers in the lipid membrane. Rather, they result from the close approach of multiple MPER-TMD trimers in the presence of cholesterol. This association involves inter-fluorine distances of less than 2 nm, which is shorter than the average separation at the P/L ratio of 1:30 used here.

The clustering of the MPER-TMD trimers in the cholesterol-containing membrane correlates with the more surface-exposed location of the MPER in the VMS^{cluster} membrane compared to the DMPC membrane. 2D ^{1}H-^{19}F HETCOR spectra show that the MPER residues have much weaker cross peaks with lipid acyl chains in the VMS^{cluster} membrane than in the DMPC membrane (Fig. III.4, Fig. III.5 c, d). Atomistic simulations confirm that the MPER helix is more parallel to the membrane surface in the VMS^{cluster} bilayer but is more tilted and buried in the DMPC bilayer (Fig. III.6). The more in-plane orientation extends the MPER reach, thus promoting trimer-trimer interactions. The fact that cholesterol lifts and extends the MPER to the membrane surface is in excellent agreement with the location of cholesterol under the canopy of the MPER helix, as found in the recent solid-state NMR and molecular dynamic study [125]. The simulations in that study identified two hotspots of interaction with cholesterol,

^{673}FNITN^{677} in the MPER and ^{684}LFIMI^{688} in the TMD. These two hotspots flank the turn between the MPER and TMD and sequester cholesterol in the L-shaped fold, in analogy with the mode of interaction between the influenza M2 protein and cholesterol [149, 150].

The limited sensitivity of ^{19}F exchange NMR experiments for measuring nanometer ^{19}F-^{19}F contacts prohibit a more exhaustive study of the lipid dependence and peptide-concentration dependence of gp41 trimer clustering. Instead, molecular dynamics simulations fill this gap. All-atom simulations show that the MPER-TMD trimers cluster at an even lower P/L molar ratio of 1:70 (**Fig. III.7 d**, **Table III.3**), supporting the notion that this trimer clustering is relevant under biological conditions. Removal of cholesterol from the VMS^{cluster} membrane increased the average inter-trimer W680-W680 distances to 4.1 nm, similar to the average distance of 3.9 nm in DMPC bilayers (**Fig. III.7 c**). In the VMS^{cluster} membrane, cholesterol molecules are observed to interact occasionally with adjacent MPERs of two trimers. Such bridging configurations may combine with cholesterol's indirect modulation of the orientation of the MPER helix to facilitate trimer clustering. A recent coarse-grained simulation of full-length gp41 in a virus-mimetic membrane showed that at least three gp41 trimers are required to cause membrane fusion [151]. Lipid stalk formation was observed when multiple trimers approached each other within ~3.5 nm, measured from the center of mass of each trimer. In our current all-atom simulations, the distance between the centers of the TM helical bundle is 3.8-4.3 nm, in good agreement with the results of the previous coarse-grained simulations.

Our current finding that membrane cholesterol promotes the clustering of MPER-TMD trimers is consistent with previous fluorescence spectroscopy data that cholesterol enhanced the fusion activity of the MPER and promoted its self-association [124]. It is also consistent with the model that gp41 localizes to the edge of the cholesterol-rich, liquid-ordered region of the membrane, as proposed here [125]. This model was validated by fluorescence microscopy on the gp41 N-terminal fusion peptide (FP) [20, 80]; in these studies, adding linactants to the membranes reduced the efficiency of gp41 FP-mediated membrane fusion events. The VMS^{cluster} membrane in our NMR experiments and simulations contains 30 mol% cholesterol and 20 mol% SM. Although the phase diagram of this exact lipid mixture has not been characterized, based on the ternary phase diagram of POPC/PSM/cholesterol [152], the VMS^{cluster} membrane likely contains both L_d and L_o phases [153-155]. Explicitly probing the preferential localization of gp41 to different lipid domains would require much larger systems that are computationally expensive at the atomistic level. As an alternative approach [156], our coarse-grained simulations found that the cholesterol concentrations near gp41 are substantially elevated compared to the bulk (Fig. S2), confirming that gp41 preferentially interacts with cholesterol. Combining these solid-state NMR data and simulations, we propose that complexation between the MPER and cholesterol induces lateral segregation of gp41 to cholesterol-rich regions of the lipid membrane and anchors the MPER at the membrane surface for self-association. In addition to cholesterol, the amino acid sequence of the MPER may also play a role in clustering. For example, a recent NMR study found that trimerization of the MPER peptide in solution requires

hydrophobic interactions involving two N-terminal Leu residues [157]. Our simulations indicate that I665, D664, S668, N671 and W672 are predominantly involved in trimer-trimer contacts (Fig. S8), suggesting that both hydrophobic and polar interactions contribute to MPER clustering. Therefore, gp41 clustering may be promoted by the concerted action of the cholesterol-rich membrane and the MPER amino acid sequence.

How does clustering of MPER-TMD trimers mediate membrane fusion? We propose that multiple gp41 trimers, brought together by the cholesterol dimers and tetramers discovered recently [158], amplify positive membrane curvature prior to the formation of the hemifusion intermediate. We speculate that this positive membrane curvature is caused by the shallow insertion of the MPER helix and the large radial footprint of each MPER-TMD trimer [159, 160]. This positive membrane curvature favors the close juxtaposition of the viral membrane and host-cell membrane. Interdigitation of the MPER helices between the clustered trimers may enable the coordinated bending of a larger lipid surface area compared to an end-to-end arrangement of the MPER helices. Clustering of MPER-TMD may also further enrich cholesterol, thus causing increased lipid asymmetry. Thus, clustering of gp41 MPER-TMD may promote virus-cell membranes fusion by generating both membrane curvature and lipid asymmetry.

Acknowledgments

This work is supported by NIH grant GM066976 to M.H. The computational work and Y.O. are supported in part by the NSF grant CHE-1829555 to Q.C. Computational resources from the Extreme Science and Engineering Discovery Environment (XSEDE), which is supported by NSF grant number OCI-1053575, are greatly appreciated. Part of the computational work was performed on the Shared Computing Cluster which is administered by Boston University's Research Computing Services (URL: www.bu.edu/tech/support/research/).

Conclusion: Assembling the puzzle

In this study, we learned that the HIV virion membrane-bound domains of the gp41 fusion protein indeed form clusters in lipid bilayers (**Section III.3.a**), as discussed in **Section I.2.c**. This clustering activity was stronger in membranes with the $VMS^{cluster}$ lipid composition, which as discussed above, likely contains the L_o/L_d domain boundaries that gp41 is known to utilize [20], opening the door for a possible functional connection between gp41's clustering and utilization of line tension at L_o/L_d boundaries (**Section I.2.b**). Curiously, the membrane-proximal external region (MPER) domain was largely surface-exposed in the $VMS^{cluster}$ membrane (**Section III.3.b**), and instead exhibited lipid-packing-disrupting membrane insertion activity (see **Section I.2.e**) in the DMPC membrane, suggesting gp41 may only insert its MPER domain into membranes at other stages of the virus life cycle. Finally, this study demonstrated a viable ^{19}F-^{19}F spin diffusion NMR method that could be applied to other questions of membrane protein clustering and supermolecular assembly.

IV. Clustering of Tetrameric Influenza M2 Proteins in Lipid Bilayers

By Madeleine Sutherland, Nhi Tran and Mei Hong; submitted to *Biochim. Biophys. Acta.*, October 30, 2021

IV. Graphical abstract

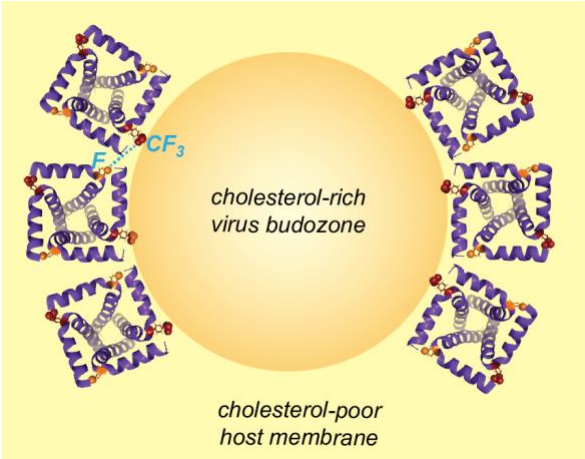

^{19}F spin diffusion NMR reveals that tetrameric influenza M2 proteins cluster around cholesterol- and phosphoethanolamine-rich membrane domains.

IV. Abstract

The tetrameric influenza M2 protein forms a drug-targeted proton channel to mediate virus uncoating and carries out membrane scission for virus release. While the proton channel function of M2 has been extensively studied, the mechanism by which M2 mediates membrane scission is still not well understood. Fluorescence and electron microscopy data indicate that M2 tetramers concentrate at the neck of the budding virus in the host plasma membrane. However, molecular structural evidence for this clustering is scarce. Here, we use ^{19}F solid-state NMR spectroscopy to investigate M2 clustering in phospholipid bilayers. By mixing CF_3-Phe47 labeled peptide with 4-F-Phe47 labeled peptide at equal concentrations and measuring F-CF_3 cross peaks in 2D ^{19}F-^{19}F correlation spectra, we show that M2 tetramers indeed cluster in lipid bilayers. This clustering is stronger in cholesterol-containing membranes and in phosphoethanolamine membranes. The observed F-CF_3 correlation peaks indicate that Phe47 sidechains of different tetramers are less than ~2 nm away from each other. ^{1}H-^{19}F correlation peaks between lipid chain protons and fluorinated Phe47 indicates that Phe47 is more deeply inserted into the membrane in the presence of cholesterol than in its absence, suggesting that Phe47 preferentially interacts with cholesterol. Static ^{31}P NMR spectra indicate that M2 induces negative Gaussian curvature in the POPE membrane. These results suggest that M2 tetramers cluster at cholesterol- and PE-rich region of the cell membrane to cause high membrane curvature, which in turn leads to membrane scission for virus release.

IV.1. Introduction

Influenza A and B infections represent an ongoing global health issue where improved vaccine and therapeutic design could make a substantial difference (see **Section I.1.**). Basic research on Influenza A's chemistry can open up new technological avenues. The 97-residue Matrix protein 2 (M2) of the Influenza A virus plays several important roles in the virus life cycle. After the influenza virus enters a cell by endocytosis, the acidic environment of the endosome activates M2's proton channel activity, acidifying the virion, which triggers fusion of the virus lipid envelope and the endosomal membrane and release of the viral ribonucleoproteins into the host cell [161-163]. M2's proton channel function has been extensively characterized [164-171], and the mechanism of its inhibition by adamantane drugs has also been studied using biophysical and biochemical experiments [172-177]. In addition to this proton channel function, M2 also mediates virus budding and release by carrying out membrane scission in a manner that is independent of the host machinery such as ESCRT [178-180]. M2-deletion viruses can form buds on the plasma membrane but cannot be released, demonstrating this scission function [178].

Several lines of evidence suggest that M2 and other eukaryotic membrane proteins may cluster to carry out their functions. Electron micrographs of immunogold labeled M2 on the ~100 nm scale show that the protein is clustered to the neck of the budding virions in influenza-infected MDCK cells [21, 178]. Fluorescence microscopy images of phase-separated giant unilamellar vesicles showed rhodamine-labeled M2 [178] and M2CD(22-62) [21] are restricted to the L_d phase but concentrate on the boundary of liquid-ordered (L_o) and liquid-disordered (L_d) phases. Functionally important cluster formation has also been reported in other related membrane proteins. For example, fluorescence microscopy data revealed Gag-restricted clustering of the HIV Env protein upon virus maturation [22]. Oxidation-sensitive co-clustering of the SNARE component syntaxin-1A and the pore-forming subunit of Ca^{2+} channel Cav1.2 was associated with the interactions between these proteins in exocytotic neurotransmitter release [23].

Despite these biophysical data that M2 proteins self-associate on the micron and ~100 nm scale, whether M2 tetramers cluster on the molecular length scale of a few nanometers has not been established experimentally. Coarse-grained molecular dynamics simulations found that M2 tetramers spontaneously assemble into compact clusters in membrane environments with high lateral stress or "stiff" lipid species. Simulated lateral stress on the order of what a plasma membrane experiences led to M2 clusters which coincided with spontaneous inward (-/- by our sign convention) curvature of the membrane [21]. A ^2H NMR study of the M2(22-46) peptide containing deuterated Ala_{29} in DOPC : DOPE (4:1) bilayers showed that increasing the peptide/lipid molar ratio increased the quadrupolar couplings. Simulations of these spectral lineshapes indicate that the uniaxial rotational diffusion rates of the tetramers slowed by 25-fold [181]. However, since motional rates could decrease due to the increased membrane viscosity when more peptide is present, this dynamics change does not provide unambiguous information about M2 clustering.

The recently discovered cholesterol binding to the M2 protein may provide a molecular mechanism for M2 clustering [182-185]. ^{13}C-^{19}F distance measurement between ^{13}C-labeled M2(22-61) and fluorinated cholesterol showed that the methyl-rich β-face of cholesterol interacts with the methyl-rich Ile and Leu residues in the M2 transmembrane (TM) helix, while the polar hydroxyl end of cholesterol interacts with polar and aromatic residues in the M2 amphipathic helix (AH) [184]. Two cholesterol molecules are bound to each M2 tetramer on average, forming an asymmetric M2-cholesterol complex. It was hypothesized that this asymmetric complex might facilitate the recruitment of M2 to the virus budozone because of the higher cholesterol concentration at the budozone compared to the plasma membrane. More recent ^{19}F and ^{13}C spin diffusion NMR data on lipid bilayers with 17% cholesterol revealed that cholesterol molecules exist as dimers and tetramers in lipid bilayers, with the smooth α-face preferentially interacting with each other, thus the rough β-face could point outward towards proteins [54]. The cholesterol dimer effect held in both phase-separated palmitoylsphingomyelin (PSM):POPC:chol and miscible POPC:POPG membranes [54]. Meanwhile, as previously mentioned, M2CD tends to localize along L_o/L_d phase boundaries. These results suggests that cholesterol dimers might act as the molecular "glue" to facilitate the clustering of multiple M2 tetramers.

To directly determine whether M2 tetramers cluster in lipid bilayers, and to characterize the membrane compositions and protein requirements for such clustering, here we employ ^{19}F magic-angle-spinning (MAS) NMR spectroscopy. We synthesized M2 peptides containing either 4-F-Phe47 or 4-CF_3-Phe47, and prepared equimolar mixtures of the two peptides in lipid membranes. We then measured 2D ^{19}F-^{19}F spin diffusion correlation spectra to determine if the differently labeled peptides come into close proximity. ^{19}F spin diffusion NMR is well suited for measuring interatomic distances of 1-2 nm [50, 51, 186-191]. The lack of ^{19}F background in naturally occurring biomolecules allows us to detect only the sparsely fluorinated residues. ^{19}F has large isotropic and anisotropic chemical shifts, thus making them sensitive to molecular conformation. Most importantly, the large gyromagnetic ratio (γ) of ^{19}F increases the dipolar coupling strengths compared to couplings between low-γ nuclei. For example, ^{19}F-^{19}F dipolar couplings are 14-fold stronger than ^{13}C-^{13}C dipolar couplings for the same distance. Moreover, spin diffusion between a CF_3 group and a CF group is highly efficient due to the simultaneous polarization transfer of three fluorines to or from a CF group and methyl rotational averaging of the ^{19}F CSA, which speeds up spin diffusion. This ^{19}F spin diffusion NMR approach has been shown recently to allow the detection of inter-fluorine distances to ~2 nm [51, 188, 192, 193]. Using this ^{19}F spin diffusion NMR approach, here we show that M2 tetramers do form clusters in lipid membranes, and this clustering is facilitated by cholesterol and phosphoethanolamine (PE) lipids. We also probe the depth of insertion of Phe47 at the junction of the TM and AH using ^{1}H-^{19}F 2D correlation experiments [194], and correlate these observations with M2 clustering.

IV.2. Materials and Methods

IV.2.a. Peptide synthesis and purification

All M2 peptides used in this study were synthesized using Fmoc solid-phase chemistry on a custom designed flow peptide synthesizer [195]. Two different peptide constructs were synthesized: one containing both the TM helix and the amphipathic helix (M2CD), spanning residues 22-61, while the other comprised the TM domain (M2TM) spanning residues 22-49. The M2CD sequence is H-^{22}SSDPLVVAA SIIGILHLIL WILDRLFFKS IYRRLKYGLK R^{61}-NH_2. The M2CD construct comprises the kinked transmembrane helix (TM) and the Amphipathic Helix (AH) region of the cytoplasmic domain; the construct assembles into a tetramer with the amphipathic helix segments lying semi-embedded along the membrane surface [196]. EPR studies in this same POPC:POPG (4:1) regime showed the AH domain's membrane insertion and dynamics were only gently perturbed in the "M2TMC" (23-60) truncate compared to the full-length protein [197]. The M2TM sequence is H-^{22}SSDPLVVAA SIIGILHLIL WILDRLFFK^{49}-NH_2. This construct is three residues (^{47}FFK^{49}) longer than the commonly studied M2 TM peptide spanning residues 22-46. Each M2 peptide contained either a 4-CF_3-Phe47 label or a 4-F-Phe47 label. In addition to the ^{19}F labels, M2CD also contained ^{13}C, ^{15}N-labeled G34 and I51 and CD_3-labeled A29 while M2TM also contained ^{13}C, ^{15}N-labeled V27, A30 and G34 (**Table IV.1**). These ^{13}C, ^{15}N labeled residues allow us to monitor the secondary structure of these peptides in the membrane.

Table IV.1: Isotopic labeling and membrane compositions of the influenza AM2 samples used in this study.
4-CF3 or 4-F-labeled Phe47 residues are underlined and shown in red. 13C, 15N-labeled residues are bolded and shown in blue. CD3-labeled Ala is italicized.

M2CD(22-61)

```
22  25    30    35    40    45    50    55    60
SSD PLVVA ASIIG ILHLI LWILD RLFFK SIYRR LKYGL KR
```

Membrane Samples	P : L : C molar ratio	Lipid composition
1	1 : 12 : 3 : 3	POPC : POPG : chol
2	1 : 12 : 3	POPC : POPG
3	1 : 24 : 6 : 6	POPC : POPG : chol
4	1 : 24 : 6	POPC : POPG
5	1 : 30	POPE

M2TM(22-49)

```
22  25    30    35    40    45
SSD PLVVA ASIIG ILHLI LWILD RLFFK
```

Membrane Samples	P : L : C molar ratio	Lipid composition
6	1 : 24 : 6 : 6	POPC : POPG : chol
7	1 : 24 : 6	POPC : POPG

Each peptide was synthesized on the 0.05 mmol scale using H-Rink amide ChemMatrix resin (0.1 g at 0.05 mmol/g loading size). The resin was swelled in the reaction vessel for 5 min in ~5 mL of N,N-dimethylformamide (DMF) at 70°C. A 10-fold excess (0.5 mmol) of unlabeled amino acid was singly coupled with a coupling time of 50 s. After the final coupling step, the peptide was deprotected and cleaved from the resin by addition of TFA/phenol/H_2O/TIPS solution (88 : 5 : 5 : 2 by volume) in a fritted syringe under vortex agitation at room temperature for 3 hours. The resin was filtered off, and the crude peptide was precipitated and triturated three times with cold diethylether. The remaining solvent was allowed to evaporate from the crude peptide in the fume hood overnight.

To purify M2CD, we dissolved crude peptide in 30% acetonitrile and purified it by reverse-phase HPLC using a Vydac C4 column in the presence of 0.1% TFA. A linear gradient of 30-70% acetonitrile over 44 min was applied at a flow rate of 15 mL/min. The peptide eluted at 64% acetonitrile. The collected HPLC fractions were dried under nitrogen gas and lyophilized overnight to obtain pure powder. MALDI mass spectrometry data verified the mass of CF_3-Phe47 labeled M2CD to be 4766.8 Da, in good agreement with the calculated mass of 4764.8 Da. For the 4F-Phe47 labeled M2CD, the measured mass was 4715.2 Da, in good agreement with the calculated mass of 4713.8 Da.

4F-Phe47 labeled M2TM was purified by HPLC using a linear gradient of 30-100% acetonitrile in water over 65 min at a flow rate of 10 mL/min. MALDI-MS analysis verified the mass to be 3180.1 Da, in excellent agreement with the calculated mass of 3179.9 Da. The peptide eluted at 81% acetonitrile. HPLC fractions were dried under nitrogen gas and lyophilized overnight to obtain pure powder. The total synthesis and purification yield was about 5%. For CF_3-Phe47 labeled M2TM, crude peptide was dissolved in 60% acetonitrile, and reverse-phase HPLC used a linear gradient of 80-99% acetonitrile in water over 54 min at a flow rate of 10 mL/min. MALDI-MS analysis verified the mass to be 3228.3 Da, in good agreement with the calculated mass of 3229.9 Da. The peptide eluted at 83% acetonitrile. The total yield was 10%.

IV.2.b. Preparation of proteoliposomes

We used three phospholipids in this study: 1-palmitoyl-2-oleoyl-sn-glycero-3-phosphocholine (POPC), 1-palmitoyl-2-oleoyl-sn-glycero-3-phospho-(1'-rac-glycerol) (POPG), and 1-palmitoyl-2-oleoyl-sn-glycero-3-phosphoethanolamine (POPE). These POPX (X=C, G, E) lipids were chosen over saturated lipids to better mimic the acyl chain compositions of biological membranes. These lipids were mixed with cholesterol (chol) to produce three membrane mixtures: POPC : POPG (4:1), POPC : POPG : chol (4:1:1, i.e. 17 mol% cholesterol), and POPE. NMR samples contained 4.5-8.0 mg of peptide and 12-48 mg of lipids and cholesterol. The peptide/lipid molar ratios (P/L) refer to the ratio of M2 monomers to all phospholipids, excluding cholesterol. P/L values of 1:15 and 1:30 were used in this study. The 1:30 samples are more dilute compared to the recent ^2H NMR study, which used P/L ratios of 1:20 and 1:7.5 [181] .

For each membrane sample, we dissolved the appropriate mass of peptide in 500 µL TFE, while phospholipids and cholesterol were dissolved in 200-500 µL chloroform. About 20-50 µl of methanol was added to POPE to aid dissolution. The homogeneous lipid solution was added to the peptide-TFE solution, incubated at room temperature for at least 10 min, then the organic solvent was removed using nitrogen gas. The dried peptide-lipid film was resuspended in 2 mL buffer (10 mM pH 7.4 HEPES/NaOH buffer, 1 mM EDTA, and 0.1 mM NaN_3) and homogenized by one of two methods. The POPC : POPG membranes with or without cholesterol were homogenized by 10-15 cycles of freeze-thawing between liquid nitrogen and a 50˚C water bath. The POPE vesicle solution, which does not homogenize well by freeze-thawing, was sonicated at room temperature using a bath sonicator for at least three rounds of seven minutes each until the solution appeared homogeneous. These proteoliposome solutions were transferred to Thermo Scientific Snakeskin™ dialysis tubing with a 3.5 kD MWCO and dialyzed for 8-12 hours in sample buffer to remove residual TFE. The proteoliposome solutions were then ultracentrifuged to obtain the membrane pellets. Some samples were spun down using a Beckman Coulter Optima LE-80K centrifuge equipped with a SW-60 swinging bucket rotor at 40,000–45,000 rpm (143,000-272,000 x g) at 4˚C for 4–5 hours. Other samples were spun down at 55,000 rpm (max 186,000 x g) in a Beckman Coulter Optima Max preparative ultracentrifuge equipped with a TLA-55 rotor for two hours. The wet membrane pellets were allowed to dry to 40–50 wt% water in a desiccator or under nitrogen gas. When the volume of excess water was large, brief lyophilization was used. The samples were then spun into a 4 mm MAS rotor using a 5 mL pipette tip in a Thermo Sorvall ST 16R centrifuge.

IV.2.c. Solid-state NMR experiments

All MAS NMR experiments were conducted on a Bruker 400 MHz (^{1}H Larmor frequency) wide-bore AVANCE III-HD spectrometer using a 4 mm HFX MAS probe tuned to ^{1}H, ^{19}F and ^{13}C Larmor frequencies. Typical radiofrequency (RF) field strengths were 50-62.5 kHz for ^{19}F, 50-71 kHz for ^{1}H, and 50 kHz for ^{13}C. 1D ^{13}C and 2D ^{13}C-^{13}C correlation experiments used a ^{1}H excitation field strength of 71.4 kHz and a ^{13}C RF field strength of 50 kHz. Static ^{31}P NMR spectra were measured using a 4 mm ^{1}H/^{31}P probe at 298 K and 310 K. The ^{31}P RF field strength was 62.5 kHz, and 1024 scans were measured per spectrum.

The 2D ^{19}F-^{19}F correlation spectra were measured using a CORD [198] spin diffusion mixing time of 500 ms at a temperature of ~243 K to reduce peptide motion. Cross peak intensities between 4-CF_3-Phe47 and 4F-Phe47 report the distance between the two fluorine labels. The pulse sequence begins with ^{1}H-^{19}F cross polarization (CP), followed by ^{19}F chemical shift evolution under ^{1}H TPPM decoupling [199] and the CORD mixing period before detection. The unsynchronized 2D ^{19}F-^{19}F correlation spectra were measured under 8.5 kHz MAS. The indirect dimension spectral width was 211 ppm, and the maximum t_1 evolution time was 0.567 ms. For each sample, four to eight blocks of 2D spectra were coadded to obtain sufficient signal-to-noise ratios (SNRs), giving a total measuring time of 70 – 123 hours for each sample (**Table IV.2**).

To increase the spectral sensitivity, we also measured rotor synchronized 2D ^{19}F spectra that remove the spinning sidebands in the indirect dimension. For these experiments, the indirect dimension's spectral width was set to 23 ppm, and the corresponding MAS frequency was 8641 Hz. The t_1 increment was one rotor period, or 115.73 µs, and 28 complex t_1 time points were collected to reach a maximum evolution time of 1.62 ms. With the small spectral width for the indirect dimension, the 4-F-Phe47 peak was folded to -71 ppm. Four to eight blocks of 2D spectra were coadded for each sample to obtain sufficient SNRs, giving a total measuring time of 88 – 105 hours per sample (**Table IV.2**).

Table IV.2: Parameters for the 2D 19F-19F and 1H-19F NMR experiments.

Experiment	NMR Parameters	Experimental Time (hrs)	Membrane Sample
rotor synchronized 2D FF CORD	B_0 = 9.4 T, T_{set}=243-245 K, ν_r = 8641 Hz, SWH1 = 8641 Hz (=23 ppm), SWH2 = 93.75 kHz, ^{19}F carrier frequency = -68 ppm, NS per block =1024, τ_{rd}=1.7 s, $t_{1,max}$= 1.62 ms, $t_{1,inc}$= 115.8 µs, τ_{dwell}=5.3 µs, τ_{acq} = 4.3 ms, τ_{HF}=1 ms, τ_{CORD} = 500 ms, $\nu_{1H,acq}$ = 71.4 kHz (samples 3,4, and 6) and 62.5 kHz (samples 5 and 7).	105	3
		105	4
		105	5
		87.5	6
		87.5	7
2D FF CORD without rotor synchronization	B_0 = 9.4 T, T_{set}= 243 K, ν_r = 8500 Hz, SWH1 = 79.4 kHz, SWH2 = 93.75 kHz, ^{19}F carrier frequency = -90.2 ppm, NS per block = 256, τ_{rd} = 2 s, $t_{1,max}$ = 0.567 ms, $t_{1,inc}$= 12.60 µs, τ_{dwell} = 5.3 µs, τ_{acq} = 4.27 ms, τ_{HF}= 1 ms, τ_{CORD} = 500 ms, $\nu_{1H,acq}$ = 71.4 kHz.	122.5	1
		105	2
		140	3
		70	4
2D ^1H-^{19}F HETCOR with 100 ms ^1H spin diffusion	B_0 = 9.4 T, T_{set} = 262-265 K for samples 3, 4, 6, 7 and 283 K for sample 5, SWH1 = 5 kHz, SWH2 = 93.75 kHz, ^{19}F carrier frequency = -97.6 ppm, NS per block = 1024, τ_{rd} = 1.5 s, $t_{1,max}$= 4.8 ms, $t_{1,inc}$= 200 µs, τ_{dwell}=5.3 µs, τ_{acq} = 4.3 ms, τ_{HF}= 1 ms, T_2-filter duration = 117.6 µs, τ_{mix} = 100 ms, $\nu_{1H,acq}$= 71.4 kHz for sample 3 and 50 kHz for samples 4-7.	88	3
		88	4
		88	5
		88	6
		88	7

Symbols: B_0 = magnetic field; T_{set} = thermocouple-reported bearing gas temperature; ν_r = MAS frequency; SWH1: spectral width of the ω_1 dimension of the 2D spectra; SWH2: spectral width of the ω_2 dimension of the 2D spectra; ns = number of scans per t_1 slice of the 2D spectra; τ_{rd} = recycle delay; $t_{1,max}$ = maximum t_1 evolution time; $t_{1,inc}$ = increment or dwell time for the t_1 evolution period; τ_{dwell} = dwell time during direct acquisition of the FID; τ_{acq} = maximum acquisition time during direct detection; τ_{HF} = ^1H-^{19}F CP contact time; τ_{CORD} = CORD mixing time. $\nu_{1H,acq}$ = ^1H decoupling field strength during detection.

To probe the depth of insertion of Phe47 in the lipid membrane, we measured 2D ^{1}H-^{19}F heteronuclear correlation (HETCOR) spectra with ^{1}H spin diffusion [194]. The experiment began with four ^{19}F 90˚ pulses spaced by 2 ms each to saturate the ^{19}F magnetization. Then a ^{1}H 90˚ excitation pulse and a ^{1}H T_2 filter of 2*112.6 µs = 225.2 µs were used to select the water and lipid ^{1}H magnetization. The ensuing ^{1}H chemical shift evolution was followed by a ^{1}H mixing time of 100 ms during which the water and lipid ^{1}H magnetization was transferred to the peptide and was detected on ^{19}F after ^{1}H-^{19}F CP. These 2D HETCOR experiments used 48 t_1 time points to reach a maximum ^{1}H t_1 evolution time of 4.8 ms, and 1,024 scans per t_1 slice. Typical spectra were coadded from four blocks of experiments, giving signal-averaging times of 88 hours per sample. For different lipid membranes, we chose sample temperatures of 263– 283 K to obtain similar lipid CH_2 linewidth of ~350 Hz, as assessed in 1D ^{1}H spectra. This ensures that the lipid chain dynamics are similar between the different membranes, thus giving similar ^{1}H spin diffusion coefficients. ^{1}H chemical shifts were calibrated using the phosphocholine headgroup $H\gamma$ chemical shift of 3.26 ppm and the lipid chain ω chemical shift of 0.9 ppm for POPE. All NMR spectra were plotted from TopSpin 3.6.1. Peak intensities were analyzed in Microsoft Excel v16.52.

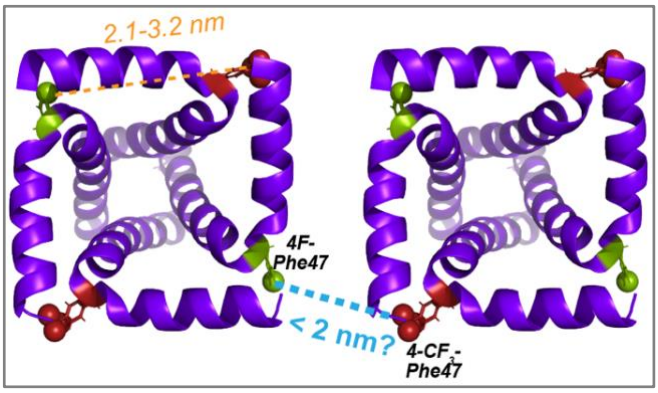

Figure IV.1. Schematic diagram of M2 clustering in lipid membranes.
The solid-state NMR orientational structure of M2(22-62) (PDB: 2L0J) solved in DOPC : DOPE bilayers is shown. Intra-tetramer nearest-neighbor distances between Phe47 sidechain *para*-hydrogens are 2.1 – 3.2 nm. The ^{19}F NMR experiments in this study probe clustering of the tetramers to within 2 nm between Phe47 residues of neighboring tetramers.

IV.3. Results

In this work, we investigate M2 clustering in lipid membranes as a function of the protein/lipid ratio, the presence or absence of cholesterol, and PC-rich membranes versus a PE membrane. We also compare M2 peptides that contain both the TM domain and the amphipathic helix (M2CD) versus only the TM domain (M2TM). The POPC : POPG (4:1) membrane composition and the peptide length were chosen to allow comparison of our data with previous biochemical studies of M2's membrane scission function [178, 200-202] and with NMR [183, 184] and EPR [197, 203, 204] studies of M2 peptides' interaction with membranes.

Our strategy for detecting tetramer association is to mix 4-CF_3-Phe47 labeled peptide with 4-F-Phe47 labeled peptide at a 1:1 molar ratio and measure CF_3-F cross peaks in 2D ^{19}F-^{19}F correlation spectra with a long spin diffusion mixing time of 500 ms. Phe47 is chosen because it lies at the corners of each M2CD tetramer, with maximal separation within each tetramer and potentially the shortest distance between two tetramers (**Fig. IV.1**). Based on the eight lowest energy structures of M2CD(22-62) in

DOPC : DOPG bilayers (PDB: 2L0J) [196], the intra-tetramer distances between the *para* hydrogens of Phe47 sidechain range from ~21 Å to ~33 Å. The average inter-monomer distance of ~27 Å is too long to be detected by ^{19}F spin diffusion NMR. We can estimate the distances between tetramers if they are uniformly distributed in the membrane. Molecular dynamics simulations of gel-phase POPC membranes indicate a headgroup area of 59 Å^2 [205]. Using this value, we estimate that the center-to-center distance between two M2 tetramers is about 66 Å at a P/L ratio of 1:30 and about 50 Å at a P/L of 1:15. Since each tetramer has a side length of approximately 27 Å, these values correspond to nearest-neighbor distances of ~39 Å and ~23 Å between fluorinated Phe47 residues in two parallel packed tetramers. These inter-tetramer separations for homogeneously distributed M2 tetramers are beyond the distance-detection limit of ^{19}F spin diffusion NMR experiments. However, if the M2 tetramers cluster in the membrane, then CF_3-F cross peaks can become observable. We test this hypothesis by measuring 2D ^{19}F-^{19}F correlation spectra as a function of P/L and membrane compositions.

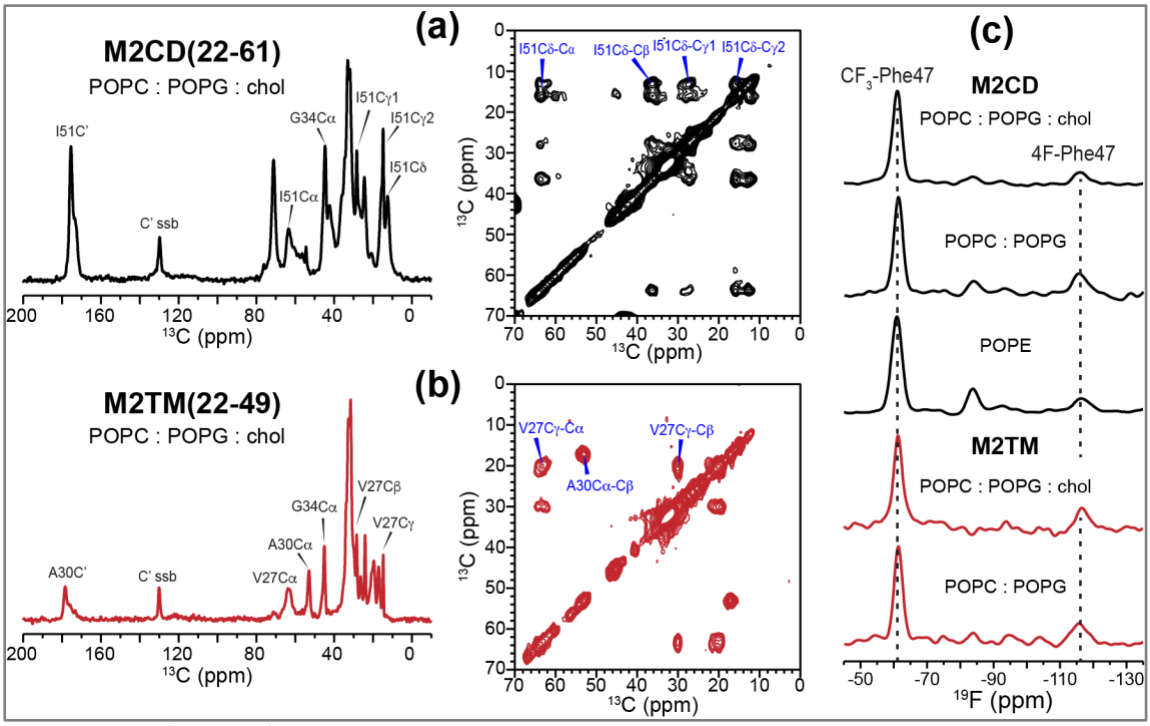

Figure IV.2. ^{13}C and ^{19}F NMR spectra of membrane-bound M2 peptides.
(**a**) 1D ^{13}C CP and 2D ^{13}C-^{13}C correlation spectra of M2CD at P/L 1:15 in POPC : POPG : chol membranes. The spectra were measured at 243 K under 10 kHz MAS. Peaks that are not annotated in the 1D spectra are natural abundance lipid ^{13}C signals. (**b**) Spectra of M2TM at P/L 1:30 in POPC : POPG : chol membranes. The spectra were measured at 253 K under 9 kHz MAS. These ^{13}C chemical shifts confirm the α-helical conformation of both peptides. (**c**) 1D ^{19}F CP spectra of membrane-bound M2CD and M2TM. The spectra show similar ^{19}F linewidths and intensity distributions, indicating that the peptides exhibit similar conformational dynamics under these experimental conditions. The spectra were measured between 243 and 253 K under 9 kHz and 10 kHz MAS.

IV.3.a. M2 tetramers cluster in a membrane-dependent manner

We first measured the ^{13}C chemical shifts of site-specifically labeled M2CD and M2TM peptides to verify that fluorination of Phe47 does not perturb the α-helical conformation of the peptide (Fig. IV.2). The ^{13}C chemical shifts of G34 and I51 in M2CD and V27, A30 and G34 in M2TM indeed correspond to the α-helical conformation in both POPC : POPG membranes and the POPE membrane, confirming that the helical conformation of the TM and AH domains is preserved [175, 206].

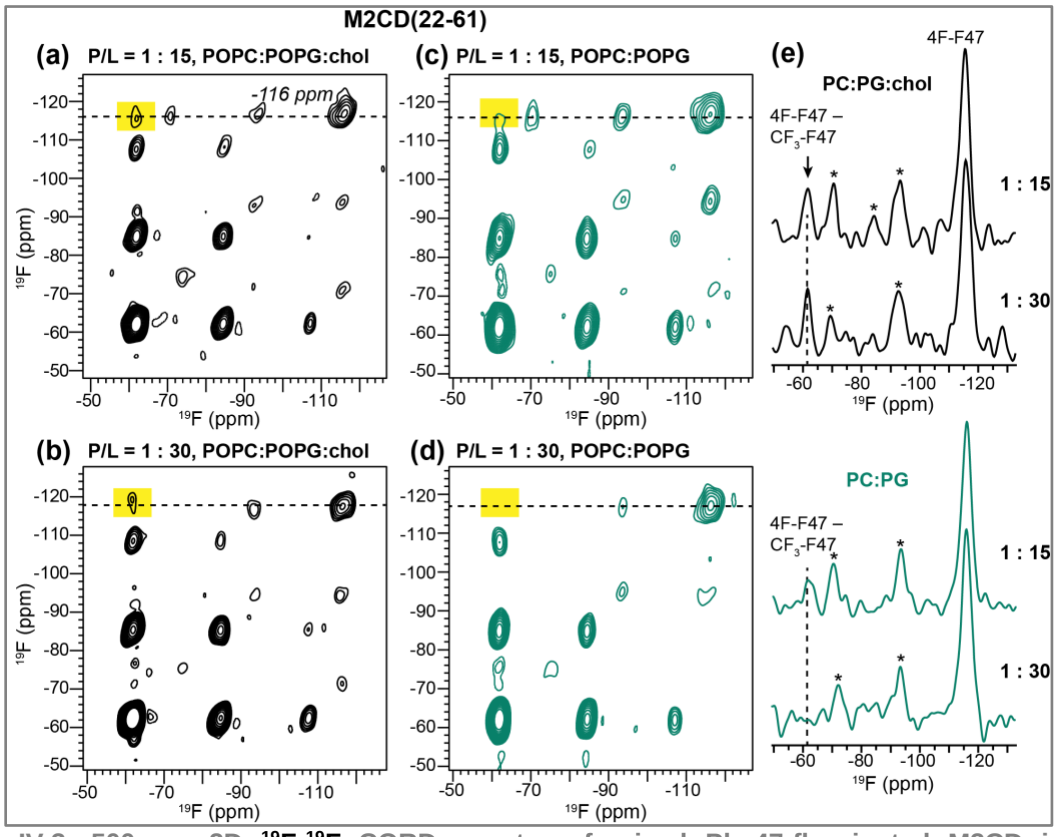

Figure IV.3. 500 ms 2D ^{19}F-^{19}F CORD spectra of mixed Phe47-fluorinated M2CD in lipid membranes.

The spectra were measured at 243 K under 8.5 kHz MAS. The -116 ppm cross section of 4F-Phe47 are extracted on the right. Cross peak between 4F-Phe47 and 4-CF_3-Phe47 (-62 ppm) indicates inter-tetramer contact. Spinning sidebands are denoted with asterisks in the cross sections. (a) 2D spectra of M2CD in POPC : POPG : chol membranes (left) and POPC : POPG membranes (right) at P/L 1:15. (b) 2D spectra of M2CD in POPC : POPG : chol membranes (left) and POPC : POPG membranes (right) at P/L 1:30. F-CF3 cross peaks are observed at high P/L in both membranes, but only in the cholesterol-containing membrane at the lower peptide concentration of 1:30.

Fig. IV.3 shows the 500 ms 2D ^{19}F-^{19}F CORD spectra of M2CD in POPC : POPG membranes with and without cholesterol. At a high P/L of 1:15, we observed a clear F-CF_3 cross peak in the POPC : POPG : chol membrane but a weaker cross peak in the POPC : POPG membrane (Fig. IV.3 a, c). When the peptide concentration was decreased two-fold to P/L 1:30 (Fig. IV.3 b, d), the F-CF_3 cross peak persisted in the POPC : POPG : chol membrane, moreover the intensity is similar to that of the high-concentration sample (Fig. IV.3 e), strongly suggesting that M2 tetramers cluster rather

than distributing homogeneously in the cholesterol-containing membrane. In contrast, peptide dilution in the POPC : POPG membrane completely suppressed the F-CF_3 cross peak, indicating that the intra-tetramer Phe47-Phe47 distances are too long to be measurable. If the 2D experiment were primarily detecting intra-tetramer cross peaks, it would be difficult to explain the dependence of these cross peak intensities on the membrane composition and peptide concentration. Therefore, these results together indicate that M2 tetramers cluster in the cholesterol-containing membrane, and this clustering is not an artifact of the high peptide concentration but reflects specific protein-protein interactions and protein-cholesterol interactions.

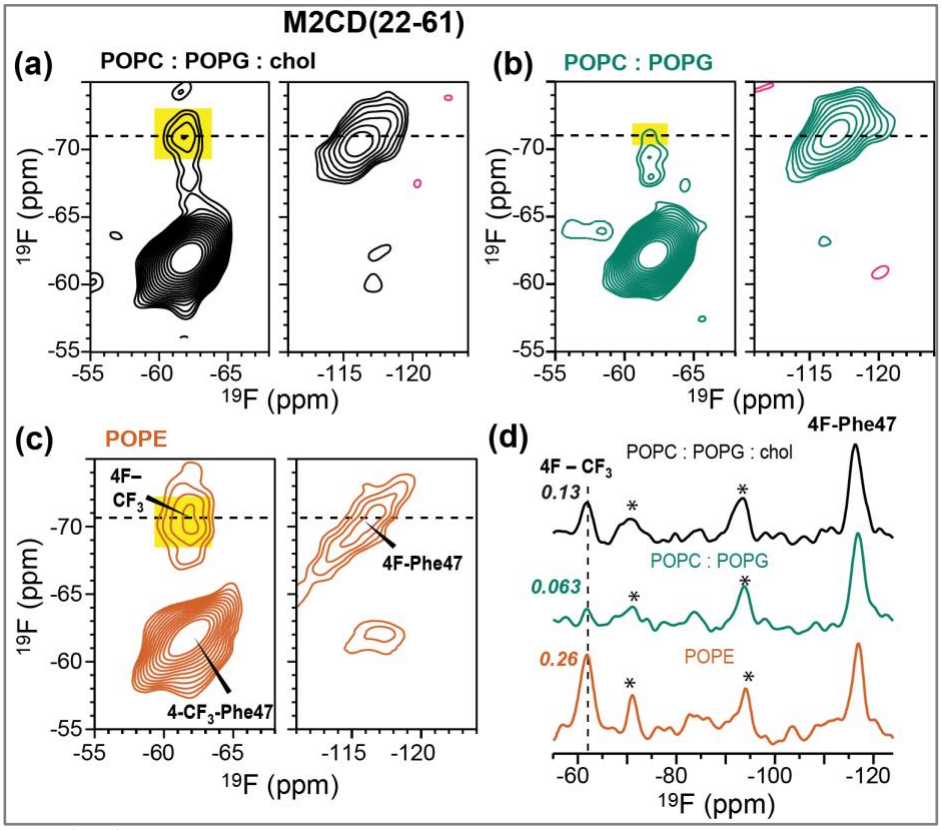

Figure IV.4. 2D ^{19}F-^{19}F correlation spectra of mixed Phe47 fluorinated M2CD peptides in three membranes at P/L 1:30.
The spectra were measured with 500 ms CORD mixing at 243 K under 8641 Hz MAS. (**a**) 2D spectrum of the peptide in the POPC : POPG : chol membrane. (**b**) 2D spectrum of the peptide in the POPC : POPG membrane. (**c**) 2D spectrum of the peptide in the POPE membrane. (**d**) 1D cross sections at the folded 4F-Phe47 chemical shift of -71 ppm. The CF_3 cross peak (dashed line) intensity relative to the sum of all peak intensities in the cross section decreases in the order of POPE > POPC : POPG : chol > POPC : POPG.

To reproduce the F-CF_3 cross peaks with higher sensitivity, we measured rotor-synchronized 2D ^{19}F correlation spectra of the 1:30 M2CD samples and quantified the intensity of the F-CF_3 cross peak relative to the total intensities of the -71 ppm cross section of the folded 4F-Phe47 peak (Fig. IV.4). The cross-peak intensities varied significantly between different membrane samples. In the POPC : POPG : chol membrane, the F-CF_3 cross peak intensity is 0.13 of the total intensity (Fig. IV.4 a),

whereas in the POPC : POPG membrane, the cross peak intensity decreased to 0.063 (Fig. IV.4 b), confirming that cholesterol facilitates clustering. To investigate whether M2 can also cluster in other membranes, we measured the 2D ^{19}F-^{19}F correlation spectrum of M2CD in the POPE membrane. PE lipids are enriched in Influenza virus lipid envelopes relative to the host cell membranes from which they are derived [207, 208], and their negative curvature is known to play an important role in membrane fusion and fission in general [9, 74]. Fig. IV.4 c shows the 2D ^{19}F CORD spectrum of POPE-bound M2CD. A strong CF_3-F cross peak is observed, whose intensity is even higher than that of the POPC : POPG : chol sample, indicating that M2CD clusters more tightly in the POPE membrane.

To determine whether the amphipathic helix is required for M2 clustering, we also measured the 2D ^{19}F spin diffusion spectra of M2TM(22-49) in POPC : POPG membranes with and without cholesterol. At the P/L of 1:30, we observed a clear F-CF_3 cross peak in the POPC : POPG : chol membrane but a much weaker cross peak in the POPC : POPG membrane (Fig. IV.5). This trend is similar to M2CD, indicating that M2 remains able to cluster in the absence of the AH residues 50-62, and this clustering is also facilitated by cholesterol. The F-CF_3 cross peak intensities of M2TM are stronger than that of M2CD (Fig. IV.5 c), suggesting that M2TM peptides may form tighter clusters than M2CD.

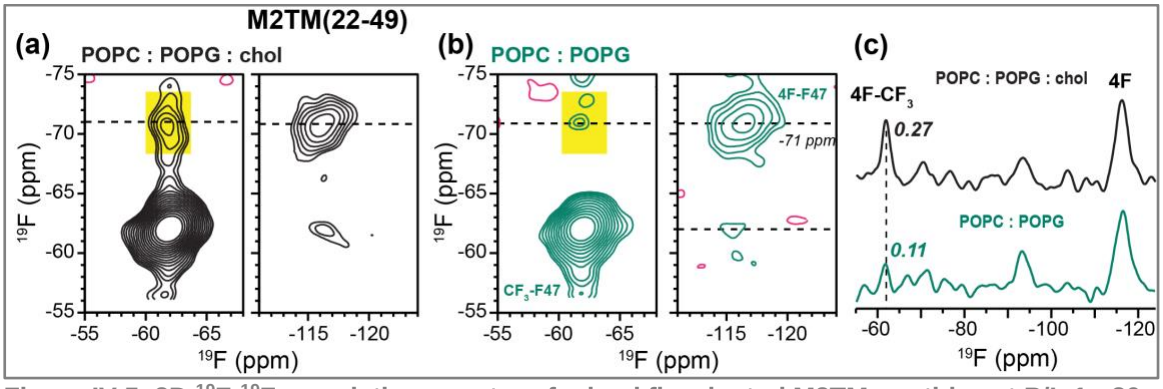

Figure IV.5. 2D ^{19}F-^{19}F correlation spectra of mixed fluorinated M2TM peptides at P/L 1 : 30. The spectra were measured with a CORD mixing time of 500 ms at 243 K under 8641 Hz MAS. (a) 2D spectrum of the peptide in the POPC : POPG : chol membrane. (b) 2D spectrum of the peptide in the POPC : POPG : membrane. (c) 1D cross section of the two 2D spectra at the folded 4F-Phe47 chemical shift of -71 ppm. The F-CF_3 cross peak (dashed line) intensity is much higher in the cholesterol-containing membrane than in the cholesterol-free membrane.

IV.3.b. Depth of insertion of Phe47 in lipid membranes

Using fluorinated Phe47 as a readout, we next investigated the depth of insertion of this junction between the TM and AH domains using 2D ^{1}H-^{19}F correlation experiments [194]. By detecting the cross peaks of the Phe47 CF_3 signal at -62 ppm with the water and lipid protons at ~5.1 and 1.3 ppm, respectively, we obtain information about the depth of insertion of the TM-AH junction in different lipid membranes. The 4F-Phe47 signal at -116 ppm reports the same information, but due to its low intensity we do not analyze this signal below. Fig. IV.6 compares the 2D ^{1}H-^{19}F HETCOR spectra measured with a ^{1}H spin diffusion mixing time of 100 ms. All samples exhibit strong

water-Phe47 cross peaks, as expected because of the surface-proximal position of this residue [196]. The depth of Phe47 is manifested in terms of the lipid-CF_3 cross peak intensity relative to the water-CF_3 cross peak, I_{CH2}/I_{H2O}. For M2CD, this lipid-to-water intensity ratios are similar, 0.16 and 0.14, in the POPC : POPG : chol membrane and POPC : POPG membrane, respectively (Fig. IV.6 a, b). This indicates that the Phe47 sidechain is moderately inserted into both membranes.

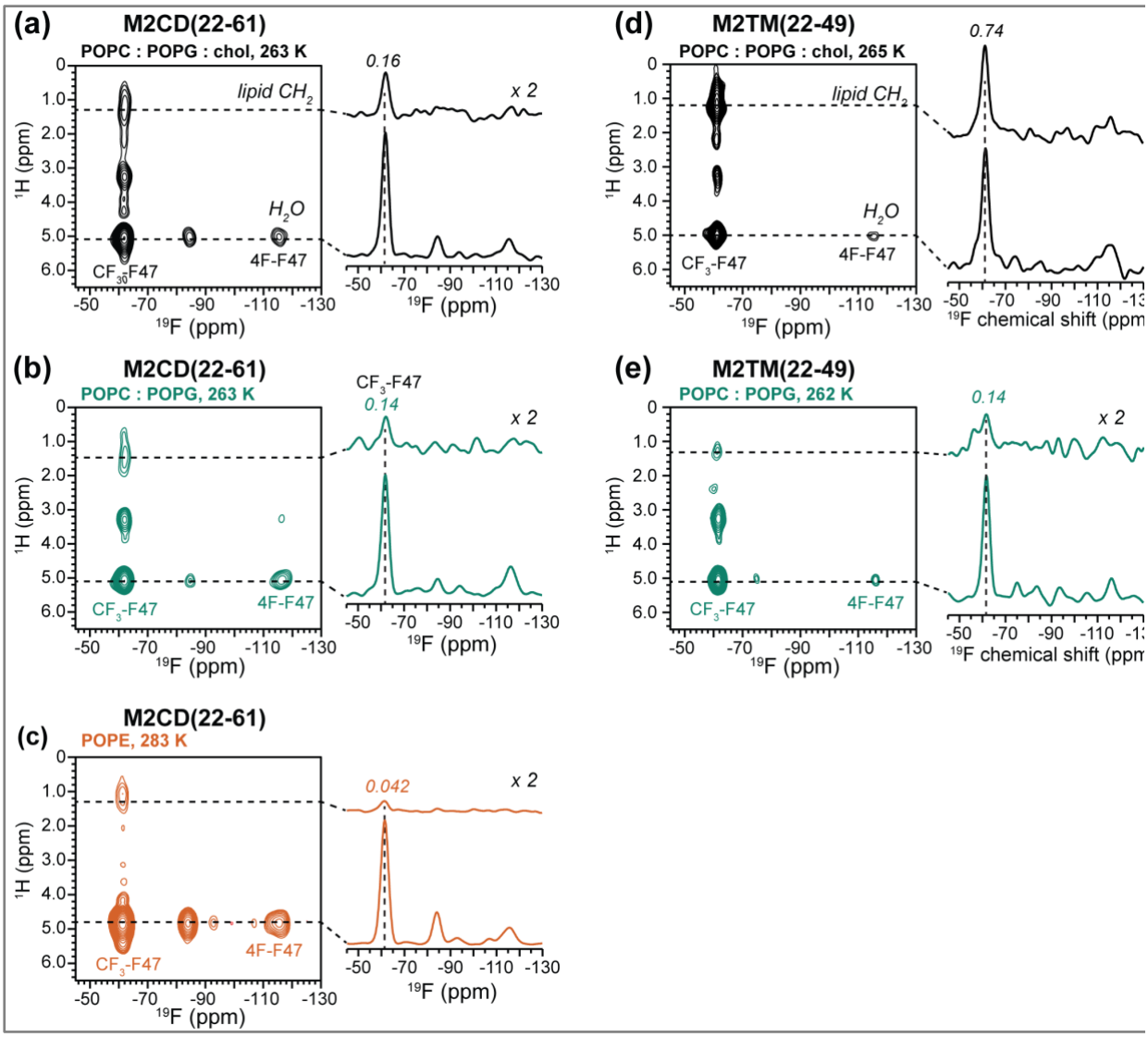

Figure IV.6. 2D ^1H-^{19}F correlation spectra of M2 peptides in different lipid membranes.
The spectra were measured at sample temperatures that give similar lipid chain ^1H linewidths. All samples have a P/L ratio of 1:30. **(a, b, e)** M2CD spectra. **(c, d)** M2TM spectra. (**a**) Spectrum of M2CD in POPC : POPG : chol membranes, measured at 263 K. (**b**) Spectrum of M2CD in POPC : POPG membranes, measured at 263 K. (**c**) Spectrum of M2TM in POPC : POPG : chol membranes, measured at 265 K. (**d**) Spectrum of M2TM in POPC : POPG membranes, measured at 262 K. (**e**) Spectrum of M2CD in POPE membrane, measured at 283 K. Water and lipid CH_2 cross sections are shown to the right of each 2D spectrum. The intensity ratio of the lipid–CF_3 cross peak relative to the water-CF_3 cross peak is the highest for M2TM in the POPC : POPG : chol membrane and the lowest for M2CD in the POPE membrane.

Interestingly, for the M2TM peptide, the Phe47 sidechain shows an unexpectedly high lipid cross peak intensity of 0.74 in the POPC : POPG : chol membrane (Fig. IV.6 c), indicating close contact with the lipid chains. Removal of cholesterol from the membrane decreased the lipid-CF_3 cross peak intensity to 0.14, similar to the values found for M2CD (Fig. IV.6 d). These spectra were measured at temperatures at which the lipid chains have similar ^{1}H linewidths. Thus, the high intensity of the Phe47-lipid cross peak in the POPC : POPC : chol membrane cannot be attributed to different ^{1}H spin diffusion coefficients, but must be attributed to deeper insertion of the Phe47 sidechain into the membrane.

Finally, we measured the 2D HETCOR spectrum of POPE-bound M2CD. In contrast to the POPC : POPG samples, negligible lipid cross peak intensity is observed (Fig. IV.6 e), indicating that Phe47 is much more shallowly inserted into the POPE membrane than the POPC : POPG membranes.

IV.3.c. M2CD induces curvature to POPE membranes

Membrane scission requires the separating membranes to adopt strong local negative Gaussian curvature (NGC), wherein every point on the surface of the membrane has principal curvatures of opposite signs. This NGC is manifested as a broad isotropic peak in the static ^{31}P NMR spectra [209] and as diffraction peaks at characteristic Q positions in small-angle X-ray scattering (SAXS) data. A previous SAXS study showed that M2CD and full-length M2 promote cubic phases, which possess NGC's, in PE-rich membranes [74]. We previously measured ^{31}P NMR spectra of oriented DMPC/DHPC (3:1) bicelles and found that M2CD but not M2TM induced an isotropic peak, indicating the formation of a high-curvature phase [210]. To investigate if the clustering of M2 tetramers correlates with membrane curvature formation, we measured the static ^{31}P spectra of the three membranes containing M2CD at a P/L of 1:30 (Fig. IV.7). Neither of the two POPC : POPG membranes showed an isotropic peak, indicating that these two membranes maintain their lamellar morphologies. In comparison, the POPE membrane exhibits a small isotropic peak at 310 K, indicating the generation of NGC at this temperature. Thus, the membrane that gives rise to the highest intermolecular F-CF_3 cross peak and shallowest AH insertion also has the highest curvature.

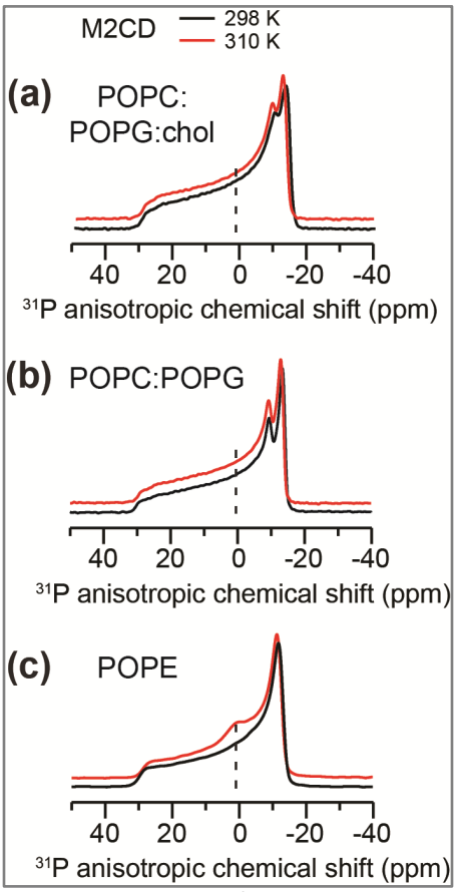

Figure IV.7. Static ^{31}P NMR spectra of proteoliposomes containing M2CD at P/L 1:30.
The spectra were measured at 298 K (black lines) and 310 K (red lines). (**a**) POPC : POPG : chol membranes. (**b**) POPC : POPG membranes. (**c**) POPE membranes. Only the POPE membrane exhibits an isotropic peak, which is indicative of NGC.

IV.4. Discussion

The ^{19}F NMR data shown here, taken together, indicate that M2 tetramers cluster on the molecular length scale in lipid membranes, and this clustering is promoted by cholesterol and PE lipids. By varying the peptide/lipid molar ratio, membrane lipid composition, and the peptide length, we can attribute the observed F-CF_3 cross peaks predominantly to tetramer clustering, whereas Phe47-Phe47 contact within each tetramer has negligible contribution. At the low temperature (~243 K) of the ^{19}F spin diffusion experiments, the peptide motion is frozen and the lipid dynamics is also significantly suppressed, thus differential rates of molecular motion cannot explain the different F-CF_3 cross peak intensities observed in different membranes. Under these conditions, we found that the F-CF_3 cross peaks are not present in all samples. In the cholesterol-free POPC : POPG membrane at P/L ratios of 1:30 and 1:15, the F-CF_3 cross peak of M2CD is either completely absent or weak. This indicates that the Phe47-Phe47 distances within each tetramer is longer than measurable by ^{19}F spin diffusion, consistent with the average nearest-neighbor distance of ~2.7 nm between Phe47 residues in each tetramer [196]. As another control, we measured 2D ^{19}F-^{19}F correlation spectra of the M2TM peptide. The removal of most of the AH segment from this peptide rules out the possibility that the amphipathic helix might interact with cholesterol in such a way to affect the tetramer conformation and shorten the intra-tetramer Phe47-Phe47 distances [204]. At the same time, the presence of ^{47}FFK^{49}, which resides at the TM-AH junction, should retain the ability of the peptide to bind cholesterol [183, 184]. Indeed, the presence of the F-CF_3 cross peak in M2TM(22-49) bound to the POPC : POPG : chol membrane supports the conclusion that M2 tetramers form tight clusters in cholesterol-containing membranes. We also observed a strong F-CF_3 cross peak in the POPE membrane, in the absence of cholesterol, which provides additional evidence of the ability of the M2 peptides to cluster on the 1-2 nm scale.

These ^{19}F NMR data are consistent with, and more direct than, ^{2}H NMR spectra of the Ala_{29} CD_3 group for demonstrating clustering [181]. In that study, increasing the P/L ratio from 1:20 to 1:7.5 in the DOPC : DOPE membrane increased the uniaxial rotation correlation time of M2TM tetramers from 0.55 μs to 13.9 μs, suggesting protein clustering. This hypothesis was also tested using coarse-grained molecular dynamics simulations, which found that M2TM tetramers cluster in an approximately linear fashion, and the tetramers can adopt both parallel and antiparallel orientations with each other.

EPR spectroscopy studies of M2TM(22-46) and M2C(23-60) peptides showed an equilibrium between two conformer states [204, 211, 212]. Both conformers seem to be present in all membranes tested, while the conformers' relative populations vary greatly with different membrane-lipid compositions. *Cholesterol, thicker membranes, and PE species all favor a "tight" conformer state*, characterized by:

(1) Closer contact distances between residues on neighboring monomers in both the TM and the AH helices,
(2) Lower mobility
(3) Shallower insertion in the membrane and higher solvent accessibility.

Effect (1) was demonstrated by spin-spin coupling between neighboring spin-labeled residues by X-band EPR spectra on M2TM [211, 212] and M2TMC [204] and (2) was demonstrated by continuous-wave (CW) EPR spectra on M2C(23-60) [204]). The membrane insertion effect (3) was viewed through power saturation EPR probing the membrane with O2 and the solvent with NiEDDA [204]. Interestingly, our previously tested VMS membrane (SM:DPPC:DPPE:Chol) pushed the immobile conformer into dominance the most strongly [204].

To ensure the two conformer equilibrium is a true property of full-length wild-type M2, the aforementioned EPR studies were extended to the wild-type (M2-WT) nitroxide-labeled at residue 59 (in the AH); saturation recovery EPR curves had a clear biexponential form that characteristic of true conformer exchange. As with other constructs, cholesterol pushed the TM and AH helices toward the immobile and tighter packed conformation [213].

The aforementioned EPR spectra were measured at ambient temperature (~20˚C) where cholesterol and PE can modulate the membrane viscosity and lateral pressure, which can in turn affect the tetramer conformation. However, the possibility of M2 clustering in these samples cannot be ruled out, even at the low peptide concentrations used in these studies. Even if this conformational distribution exclusively reflects intra-tetramer structural variation, it may already be reflected in the ensemble of orientational structures solved by solid-state NMR, in which the nearest-neighbor Phe47-Phe47 distances varied but never fell below 2.1 nm [196]. These considerations support the model that the measured ^{19}F-^{19}F cross peaks in the 2D ^{19}F spin diffusion spectra predominantly result from inter-tetramer clustering rather than intra-tetramer interactions.

The fluorinated Phe47 allowed us to probe the depth of insertion of this junction between the TM and AH. While most spectra showed a modest lipid-Phe47 cross peak (**Fig. IV.6**), we observed an unexpectedly strong lipid-Phe47 cross peak for M2TM in the POPC : POPG : chol membrane. This result cannot be explained by differential dynamics of the lipids, since we measured these HETCOR spectra at temperatures that give similar lipid proton linewidths and hence similar lipid chain dynamics. Instead, we attribute this strong lipid-Phe47 cross peak to preferential interaction of the Phe47 sidechain with cholesterol, which anchors this residue to the membrane. The propensity of the Phe47 sidechain to insert into the membrane is present in M2CD as well but may be partly restricted by the rest of the amphipathic helix.

The Phe residues of the AH have been previously reported to interact with cholesterol. In DMPC : DMPG : chol (16:4:5) membranes, Phe-^{13}C-labeled full-length M2 and $^{13}C_{2,3,4}$-labeled cholesterol showed cross peaks in 2D ^{13}C-^{13}C correlation spectra [185]. Earlier ^{13}C-^{19}F REDOR experiments of ^{13}C-labeled protein and fluorinated cholesterol showed that an M2TM(22-46) peptide that lacks the ^{47}FFK^{49} motif does not bind cholesterol, whereas an M2CD(22-61) peptide that contains multiple Phe residues does bind half-stoichiometrically [184]. To characterize the binding interface in greater detail, 2D ^{13}C-^{13}C correlation spectra of ^{13}C-labeled M2(21-97) in POPC : POPG : chol

membranes measured with dynamic nuclear polarization (DNP) showed cross peaks between cholesterol C3 and C9 carbons and Phe aromatic carbons [183]. Finally, docking simulations constrained by measured intermolecular distances and cholesterol orientations found that Phe47 was the only Phe that could bind cholesterol [183] without violating experimental distance and cholesterol tilt angle ([184]) restraints. These lines of evidence all indicate that Phe47 interacts with cholesterol, which could explain the strong lipid-Phe47 cross peak.

We did not observe significant difference in the depth of insertion of Phe47 in M2CD between the POPC : POPG : chol membrane and the POPC : POPG membrane (**Fig. IV.6 a, b**). This result differs from power saturation EPR data of M2TMC in POPC : POPG membranes, which found that addition of 30% cholesterol caused AH residues 46, 48, 51 and 55 to be more surface exposed compared to their depths in the non-cholesterol membrane [204]. Three experimental differences could cause this discrepancy. First, our ^{1}H-^{19}F HETCOR spectra were measured in a membrane containing only 17% cholesterol. This low level of cholesterol might not cause a sufficiently large change in the AH insertion depth. Second, we conducted the HETCOR experiments at -10˚C whereas the EPR experiments were conducted at ambient temperature. Since the M2 structure is highly sensitive to the membrane properties, the low temperature at which these HETCOR spectra were measured might reduce the difference in the insertion depth of the AH. Finally, at the temperature of these 2D HETCOR experiments, the lipid chain proton linewidth of the POPC : POPG : chol membrane was ~480 Hz, which was moderately broader than the POPC : POPG lipid linewidth of ~370 Hz. Thus the lipids may be more immobilized in the cholesterol-containing membrane. If this is the case, then the Phe47 sidechain may become slightly less inserted after correcting for this dynamics difference.

Interestingly, the HETCOR spectra indicate that Phe47 is less inserted into the POPE membrane than in the POPC : POPG membranes (**Fig. IV.6 e**). This result is in good agreement with atomic force microscopy (AFM) data that showed that adding POPE into POPC bilayers suppressed the ability of an AH-only peptide to insert into the membrane and to modulate bilayer structure (while addition of 30% cholesterol facilitated larger and deeper M2AH-induced pits in the membrane) [214]. Differential insertion depth of the AH domain may allow M2 to adapt to different membrane environments, and may help modulate the interfacial energy at the L_o/L_d boundary, which is important for inducing membrane curvature [17]. Fluorescence microscopy data of M2-infected cells have shown that M2 congregates at the edge of the budding virion in the host cell membrane [178]. POPE may be recruited to the budozone [207, 208] to promote NGC, both due to its own negative curvature and due to its ability to promote M2 clustering and regulate the depth of insertion of M2. Thus, cholesterol, PE lipids, and M2 may jointly drive membrane scission by associating at the budozone to cause high membrane curvature.

In conclusion, the current ^{19}F and ^{31}P NMR data indicate that both M2CD and M2TM tetramers form clusters in lipid membranes in the presence of cholesterol and PE lipids. Based on the Phe47-Phe47 cross peaks intensities, the tetramers are more

tightly clustered in the POPE membrane than in the 17% cholesterol POPC : POPG : chol membrane. But the inter-tetramer distances are shorter than 2 nm in both membranes in order to account for the observed ^{19}F-^{19}F cross peaks. The membrane with the tightest M2 clusters, POPE, also exhibits the highest NGC and the shallowest insertion of the Phe47 sidechain. These results provide experimental evidence that M2 proteins cluster at the edge of the cholesterol- and PE-rich budding virion to cause membrane curvature, causing an ever-narrower stalk to achieve membrane scission.

Acknowledgement

This work is supported by NIH grant GM088204 to M.H. This study made use of NMR spectrometers at the MIT-Harvard Center for Magnetic Resonance, which is supported by NIH grant P41 GM132079.

Conclusion: Assembling the puzzle

Both this and the prior study (**Chapter III**) investigated the extent to which a membrane remodeling protein inserts a membrane-proximal domain into different membranes – a lipid packing disruption event introduced in **Section I.2.e**. M2's membrane-proximal domain, in this case termed the "Amphipathic Helix" (AH) differs from gp41's MPER, in that M2 AH inserts into cholesterol-containing membranes (**Section IV.3.b**). It is worth noting that in the native systems, gp41 MPER faces the *outer* leaflet of the fusing membranes, while M2 AH faces the *inner* leaflet. Since the C-terminal gp41 TMD's proposed membrane water defects would exist in the inner leaflet, it's possible *both* proteins evolved a mechanism to disrupt lipid packing in specifically the inner leaflet.

At an early stage of fission, M2 may influence membrane geometry through multiple indirect routes. It could recruit POPE in the outer leaflet (as predicted in **Section I.2.d**), to reinforce the negative-curvature neck formation, as this has been shown to facilitate membrane curvature induction (**Section IV.3.c**). It could modulate the L_o/L_d boundary line tension in a manner that promotes curvature (see **Section I.2.b**); this effect seems likely now due to M2's previously demonstrated localization along the L_o/L_d domain boundaries, and the differential behavior between membrane compositions reviewed *and* further demonstrated here (**Section IV.3.a-b**). It's also possible M2 directly induces curvature, as discussed in **Section I.2.a** and demonstrated in **Section IV.3.c**. Within a fission pore structure, in the dimension defined as tangent to the lamellar membrane, M2's wedge shape can potentially reinforce the curvature of both leaflets by pushing the inner leaflet's heads groups closer together, and the outer leaflet's acyl chains closer together.

It is apparent now that M2 proteins proactively form clusters (**Sections I.2.c, IV.3.a**), and it seems likely that clustering reinforces some or all of M2's effects on membrane lipid organization. This study contributed significantly, then, to our understanding of how M2-mediated membrane fission can work.

V. Conclusion

Both membrane remodeling proteins examined here, influenza M2 and HIV gp41, have dozens of partial and complete crystal structures in the PDB. However, it is difficult to characterize how the proteins interact with membrane lipids by any other method than solid-state NMR. Despite decades of studies on these proteins, the mechanistic details of how they deform and break membranes have remained elusive.

In this thesis, we outlined the known modes of membrane perturbation by proteins and used both static ^{31}P and multinuclear MAS spin diffusion experiments to demonstrate which modes applied to our proteins. Our peptide studies suggest that both M2 and gp41 form clusters in some membrane compositions but not others, and deform POPE bilayers into structures with the necessary negative Gaussian curvature for fusion or fission. We find that cholesterol dampens some activities of these peptides and enhances others, and since other groups' fluorescence microscopy and simulation studies found that both proteins localize to the edges between cholesterol-rich L_o and cholesterol-poor L_d domains in the membrane, cholesterol binding can potentially play an important role in the proteins' mechanisms.

Below is a summary of what we now know about each protein's mechanism, incorporating our findings:

Mode of action	***HIV gp41***	***Influenza M2***
Direct curvature induction	Yes (**II.3.a**)	Yes (**IV.3.c**)
Modulating line tension	Almost certainly (literature)	Likely (literature)
Protein clustering	Yes (**III.3.a**)	Yes (**IV.3.a**)
Altering local membrane composition	Unknown	Unknown
Disrupting lipid packing	Likely (**II.3.d**)	Yes (AH insertion, **IV.3.b**)

Protein clustering, now demonstrated for both M2 (**Section IV.3.a**) and gp41 (**Section III.3.a**), should allow the proteins to act collectively on the membrane. We are less certain about *which* actions are being taken collectively. In the future, to assemble all the pieces of these mechanistic puzzles, it would help to determine the elastic moduli of realistic membranes, and how much stress each of the above modes of action can exert upon the membranes. We are building toward robust and rigorous experimental estimates of the membranes' minimum necessary steps to enable viral-host membrane fusion and fission, which heretofore has mainly been predicted on theoretical grounds (i.e. [9, 215, 216]).

Further, functional characterization of the proteins in membranes with realistic L_o/L_d domain separation should help us understand how far and in what direction gp41 and M2 alter the line tension at the boundary, and what role this plays in their mechanisms. This is a critical piece of information because (1) as discussed earlier (**Section I.2.b**), high line also enhances membrane curvature, which is required for fusion and fission, and (2) both proteins were previously demonstrated to localize to L_o/L_d domain boundaries.

Finally, we studied the interplay between membrane remodeling proteins, lipids, cholesterol and water, but the role of ions in the media also should also be incorporated into the picture. In fact, there is evidence that the initial step of HIV entry, gp120 engagement of CD4 and CXCR4, leads to a flux of calcium ions into the cell [217]. A discussion of the myriad potential and demonstrated impacts of calcium on the local organization of lipids and bound waters is beyond the scope of this work. With that said, there is a clear need for future studies to explore how these effects could play a role in membrane fusion and even membrane fission.

Chemists studying biomolecules don't often have the opportunity to think about stress, strain and material elastic moduli, but plasma membranes are materials. Thus, the community of chemists working on membrane questions may have a collective learning experience ahead of us, as we strive toward greater understanding how viral membrane fusion and fission works.

Acknowledgements:

I wish to thank Prof. Mei Hong for training me in and increasing my love for solid-state NMR, guiding these studies, and facilitating my transition to physical chemistry. All members of the Hong group provided helpful technical input, as well as robust and enjoyable scientific discussions. Dr.'s Adam Willard and Laura Kiessling also provided insightful and constructive scientific input throughout this investigation.

I also wish to thank my partner, Dr. Dibbyan Mazumder, for being a constant source of support and teaching me a bit about elastic mechanics. My grandfather, George Rhodes, provided interesting discussions, a listening ear and moral support at every stage of my education. My mother, Heather Rhodes, did the same and even provided copy editing services on this thesis. My best friends, my chosen family, Jessica Blucher and Amanda Cowfer, provided innumerable forms of support in getting me through my grad school experience from start to finish. The MIT Graduate Student Union provided invaluable community support. Nobody finishes a PhD on their own, so every degree awarded is truly a group victory.

"And despite all this search and investigation, we cannot absolve ourselves from human frailties, but, granted whatever faculty we have, we shall strive and address ourselves in supplication to Almighty God that He vouchsafe to us courage and help."

- Ibn al-Haitham [218], originator of the modern scientific method

References

[1] J. Renju, M. Moshabela, E. McLean, W. Ddaaki, M. Skovdal, F. Odongo, D. Bukenya, J. Wamoyi, O. Bonnington, J. Seeley, B. Zaba, A. Wringe, 'Side effects' are 'central effects' that challenge retention in HIV treatment programmes in six sub-Saharan African countries: a multicountry qualitative study, Sex Transm Infect, 93 (2017).
[2] W.H.O., HIV Drug Resistance Report 2019, in, WHO/CDS/HIV/19.21, Geneva, Switzerland, 2019.
[3] C. Beyrer, A. Pozniak, HIV Drug Resistance — An Emerging Threat to Epidemic Control, N Engl J Med, 377 (2017).
[4] F.S. Wang, L. Zhang, D. Douek, A. McMichael, X.N. Xu, S.R. Lewin, Strategies for an HIV cure: progress and challenges, Nat Immunol, 19 (2018) 1155-1158.
[5] Past Seasons Estimated Influenza Disease Burden, in, Center for Disease Control and Prevention, 2020.
[6] M.M. Patel, I.A. York, A.S. Monto, M.G. Thompson, A.M. Fry, Immune-mediated attenuation of influenza illness after infection: opportunities and challenges, The Lancet Microbe, (2021).
[7] A.H. Villamagna, S.J. Gore, J.S. Lewis, J.S. Doggett, The Need for Antiviral Drugs for Pandemic Coronaviruses From a Global Health Perspective, Front Med (Lausanne), 7 (2020) 596587.
[8] G. Zhao, J.R. Perilla, E.L. Yufenyuy, X. Meng, B. Chen, J. Ning, J. Ahn, A.M. Gronenborn, K. Schulten, C. Aiken, P. Zhang, Mature HIV-1 capsid structure by cryo-electron microscopy and all-atom molecular dynamics, Nature, 497 (2013) 643-646.
[9] L.V. Chernomordik, M.M. Kozlov, Protein-lipid interplay in fusion and fission of biological membranes, Annu Rev Biochem, 72 (2003) 175-207.
[10] B. Kollmitzer, P. Heftberger, M. Rappolt, G. Pabst, Monolayer spontaneous curvature of raft-forming membrane lipids, Soft Matter, 9 (2013) 10877-10884.
[11] N. Fuller, R.P. Rand, The Influence of Lysolipids on the Spontaneous Curvature and Bending Elasticity of Phospholipid Membranes, Biophysical journal, 81 (2001) 243-254.
[12] T. Hirama, S.M. Lu, J.G. Kay, M. Maekawa, M.M. Kozlov, S. Grinstein, G.D. Fairn, Membrane curvature induced by proximity of anionic phospholipids can initiate endocytosis, Nature communications, 8 (2017).
[13] L.J. Pike, The challenge of lipid rafts, Journal of lipid research, 50 (2009) S323-S328.
[14] P.J. Quinn, C. Wolf, The liquid-ordered phase in membranes, Biochimica et Biophysica Acta (BBA) - Biomembranes, 1788 (2009) 33-46.
[15] A. Bunge, P. Muller, M. Stockl, A. Herrmann, D. Huster, Characterization of the ternary mixture of sphingomyelin, POPC, and cholesterol: support for an inhomogeneous lipid distribution at high temperatures, Biophys J, 94 (2008) 2680-2690.
[16] P.I. Kuzmin, S.A. Akimov, Y.A. Chizmadzhev, J. Zimmerberg, F.S. Cohen, Line tension and interaction energies of membrane rafts calculated from lipid splay and tilt, Biophys J, 88 (2005) 1120-1133.
[17] A.J. García-Sáez, S. Chiantia, P. Schwille, Effect of line tension on the lateral organization of lipid membranes, J. Biol. Chem., 282 (2007) 33537-33544.

[18] D.J. Benvegnu, H.M. McConnell, Line Tension between Liquid Domains In Lipid Monolayers, J Phys Chem, 96 (1992) 6820-6824.
[19] S. Trabelsi, S. Zhang, T.R. Lee, D.K. Schwartz, Linactants: surfactant analogues in two dimensions, Phys Rev Lett, 100 (2008) 037802.
[20] S.-T. Yang, V. Kiessling, L.K. Tamm, Line tension at lipid phase boundaries as driving force for HIV fusion peptide-mediated fusion, Nat Commun, 7 (2016).
[21] J.J. Madsen, J.M.A. Grime, J.S. Rossman, G.A. Voth, Entropic forces drive clustering and spatial localization of influenza A M2 during viral budding, Proc Natl Acad Sci U S A, 115 (2018) E8595-e8603.
[22] J. Chojnacki, T. Staudt, B. Glass, P. Bingen, J. Engelhardt, M. Anders, J. Schneider, B. Müller, S.W. Hell, H.G. Kräusslich, Maturation-dependent HIV-1 surface protein redistribution revealed by fluorescence nanoscopy, Science, 338 (2012) 524-528.
[23] J. Sajman, M. Trus, D. Atlas, E. Sherman, The L-type Voltage-Gated Calcium Channel co-localizes with Syntaxin 1A in nano-clusters at the plasma membrane, Sci Rep, 7 (2017) 11350.
[24] Y. Hua, R.H. Scheller, Three SNARE complexes cooperate to mediate membrane fusion, Proc. Natl. Acad. Sci. U.S.A., 98 (2001) 8065.
[25] D. Milovanovic, A. Honigmann, S. Koike, F. Göttfert, G. Pähler, M. Junius, S. Müllar, U. Diederichsen, A. Janshoff, H. Grubmüller, H.J. Risselada, C. Eggeling, S.W. Hell, G. van den Bogaart, R. Jahn, Hydrophobic mismatch sorts SNARE proteins into distinct membrane domains, Nat. Commun., 6 (2015) 5984.
[26] G. van den Bogaart, K. Meyenberg, H.J. Risselada, H. Amin, K.I. Willig, B.E. Hubrich, M. Dier, S.W. Hell, H. Grubmüller, U. Diederichsen, R. Jahn, Membrane protein sequestering by ionic protein–lipid interactions, Nature, 479 (2011) 552-555.
[27] M. Paraan, J. Mendez, S. Sharum, D. Kurtin, H. He, S.M. Stagg, The structures of natively assembled clathrin-coated vesicles, Science Advances, 6 (2020) eaba8397.
[28] J.E. Donald, Y. Zhang, G. Fiorin, V. Carnevale, D.R. Slochower, F. Gai, M.L. Klein, W.F. DeGrado, Transmembrane orientation and possible role of the fusogenic peptide from parainfluenza virus 5 (PIV5) in promoting fusion, Proc Natl Acad Sci U S A, 108 (2011) 3958-3963.
[29] H. Yao, M. Hong, Conformation and Lipid Interaction of the Fusion Peptide of the Paramyxovirus PIV5 in Anionic and Negative-Curvature Membranes From Solid-State NMR, Journal of the American Chemical Society, 136 (2014) 2611-2624.
[30] M.S. Bretscher, Asymmetrical Lipid Bilayer Structure for Biological Membranes, Nature New Biology, 236 (1972) 11-12.
[31] G. van Meer, Dynamic transbilayer lipid asymmetry, Cold Spring Harb Perspect Biol, 3 (2011).
[32] E.M. Bevers, P.L. Williamson, Getting to the Outer Leaflet: Physiology of Phosphatidylserine Exposure at the Plasma Membrane, Physiol Rev, 96 (2016) 605-645.
[33] M.K. Callahan, P.M. Popernack, S. Tsutsui, L. Truong, R.A. Schlegel, A.J. Henderson, Phosphatidylserine on HIV envelope is a cofactor for infection of monocytic cells, J Immunol, 170 (2003) 4840-4845.

[34] S.T. Henriques, Y.H. Huang, M.A. Castanho, L.A. Bagatolli, S. Sonza, G. Tachedjian, N.L. Daly, D.J. Craik, Phosphatidylethanolamine binding is a conserved feature of cyclotide-membrane interactions, J Biol Chem, 287 (2012) 33629-33643.
[35] W. Qiang, Y. Sun, D.P. Weliky, A strong correlation between fusogenicity and membrane insertion depth of the HIV fusion peptide, Proc Natl Acad Sci U S A, 106 (2009) 15314-15319.
[36] A. Piai, J. Dev, Q. Fu, J.J. Chou, Stability and Water Accessibility of the Trimeric Membrane Anchors of the HIV-1 Envelope Spikes, J Am Chem Soc, 139 (2017) 18432-18435.
[37] M. Hong, K. Schmidt-Rohr, Magic-angle-spinning NMR techniques for measuring long-range distances in biological macromolecules, Acc Chem Res, 46 (2013) 2154-2163.
[38] K.K. Kumashiro, K. Schmidt-Rohr, O.J. Murphy, K.L. Ouellette, W.A. Cramer, L.K. Thompson, A Novel Tool for Probing Membrane Protein Structure: Solid-State NMR with Proton Spin Diffusion and X-Nucleus Detection, JACS, 120 (1998) 5043-5051.
[39] D. Huster, X. Yao, M. Hong, Membrane Protein Topology Probed by 1H Spin Diffusion from Lipids Using Solid-State NMR Spectroscopy, JACS, 124 (2002) 874-883.
[40] G. Hou, S. Yan, J. Trebosc, J.P. Amoureux, T. Polenova, Broadband homonuclear correlation spectroscopy driven by combined R2(n)(v) sequences under fast magic angle spinning for NMR structural analysis of organic and biological solids, J. Magn. Reson., 232 (2013) 18-30.
[41] K. Schmidt-Rohr, H.W. Spiess, Multidimensional Solid-State NMR and Polymers, Academic Press Inc, San Diego, CA, 1994.
[42] R. Mani, S.D. Cady, M. Tang, A.J. Waring, R.I. Lehrer, M. Hong, Membrane-dependent oligomeric structure and pore formation of a beta-hairpin antimicrobial peptide in lipid bilayers from solid-state NMR, Proc Natl Acad Sci U S A, 103 (2006) 16242-16247.
[43] W. Luo, M. Hong, Conformational Changes of an Ion Channel Detected Through Water-Protein Interactions Using Solid-State NMR
Spectroscopy, JACS, 132 (2010) 2378–2384.
[44] S.L. Grage, S. Afonin, A.S. Ulrich, 19F NMR of biomembranes, in: Solid-State NMR, 2020.
[45] D.H. Gregory, J.T. Gerig, Structural Effects of Fluorine Substitution in Proteins, J Comput Chem, 12 (1991) 180-185.
[46] M. Salwiczek, E.K. Nyakatura, U.I. Gerling, S. Ye, B. Koksch, Fluorinated amino acids: compatibility with native protein structures and effects on protein-protein interactions, Chem Soc Rev, 41 (2012) 2135-2171.
[47] L. Merkel, M. Schauer, G. Antranikian, N. Budisa, Parallel incorporation of different fluorinated amino acids: on the way to "teflon" proteins, Chembiochem, 11 (2010) 1505-1507.
[48] Y. Hou, W. Hu, X. Li, J.J. Skinner, D. Liu, K. Wuthrich, Solvent-accessibility of discrete residue positions in the polypeptide hormone glucagon by (19)F-NMR observation of 4-fluorophenylalanine, J Biomol NMR, 68 (2017) 1-6.
[49] M.A. Danielson, J.J. Falk, Use of 19F NMR to probe protein structure and conformatioinal changes, Annu Rev Biophys Biomol Struct, 25 (1996) 163-195.

[50] A.A. Shcherbakov, M. Roos, B. Kwon, M. Hong, Two-dimensional 19F-13C correlation NMR for 19F resonance assignment of fluorinated proteins, J. Biomol. NMR, 74 (2020) 193-204.
[51] M. Roos, T. Wang, A.A. Shcherbakov, M. Hong, Fast Magic-Angle-Spinning (19)F Spin Exchange NMR for Determining Nanometer (19)F-(19)F Distances in Proteins and Pharmaceutical Compounds, J. Phys. Chem. B, 122 (2018) 2900-2911.
[52] A.A. Shcherbakov, J. Medeiros-Silva, N. Tran, M.D. Gelenter, M. Hong, From Angstroms to Nanometers: Measuring Interatomic Distances by Solid-State NMR, Chem Rev, (2021).
[53] B. Kwon, T. Mandal, M.R. Elkins, Y. Oh, Q. Cui, M. Hong, Cholesterol Interaction with the Trimeric HIV Fusion Protein gp41 in Lipid Bilayers Investigated by Solid-State NMR Spectroscopy and Molecular Dynamics Simulations, J Mol Biol, 432 (2020) 4705-4721.
[54] M.R. Elkins, A. Bandara, G.A. Pantelopulos, J.E. Straub, M. Hong, Direct Observation of Cholesterol Dimers and Tetramers in Lipid Bilayers, J Phys Chem B, 125 (2021) 1825-1837.
[55] D. Weissman, R.L. Rabin, J. Arthos, A. Rubbert, M. Dybul, R. Swofford, S. Venkatesan, J.M. Farber, A.S. Fauci, Macrophage-tropic HIV and SIV envelope proteins induce a signal through the CCR5 chemokine receptor, Nature, 389 (1997) 981-985.
[56] B. Chen, Molecular Mechanism of HIV-1 Entry, Trends Microbiol, 27 (2019) 878-891.
[57] D.R. Burton, L. Hangartner, Broadly Neutralizing Antibodies to HIV and Their Role in Vaccine Design, Annual Review of Immunology, 34 (2016) 635-659.
[58] S.C. Harrison, Viral membrane fusion, Virology, 479-480 (2015) 498-507.
[59] F.S. Cohen, G.B. Melikyan, The energetics of membrane fusion from binding, through hemifusion, pore formation, and pore enlargement, J Membr Biol, 199 (2004) 1-14.
[60] R.A. Lamb, T.S. Jardetzky, Structural basis of viral invasion: lessons from paramyxovirus F, Curr Opin Struct Biol, 17 (2007) 427-436.
[61] H.-S. Yin, X. Wen, R.G. Paterson, R.A. Lamb, T.S. Jardetzky, Structure of the parainfluenza virus 5 F protein in its metastable, prefusion conformation, Nature, 439 (2006) 38-44.
[62] H.-S. Yin, R.G. Paterson, X. Wen, R.A. Lamb, T.S. Jardetzky, Structure of the uncleaved ectodomain of the paramyxovirus (hPIV3) fusion protein, Proceedings of the National Academy of Sciences of the United States of America, 102 (2005) 9288-9293.
[63] D.C. Chan, D. Fass, J.M. Berger, P.S. Kim, Core structure of gp41 from the HIV envelope glycoprotein, Cell, 89 (1997) 263-273.
[64] W. Weissenhorn, A. Dessen, S.C. Harrison, J.J. Skehel, D.C. Wiley, Atomic structure of the ectodomain from HIV-1 gp41, Nature, 387 (1997) 426-430.
[65] Y.H. Kim, J.E. Donald, G. Grigoryan, G.P. Leser, A.Y. Fadeev, R.A. Lamb, W.F. DeGrado, Capture and imaging of a prehairpin fusion intermediate of the paramyxovirus PIV5, Proceedings of the National Academy of Sciences, 108 (2011) 20992-20997.
[66] G. Frey, H. Peng, S. Rits-Volloch, M. Morelli, Y. Cheng, B. Chen, A fusion-intermediate state of HIV-1 gp41 targeted by broadly neutralizing antibodies, Proceedings of the National Academy of Sciences, 105 (2008) 3739-3744.

[67] B. Kwon, M. Lee, A.J. Waring, M. Hong, Oligomeric Structure and Three-Dimensional Fold of the HIV gp41 Membrane-Proximal External Region and Transmembrane Domain in Phospholipid Bilayers, J. Am. Chem. Soc., 140 (2018) 8246-8259.
[68] Q. Fu, M.M. Shaik, Y. Cai, F. Ghantous, A. Piai, H. Peng, S. Rits-Volloch, Z. Liu, S.C. Harrison, M.S. Seaman, B. Chen, J.J. Chou, Structure of the membrane proximal external region of HIV-1 envelope glycoprotein, Proc Natl Acad Sci U S A, 115 (2018) E8892-E8899.
[69] J. Dev, D. Park, Q. Fu, J. Chen, H.J. Ha, F. Ghantous, T. Herrmann, W. Chang, Z. Liu, G. Frey, M.S. Seaman, B. Chen, J.J. Chou, Structural basis for membrane anchoring of HIV-1 envelope spike, Science, 353 (2016) 172-175.
[70] S.C. Chiliveri, J.M. Louis, R. Ghirlando, J.L. Baber, A. Bax, Tilted, Uninterrupted, Monomeric HIV-1 gp41 Transmembrane Helix from Residual Dipolar Couplings, J Am Chem Soc, 140 (2018) 34-37.
[71] M. Lee, C.A. Morgan, M. Hong, Fully hydrophobic HIV gp41 adopts a hemifusion-like conformation in phospholipid bilayers, J Biol Chem, 294 (2019) 14732-14744.
[72] H. Yao, M. Lee, S.Y. Liao, M. Hong, Solid-State Nuclear Magnetic Resonance Investigation of the Structural Topology and Lipid Interactions of a Viral Fusion Protein Chimera Containing the Fusion Peptide and Transmembrane Domain, Biochemistry, 55 (2016) 6787-6800.
[73] N.W. Schmidt, A. Mishra, G.H. Lai, M. Davis, L.K. Sanders, D. Tran, A. Garcia, K.P. Tai, P.B. McCray, A.J. Ouellette, M.E. Selsted, G.C.L. Wong, Criterion for Amino Acid Composition of Defensins and Antimicrobial Peptides Based on Geometry of Membrane Destabilization, Journal of the American Chemical Society, 133 (2011) 6720-6727.
[74] N.W. Schmidt, A. Mishra, J. Wang, W.F. DeGrado, G.C. Wong, Influenza virus A M2 protein generates negative Gaussian membrane curvature necessary for budding and scission, J Am Chem Soc, 135 (2013) 13710-13719.
[75] H. Yao, M.W. Lee, A.J. Waring, G.C. Wong, M. Hong, Viral fusion protein transmembrane domain adopts beta-strand structure to facilitate membrane topological changes for virus-cell fusion, Proc. Natl. Acad. Sci. USA, 112 (2015) 10926-10931.
[76] D.P. Siegel, R.M. Epand, Effect of influenza hemagglutinin fusion peptide on lamellar/inverted phase transitions in dipalmitoleoylphosphatidylethanolamine: implications for membrane fusion mechanisms, Biochimica et Biophysica Acta (BBA) - Biomembranes, 1468 (2000) 87-98.
[77] Y. Yang, H. Yao, M. Hong, Distinguishing Bicontinuous Lipid Cubic Phases from Isotropic Membrane Morphologies Using 31P Solid-State NMR Spectroscopy, J. Phys. Chem., 119 (2015) 4993-5001.
[78] E. Zaitseva, E. Zaitsev, K. Melikov, A. Arakelyan, M. Marin, R. Villasmil, L.B. Margolis, G.B. Melikyan, L.V. Chernomordik, Fusion Stage of HIV-1 Entry Depends on Virus-Induced Cell Surface Exposure of Phosphatidylserine, Cell Host Microbe, 22 (2017) 99-110 e117.
[79] Z.H. Liao, D.R. Graham, J.E.K. Hildreth, Lipid rafts and HIV pathogenesis: Virion-associated cholesterol is required for fusion and infection of susceptible cells, Aids Res Hum Retrov, 19 (2003) 675-687.

[80] S.T. Yang, V. Kiessling, J.A. Simmons, J.M. White, L.K. Tamm, HIV gp41-mediated membrane fusion occurs at edges of cholesterol-rich lipid domains, Nat. Chem. Biol., 11 (2015) 424-431.
[81] G.C. Carter, L. Bernstone, D. Sangani, J.W. Bee, T. Harder, W. James, HIV entry in macrophages is dependent on intact lipid rafts, Virology, 386 (2009) 192-202.
[82] M.K. Domanska, D. Wrona, P.M. Kasson, Multiphasic effects of cholesterol on influenza fusion kinetics reflect multiple mechanistic roles, Biophys J, 105 (2013) 1383-1387.
[83] M. Lorizate, T. Sachsenheimer, B. Glass, A. Habermann, M.J. Gerl, H.G. Kräusslich, B. Brügger, Comparative lipidomics analysis of HIV-1 particles and their producer cell membrane in different cell lines, Cell Microbiol., 15 (2013) 292-304.
[84] C.M. Gabrys, R. Yang, C.M. Wasniewski, J. Yang, C.G. Canlas, W. Qiang, Y. Sun, D.P. Weliky, Nuclear magnetic resonance evidence for retention of a lamellar membrane phase with curvature in the presence of large quantities of the HIV fusion peptide, Biochim Biophys Acta, 1798 (2010) 194-201.
[85] B. Brügger, B. Glass, P. Haberkant, I. Leibrecht, F.T. Wieland, H.G. Krausslich, The HIV lipidome: A raft with an unusual composition, Proceedings of the National Academy of Sciences of the United States of America, 103 (2006) 2641-2646.
[86] P. Zhu, E. Chertova, J. Bess, Jr., J.D. Lifson, L.O. Arthur, J. Liu, K.A. Taylor, K.H. Roux, Electron tomography analysis of envelope glycoprotein trimers on HIV and simian immunodeficiency virus virions, Proc Natl Acad Sci U S A, 100 (2003) 15812-15817.
[87] D. Lingwood, K. Simons, Lipid rafts as a membrane-organizing principle, Science, 327 (2010) 46-50.
[88] N.T. Back, L. Smit, M. Schutten, P.L. Nara, M. Tersmette, J. Goudsmit, Mutations in Human Immunodeficiency Virus Type 1 gp4l Affect Sensitivity to Neutralization by gpl20 Antibodies, Journal of virology, 67 (1993) 6897-6902.
[89] M.D. Simon, P.L. Heider, A. Adamo, A.A. Vinogradov, S.K. Mong, X. Li, T. Berger, R.L. Policarpo, C. Zhang, Y. Zou, X. Liao, A.M. Spokoyny, K.F. Jensen, B.L. Pentelute, Rapid flow-based peptide synthesis, Chembiochem, 15 (2014) 713-720.
[90] A.-R. Grimmer, A. Kretschmer, V.B. Cajipe, Influence of Magic Angle Spinning on Sample Temperature, Magn Reson Chem, 35 (1997) 86-90.
[91] A. Böckmann, C. Gardiennet, R. Verel, A. Hunkeler, A. Loquet, G. Pintacuda, L. Emsley, B.H. Meier, A. Lesage, Characterization of different water pools in solid-state NMR protein samples, J Biomol NMR, 45 (2009) 319-327.
[92] R. Mani, J.J. Buffy, A.J. Waring, R.I. Lehrer, M. Hong, Solid-State NMR Investigation of the Selective Disruption of Lipid Membranes by Protegrin-1, Biochemistry, 43 (2004) 13839-13848.
[93] G. van Meer, D.R. Voelker, G.W. Feigenson, Membrane lipids: where they are and how they behave, Nat Rev Mol Cell Biol, 9 (2008) 112-124.
[94] K. Kastl, M. Menke, E. Luthgens, S. Faiss, V. Gerke, A. Janshoff, C. Steinem, Partially reversible adsorption of annexin A1 on POPC/POPS bilayers investigated by QCM measurements, SFM, and DMC simulations, Chembiochem, 7 (2006) 106-115.
[95] J.R. Silvius, J. Gagné, Calcium-Induced Fusion and Lateral Phase Separations in Phosphatidylcholine-Phosphatidylserine Vesicles. Correlation by Calorimetric and Fusion Measurements, Biochemistry, 23 (1984) 3241-3247.

[96] F. Lindström, P.T.F. Williamson, G. Gröbner, Molecular Insight into the Electrostatic Membrane Surface Potential by 14N/31P MAS NMR Spectroscopy: Nociceptin-Lipid Association, JACS, 127 (2005) 6610-6616.
[97] L.K. Tamm, J. Crane, V. Kiessling, Membrane fusion: a structural perspective on the interplay of lipids and proteins, Current Opinion in Structural Biology, 13 (2003) 453-466.
[98] R.P. Rand, V.A. Parsegjan, Physical force considerations in model and biological membranes, Can. J. Biochem. Cell Biol, 62 (1984) 752-775.
[99] G.M.S.a.B.S. Karol S. Bruzik, 13C CP-MAS study of the gel phases of 1,2-dipalmitoylphosphatidylcholine, Bba-Biomembranes, 1023 (1990) 143-146.
[100] J. Frye, A.D. Albert, B.S. Selinsky, P.L. Yeaglex, Cross Polarization P-31 Nuclear Magnetic Resonance of Phospholipids, Biophys J, 48 (1985) 547-552.
[101] T. Doherty, M. Hong, 2D 1H-31P solid-state NMR studies of the dependence of inter-bilayer water dynamics on lipid headgroup structure and membrane peptides, J Magn Reson, 196 (2009) 39-47.
[102] D. Huster, K. Gawrisch, NOESY NMR Crosspeaks between Lipid Headgroups and Hydrocarbon Chains: Spin Diffusion or Molecular Disorder?, Journal of the American Chemical Society, 121 (1999) 1992-1993.
[103] S.E. Feller, C.A. Brown, D.T. Nizza, K. Gawrisch, Nuclear Overhauser Enhancement Spectroscopy Cross-Relaxation Rates and Ethanol Distribution across Membranes, Biophysical journal, 82 (2002) 1396-1404.
[104] H. Yao, M. Hong, Membrane-dependent conformation, dynamics, and lipid interactions of the fusion peptide of the paramyxovirus PIV5 from solid-state NMR, J Mol Biol, 425 (2013) 563-576.
[105] Z.H. Liao, L.M. Cimakasky, R. Hampton, D.H. Nguyen, J.E.K. Hildreth, Lipid rafts and HIV pathogenesis: Host membrane cholesterol is required for infection by HIV type 1, AIDS Res. Hum. Retrovir., 17 (2001) 1009-1019.
[106] J.R. Silvius, Cholesterol Modulation of Lipid Intermixing in Phospholipid and Glycosphingolipid Mixtures. Evaluation Using Fluorescent Lipid Probes and Brominated Lipid Quenchers, Biochemistry, 31 (1992) 3398-3408.
[107] W.F. Zeno, A. Rystov, D.Y. Sasaki, S.H. Risbud, M.L. Longo, Crowding-Induced Mixing Behavior of Lipid Bilayers: Examination of Mixing Energy, Phase, Packing Geometry, and Reversibility, Langmuir, 32 (2016) 4688-4697.
[108] D. Huster, K. Arnold, K. Gawrisch, Influence of Docosahexaenoic Acid and Cholesterol on Lateral Lipid Organization in Phospholipid Mixtures, Biochemistry, 37 (1998) 17299-17308.
[109] B. van Wilgenburg, M.D. Moore, W.S. James, S.A. Cowley, The Productive Entry Pathway of HIV-1 in Macrophages Is Dependent on Endocytosis through Lipid Rafts Containing CD4, PLOS ONE, 9 (2014) e86071.
[110] T. Wang, S.D. Cady, M. Hong, NMR determination of protein partitioning into membrane domains with different curvatures and application to the influenza M2 peptide, Biophys J, 102 (2012) 787-794.
[111] M.K. Baker, V.K. Gangupomu, C.F. Abrams, Characterization of the water defect at the HIV-1 gp41 membrane spanning domain in bilayers with and without cholesterol using molecular simulations, Biochim Biophys Acta, 1838 (2014) 1396-1405.

[112] A.A. Waheed, E.O. Freed, Lipids and membrane microdomains in HIV-1 replication, Virus Res., 143 (2009) 162-176.
[113] R.H. Cheng, R.J. Kuhn, N.H. Olson, M.G. Rossmann, H.K. Choi, T.J. Smith, T.S. Baker, Nucleocapsid and glycoprotein organization in an enveloped virus, Cell, 80 (1995) 621-630.
[114] A. Harris, G. Cardone, D.C. Winkler, J.B. Heymann, M. Brecher, J.M. White, A.C. Steven, Influenza virus pleiomorphy characterized by cryoelectron tomography, Proc. Natl. Acad. Sci. U.S.A., 103 (2006) 19123.
[115] R. Sougrat, A. Bartesaghi, J.D. Lifson, A.E. Bennett, J.W. Bess, D.J. Zabransky, S. Subramaniam, Electron Tomography of the Contact between T Cells and SIV/HIV-1: Implications for Viral Entry, PLoS Pathog., 3 (2007) e63.
[116] J. Chojnacki, T. Staudt, B. Glass, P. Bingen, J. Engelhardt, M. Anders, J. Schneider, B. Müller, S.W. Hell, H.-G. Kräusslich, Maturation-Dependent HIV-1 Surface Protein Redistribution Revealed by Fluorescence Nanoscopy, Science, 338 (2012) 524.
[117] J. Chojnacki, D. Waithe, P. Carravilla, N. Huarte, S. Galiani, J. Enderlein, C. Eggeling, Envelope glycoprotein mobility on HIV-1 particles depends on the virus maturation state, Nat. Commun., 8 (2017) 545.
[118] J.A. Nieto-Garai, A. Arboleya, S. Otaegi, J. Chojnacki, J. Casas, G. Fabriàs, F.X. Contreras, H.-G. Kräusslich, M. Lorizate, Cholesterol in the Viral Membrane is a Molecular Switch Governing HIV-1 Env Clustering, Adv. Sci., 8 (2021) 2003468.
[119] D.J. Wyma, J. Jiang, J. Shi, J. Zhou, J.E. Lineberger, M.D. Miller, C. Aiken, Coupling of Human Immunodeficiency Virus Type 1 Fusion to Virion Maturation: a Novel Role of the gp41 Cytoplasmic Tail, J. Virol., 78 (2004) 3429.
[120] T. Murakami, S. Ablan, E.O. Freed, Y. Tanaka, Regulation of Human Immunodeficiency Virus Type 1 Env-Mediated Membrane Fusion by Viral Protease Activity, J. Virol., 78 (2004) 1026.
[121] Z.Y. Sun, K.J. Oh, M. Kim, J. Yu, V. Brusic, L. Song, Z. Qiao, J.H. Wang, G. Wagner, E.L. Reinherz, HIV-1 broadly neutralizing antibody extracts its epitope from a kinked gp41 ectodomain region on the viral membrane, Immunity, 28 (2008) 52-63.
[122] T. Suárez, W.R. Gallaher, A. Agirre, F.M. Goñi, J.L. Nieva, Membrane Interface-Interacting Sequences within the Ectodomain of the Human Immunodeficiency Virus Type 1 Envelope Glycoprotein: Putative Role during Viral Fusion, J. Virol., 74 (2000) 8038.
[123] R.M. Epand, B.G. Sayer, R.F. Epand, Peptide-induced formation of cholesterol-rich domains, Biochemistry, 42 (2003) 14677-14689.
[124] A. Saez-Cirion, S. Nir, M. Lorizate, A. Agirre, A. Cruz, J. Perez-Gil, J.L. Nieva, Sphingomyelin and cholesterol promote HIV-1 gp41 pretransmembrane sequence surface aggregation and membrane restructuring, J. Biol. Chem., 277 (2002) 21776-21785.
[125] B. Kwon, T. Mandal, M.R. Elkins, Y. Oh, Q. Cui, M. Hong, Cholesterol Interaction with the Trimeric HIV Fusion Protein gp41 in Lipid Bilayers Investigated by Solid-State NMR Spectroscopy and Molecular Dynamics Simulations, J. Mol. Biol., 432 (2020) 4705-4721.
[126] S.M. Campbell, S.M. Crowe, J. Mak, Virion-associated cholesterol is critical for the maintenance of HIV-1 structure and infectivity, AIDS, 16 (2002) 2253-2261.

[127] Y.-H. Zheng, A. Plemenitas, C.J. Fielding, B.M. Peterlin, Nef increases the synthesis of and transports cholesterol to lipid rafts and HIV-1 progeny virions, Proc. Natl. Acad. Sci. U.S.A., 100 (2003) 8460.
[128] A.J. Mijalis, D.A. Thomas, 3rd, M.D. Simon, A. Adamo, R. Beaumont, K.F. Jensen, B.L. Pentelute, A fully automated flow-based approach for accelerated peptide synthesis, Nat. Chem. Biol., 13 (2017) 464-466.
[129] R.C. Aloia, H. Tian, F.C. Jensen, Lipid composition and fluidity of the human immunodeficiency virus envelope and host cell plasma membranes, Proceedings of the National Academy of Sciences, 90 (1993) 5181-5185.
[130] A.E. Bennett, C.M. Rienstra, M. Auger, K.V. Lakshmi, R.G. Griffin, Heteronuclear decoupling in rotating solids., J. Chem. Phys., 103 (1995) 6951-6958.
[131] S. Jo, T. Kim, V.G. Iyer, W. Im, CHARMM-GUI: a web-based graphical user interface for CHARMM, J. Comput. Chem., 29 (2008) 1859-1865.
[132] S. Jo, J.B. Lim, J.B. Klauda, W. Im, CHARMM-GUI Membrane Builder for mixed bilayers and its application to yeast membranes, Biophys. J., 97 (2009) 50-58.
[133] J. Huang, A. D. MacKerell Jr., CHARMM36 all-atom additive protein force field: Validation based on comparison to NMR data, J. Comput. Chem., 34 (2013) 2135--2145.
[134] J.B. Klauda, R.M. Venable, J.A. Freites, J.W. O'Connor, D.J. Tobias, C. Mondragon-Ramirez, I. Vorobyov, A.D. MacKerell Jr, R.W. Pastor, Update of the CHARMM all-atom additive force field for lipids: validation on six lipid types, J. Phys. Chem. B, 114 (2010) 7830-7843.
[135] W.L. Jorgensen, J. Chandrasekhar, J.D. Madura, R.W. Impey, M.L. Klein, Comparison of simple potential functions for simulating liquid water, J. Chem. Phys., 79 (1983) 926-935.
[136] Y.Z. Ohkubo, T.V. Pogorelov, M.J. Arcario, G.A. Christensen, E. Tajkhorshid, Accelerating membrane insertion of peripheral proteins with a novel membrane mimetic model, Biophys. J., 102 (2012) 2130-2139.
[137] Y. Qi, X. Cheng, J. Lee, J.V. Vermaas, T.V. Pogorelov, E. Tajkhorshid, S. Park, J.B. Klauda, W. Im, CHARMM-GUI HMMM Builder for Membrane Simulations with the Highly Mobile Membrane-Mimetic Model, Biophys. J., 109 (2015) 2012-2022.
[138] M. Parrinello, A. Rahman, Polymorphic transitions in single crystals: A new molecular dynamics method, J. Appl. Phys., 52 (1981) 7182-7190.
[139] S. Nose, A unified formulation of the constant temperature molecular dynamics methods, J. Chem. Phys., 81 (1984) 511-519.
[140] W.G. Hoover, Canonical dynamics: Equilibrium phase-space distributions, Phys. Rev. A, 31 (1985) 1695-1697.
[141] B. Hess, H. Bekker, H.J.C. Berendsen, J.G.E.M. Fraaije, LINCS: a linear constraint solver for molecular simulations, J. Comput. Chem., 18 (1997) 1463-1472.
[142] D.V.D. Spoel, E. Lindahl, B. Hess, G. Groenhof, A.E. Mark, H.J.C. Berendsen, GROMACS: Fast, flexible, and free, J. Comp. Chem., 2005 (2005) 1701-1718.
[143] Q. Fu, M.M. Shaik, Y. Cai, F. Ghantous, A. Piai, H. Peng, S. Rits-Volloch, Z. Liu, S.C. Harrison, M.S. Seaman, B. Chen, J.J. Chou, Structure of the membrane proximal external region of HIV-1 envelope glycoprotein, Proc. Natl. Acad. Sci. U.S.A., 115 (2018) E8892.

[144] S.C. Chiliveri, J.M. Louis, R. Ghirlando, J.L. Baber, A. Bax, Tilted, Uninterrupted, Monomeric HIV-1 gp41 Transmembrane Helix from Residual Dipolar Couplings, J. Am. Chem. Soc., 140 (2018) 34-37.
[145] C. Aisenbrey, O. Rifi, B. Bechinger, Structure, membrane topology and influence of cholesterol of the membrane proximal region: transmembrane helical anchor sequence of gp41 from HIV, Sci. Rep., 10 (2020) 22278.
[146] D. Huster, X.L. Yao, M. Hong, Membrane Protein Topology Probed by 1H Spin Diffusion from Lipids Using Solid-State NMR Spectroscopy, J. Am. Chem. Soc., 124 (2002) 874-883.
[147] M. Hong, K. Schmidt-Rohr, Magic-angle-spinning NMR techniques for measuring long-range distances in biological macromolecules, Acc. Chem. Res., 46 (2013) 2154-2163.
[148] E.B. Sirota, G.S. Smith, C.R. Safinya, R.J. Plano, N.A. Clark, X-ray Scattering Studies of Aligned, Stacked Surfactant Membranes, Science, 242 (1988) 1406-1409.
[149] M.R. Elkins, J.K. Williams, M.D. Gelenter, P. Dai, B. Kwon, I.V. Sergeyev, B.L. Pentelute, M. Hong, Cholesterol-binding site of the influenza M2 protein in lipid bilayers from solid-state NMR, Proc. Natl. Acad. Sci. U.S.A, 114 (2017) 12946-12951.
[150] M.R. Elkins, I.V. Sergeyev, M. Hong, Determining Cholesterol Binding to Membrane Proteins by Cholesterol (13)C Labeling in Yeast and Dynamic Nuclear Polarization NMR, J. Am. Chem. Soc., 140 (2018) 15437-15449.
[151] B. Gorai, A.K. Sahoo, A. Srivastava, N.M. Dixit, P.K. Maiti, Concerted Interactions between Multiple gp41 Trimers and the Target Cell Lipidome May Be Required for HIV-1 Entry, J. Chem. Inf. Model., 61 (2021) 444-454.
[152] R.F.M. de Almeida, A. Fedorov, M. Prieto, Sphingomyelin/Phosphatidylcholine/Cholesterol Phase Diagram: Boundaries and Composition of Lipid Rafts, Biophys. J., 85 (2003) 2406-2416.
[153] S.L. Veatch, S.L. Keller, Seeing spots: Complex phase behavior in simple membranes, Biochim. Biophys. Acta, 1746 (2005) 172-185.
[154] G.W. Feigenson, Phase diagrams and lipid domains in multicomponent lipid bilayer mixtures, Biochim. Biophys. Acta - Biomem., 1788 (2009) 47-52.
[155] F.J.-M.d. Meyer, A. Benjamini, J.M. Rodgers, Y. Misteli, B. Smit, Molecular Simulation of the DMPC-Cholesterol Phase Diagram, J. Phys. Chem. B, 114 (2010) 10451-10461.
[156] V. Corradi, E. Mendez-Villuendaas, H.I. Ingolfsson, R. Gu, I. Siuda, M.N. Melo, A. Moussatova, L.J. DeGagne, B.I. Sejdiu, G. Singh, T.A. Wassenaar, K.D. Magnero, S.J. Marrink, D.P. Tieleman, Lipid−Protein Interactions Are Unique Fingerprints for Membrane Proteins, ACS Central Sci., 4 (2018) 709-717.
[157] S.C. Chiliveri, J.M. Louis, A. Bax, Concentration-Dependent Structural Transition of the HIV-1 gp41 MPER Peptide into α-Helical Trimers, Angew. Chem. Int. Ed., 60 (2021) 166-170.
[158] M.R. Elkins, A. Bandara, G.A. Pantelopulos, J.E. Straub, M. Hong, Direct Observation of Cholesterol Dimers and Tetramers in Lipid Bilayers, J. Phys. Chem. B, 125 (2021) 1825-1837.
[159] F. Campelo, H.T. McMahon, M.M. Kozlov, The Hydrophobic Insertion Mechanism of Membrane Curvature Generation by Proteins, Biophys. J., 95 (2008) 2325-2339.

[160] T. Mandal, S.E. Spagnolie, A. Audhya, Q. Cui, Protein Induced Membrane Curvature in Coarse-Grained Simulations: Binding Interface, Insertion Depth and Lipid Spontaneous Curvature, Biophys. J., 120 (2021) 3211-3221.
[161] M. Hong, W.F. DeGrado, Structural basis for proton conduction and inhibition by the influenza M2 protein, Protein science : a publication of the Protein Society, 21 (2012) 1620-1633.
[162] L.H. Pinto, L.J. Holsinger, R.A. Lamb, Influenza virus M2 protein has ion channel activity, Cell, 69 (1992) 517-528.
[163] L.H. Pinto, R.A. Lamb, The M2 proton channels of influenza A and B viruses, The Journal of biological chemistry, 281 (2006) 8997-9000.
[164] C. Wang, R.A. Lamb, L.H. Pinto, Activation of the M2 ion channel of influenza virus: a role for the transmembrane domain histidine residue, Biophys. J., 69 (1995) 1363-1371.
[165] Y. Tang, F. Zaitseva, R.A. Lamb, L.H. Pinto, The Gate of the Influenza Virus M2 Proton Channel Is Formed by a Single Tryptophan Residue, The Journal of biological chemistry, 277 (2002) 39880-39886.
[166] L.H. Pinto, G.R. Dieckmann, C.S. Gandhi, C.G. Papworth, J. Braman, M.A. Shaughnessy, J.D. Lear, R.A. Lamb, W.F. DeGrado, A functionally defined model for the M2 proton channel of influenza A virus suggests a mechanism for its ion selectivity, Proc. Natl. Acad. Sci. USA, 94 (1997) 11301-11306.
[167] F. Hu, W. Luo, M. Hong, Mechanisms of proton conduction and gating by influenza M2 proton channels from solid-state NMR, Science, 330 (2010) 505-508.
[168] F. Hu, K. Schmidt-Rohr, M. Hong, NMR detection of pH-dependent histidine-water proton exchange reveals the conduction mechanism of a transmembrane proton channel, J. Am. Chem. Soc,, 134 (2012) 3703-3713.
[169] J. Hu, R. Fu, K. Nishimura, L. Zhang, H.X. Zhou, D.D. Busath, V. Vijayvergiya, T.A. Cross, Histidines, heart of the hydrogen ion channel from influenza A virus: toward an understanding of conductance and proton selectivity, Proc. Natl. Acad. Sci. U.S.A., 103 (2006) 6865-6870.
[170] C. Li, M. Yi, J. Hu, H.X. Zhou, T.A. Cross, Solid-state NMR and MD simulations of the antiviral drug amantadine solubilized in DMPC bilayers, Biophys. J., 94 (2008) 1295-1302.
[171] Y. Miao, H. Qin, R. Fu, M. Sharma, T.V. Can, I. Hung, S. Luca, P.L. Gor'kov, W.W. Brey, T.A. Cross, M2 proton channel structural validation from full-length protein samples in synthetic bilayers and E. coli membranes, Angew. Chem. Int. Ed. Engl. , 51 (2012) 8383-8386.
[172] S.D. Cady, K. Schmidt-Rohr, J. Wang, C.S. Soto, W.F. Degrado, M. Hong, Structure of the amantadine binding site of influenza M2 proton channels in lipid bilayers, Nature, 463 (2010) 689-692.
[173] Y. Ohigashi, C. Ma, X. Jing, V. Balannick, L.H. Pinto, R.A. Lamb, An amantadine-sensitive chimeric BM2 ion channel of influenza B virus has implications for the mechanism of drug inhibition, Proc. Natl. Acad. Sci. U. S. A., 106 (2009) 18775-18779.
[174] A.L. Stouffer, R. Acharya, D. Salom, A.S. Levine, L. Di Costanzo, C.S. Soto, V. Tereshko, V. Nanda, S. Stayrook, W.F. DeGrado, Structural basis for the function and inhibition of an influenza virus proton channel, Nature, 451 (2008) 596-599.

[175] S.D. Cady, T.V. Mishanina, M. Hong, Structure of amantadine-bound M2 transmembrane peptide of influenza A in lipid bilayers from magic-angle-spinning solid-state NMR: the role of Ser31 in amantadine binding, J. Mol. Biol., 385 (2009) 1127-1141.
[176] S.D. Cady, J. Wang, Y. Wu, W.F. DeGrado, M. Hong, Specific binding of adamantane drugs and direction of their polar amines in the pore of the influenza M2 transmembrane domain in lipid bilayers and dodecylphosphocholine micelles determined by NMR spectroscopy J. Am. Chem. Soc., 133 (2011) 4274-4284.
[177] L.B. Andreas, A.B. Barnes, B. Corzilius, J.J. Chou, E.A. Miller, M. Caporini, M. Rosay, R.G. Griffin, Dynamic nuclear polarization study of inhibitor binding to the M2(18-60) proton transporter from influenza A, Biochemistry, 52 (2013) 2774-2782.
[178] J.S. Rossman, X. Jing, G.P. Leser, R.A. Lamb, Influenza virus M2 protein mediates ESCRT-independent membrane scission, Cell, 142 (2010) 902-913.
[179] E.A. Bruce, L. Medcalf, C.M. Crump, S.L. Noton, A.D. Stuart, H.M. Wise, D. Elton, K. Bowers, P. Digard, Budding of filamentous and non-filamentous influenza A virus occurs via a VPS4 and VPS28-independent pathway, Virology, 390 (2009) 268-278.
[180] B.J. Chen, R.A. Lamb, Mechanisms for enveloped virus budding: can some viruses do without an ESCRT?, Virology, 372 (2008) 221-232.
[181] J. Paulino, X. Pang, I. Hung, H.X. Zhou, T.A. Cross, Influenza A M2 Channel Clustering at High Protein/Lipid Ratios: Viral Budding Implications, Biophys J, 116 (2019) 1075-1084.
[182] C. Schroeder, H. Heider, E. Möncke-Buchner, T.I. Lin, The influenza virus ion channel and maturation cofactor M2 is a cholesterol-binding protein, Eur Biophys J, 34 (2005) 52-66.
[183] M.R. Elkins, I.V. Sergeyev, M. Hong, Determining Cholesterol Binding to Membrane Proteins by Cholesterol (13)C Labeling in Yeast and Dynamic Nuclear Polarization NMR, J Am Chem Soc, 140 (2018) 15437-15449.
[184] M.R. Elkins, J.K. Williams, M.D. Gelenter, P. Dai, B. Kwon, I.V. Sergeyev, B.L. Pentelute, M. Hong, Cholesterol-binding site of the influenza M2 protein in lipid bilayers from solid-state NMR, Proc. Natl. Acad. Sci. U. S. A., 114 (2017) 12946-12951.
[185] E.V. Ekanayake, R. Fu, T.A. Cross, Structural Influences: Cholesterol, Drug, and Proton Binding to Full-Length Influenza A M2 Protein, Biophys J, 110 (2016) 1391-1399.
[186] J.L. Kitevski-LeBlanc, R.S. Prosser, Current applications of 19F NMR to studies of protein structure and dynamics, Prog. Nucl. Magn. Reson. Spectrosc., 62 (2012) 1-33.
[187] N.G. Sharaf, A.M. Gronenborn, 19F-Modified Proteins and 19F-Containing Ligands as Tools in Solution NMR Studies of Protein Interactions, in: Z. Kelman (Ed.) Methods in Enzymology, vol. 565, Academic Press, 2015, pp. 67-95.
[188] M. Roos, V.S. Mandala, M. Hong, Determination of Long-Range Distances by Fast Magic-Angle-Spinning Radiofrequency-Driven (19)F-(19)F Dipolar Recoupling NMR, J. Phys. Chem. B, 122 (2018) 9302-9313.
[189] A.A. Shcherbakov, M. Hong, Rapid Measurement of Long-Range Distances in Proteins by Multidimensional 13C-19F REDOR NMR under Fast Magic-Angle Spinning, J. Biomol. NMR., 71 (2018) 31-43.
[190] A.A. Shcherbakov, V.S. Mandala, M. Hong, High-Sensitivity Detection of Nanometer 1H-19F Distances for Protein Structure Determination by 1H-Detected Fast MAS NMR, J. Phys. Chem. B., 123 (2019) 4387-4391.

[191] A.A. Shcherbakov, J. Medeiros-Silva, N. Tran, M.D. Gelenter, M. Hong, From Angstroms to Nanometers: Measuring Interatomic Distances in Solid-State NMR, Chem. Rev., in press (2022).
[192] M. Lu, M. Wang, I.V. Sergeyev, C.M. Quinn, J. Struppe, M. Rosay, W. Maas, A.M. Gronenborn, T. Polenova, (19)F Dynamic Nuclear Polarization at Fast Magic Angle Spinning for NMR of HIV-1 Capsid Protein Assemblies, J. Am. Chem. Soc., 141 (2019) 5681-5691.
[193] M. Wang, M. Lu, M. Fritz, C. Quinn, I.J. Byeon, C.H. Byeon, J. Struppe, W. Maas, A.M. Gronenborn, T. Polenova, Fast Magic Angle Spinning ^{19}F NMR of HIV-1 Capsid Protein Assemblies, Angew. Chem. Int. Ed. Engl., 57 (2018) 16375-16379.
[194] D. Huster, X. Yao, M. Hong, Membrane protein topology probed by (1)H spin diffusion from lipids using solid-state NMR spectroscopy, J Am Chem Soc, 124 (2002) 874-883.
[195] M.D. Simon, P.L. Heider, A. Adamo, A.A. Vinogradov, S.K. Mong, X. Li, T. Berger, R.L. Policarpo, C. Zhang, Y. Zou, X. Liao, A.M. Spokoyny, K.F. Jensen, B.L. Pentelute, Rapid flow-based peptide synthesis, Chembiochem, 15 (2014) 713-720.
[196] M. Sharma, M. Yi, H. Dong, H. Qin, E. Peterson, D.D. Busath, H.X. Zhou, T.A. Cross, Insight into the mechanism of the influenza A proton channel from a structure in a lipid bilayer, Science, 330 (2010) 509-512.
[197] S. Huang, B. Green, M. Thompson, R. Chen, J. Thomaston, W.F. DeGrado, K.P. Howard, C-terminal juxtamembrane region of full-length M2 protein forms a membrane surface associated amphipathic helix, Protein Sci, 24 (2015) 426-429.
[198] G. Hou, S. Yan, J. Trébosc, J.P. Amoureux, T. Polenova, Broadband homonuclear correlation spectroscopy driven by combined R2(n)(v) sequences under fast magic angle spinning for NMR structural analysis of organic and biological solids, J Magn Reson, 232 (2013) 18-30.
[199] A.E. Bennett, C.M. Rienstra, M. Auger, K.V. Lakshmi, R.G. Griffin, Heteronuclear decoupling in rotating solids, J. Chem. Phys., 103 (1995) 6951-6958.
[200] J.S. Rossman, X. Jing, G.P. Leser, V. Balannik, L.H. Pinto, R.A. Lamb, Influenza virus M2 ion channel protein is necessary for filamentous virion formation, J. Virol., 84 (2010) 5078-5088.
[201] A. Martyna, B. Bahsoun, M.D. Badham, S. Srinivasan, M.J. Howard, J.S. Rossman, Membrane remodeling by the M2 amphipathic helix drives influenza virus membrane scission, Sci. Rep., 7 (2017).
[202] A. Martyna, B. Bahsoun, J.J. Madsen, F. Jackson, M.D. Badham, G.A. Voth, J.S. Rossman, Cholesterol Alters the Orientation and Activity of the Influenza Virus M2 Amphipathic Helix in the Membrane, J. Phys. Chem. B, 124 (2020) 6738-6747.
[203] P.A. Nguyen, C.S. Soto, A. Polishchuk, G.A. Caputo, C.D. Tatko, C. Ma, Y. Ohigashi, L.H. Pinto, W.F. DeGrado, K.P. Howard, pH-induced conformational change of the influenza M2 protein C-terminal domain, Biochemistry, 47 (2008) 9934-9936.
[204] S.S. Kim, M.A. Upshur, K. Saotome, I.D. Sahu, R.M. McCarrick, J.B. Feix, G.A. Lorigan, K.P. Howard, Cholesterol-Dependent Conformational Exchange of the C-Terminal Domain of the Influenza A M2 Protein, Biochemistry, 54 (2015) 7157-7167.
[205] S. Leekumjorn, A.K. Sum, Molecular characterization of gel and liquid-crystalline structures of fully hydrated POPC and POPE bilayers, J. Phys. Chem. B, 111 (2007) 6026-6033.

[206] S.D. Cady, T. Wang, M. Hong, Membrane-dependent effects of a cytoplasmic helix on the structure and drug binding of the influenza virus M2 protein, J. Am. Chem. Soc., 133 (2011) 11572-11579.
[207] P.T. Ivanova, D.S. Myers, S.B. Milne, J.L. McClaren, P.G. Thomas, H.A. Brown, Lipid composition of viral envelope of three strains of influenza virus - not all viruses are created equal, ACS Infect Dis, 1 (2015) 399-452.
[208] J. Zhang, A. Pekosz, R.A. Lamb, Influenza virus assembly and lipid raft microdomains: a role for the cytoplasmic tails of the spike glycoproteins, J Virol, 74 (2000) 4634-4644.
[209] Y. Yang, H. Yao, M. Hong, Distinguishing bicontinuous lipid cubic phases from isotropic membrane morphologies using (31)P solid-state NMR spectroscopy, J Phys Chem B, 119 (2015) 4993-5001.
[210] T. Wang, M. Hong, Investigation of the curvature induction and membrane localization of the influenza virus M2 protein using static and off-magic-angle spinning solid-state nuclear magnetic resonance of oriented bicelles, Biochemistry, 54 (2015) 2214-2226.
[211] K.C. Duong-Ly, V. Nanda, W.F. Degrado, K.P. Howard, The conformation of the pore region of the M2 proton channel depends on lipid bilayer environment, Protein Sci, 14 (2005) 856-861.
[212] K. Saotome, K.C. Duong-Ly, K.P. Howard, Influenza A M2 protein conformation depends on choice of model membrane, Biopolymers, 104 (2015) 405-411.
[213] A.L. Herneisen, I.D. Sahu, R.M. McCarrick, J.B. Feix, G.A. Lorigan, K.P. Howard, A Budding-Defective M2 Mutant Exhibits Reduced Membrane Interaction, Insensitivity to Cholesterol, and Perturbed Interdomain Coupling, Biochemistry, 56 (2017) 5955-5963.
[214] J. Pan, A. Dalzini, L. Song, Cholesterol and phosphatidylethanolamine lipids exert opposite effects on membrane modulations caused by the M2 amphipathic helix, Biochim. Biophys. Acta, 1861 (2019) 201-209.
[215] L.V. Chernomordik, M.M. Kozlov, Mechanics of membrane fusion, Nat Struct Mol Biol, 15 (2008) 675-683.
[216] L. Chernomordik, Non-bilayer lipids and biological fusion intermediates, Chem Phys Lipids, 81 (1996) 203-213.
[217] M. Melar, D.E. Ott, T.J. Hope, Physiological levels of virion-associated human immunodeficiency virus type 1 envelope induce coreceptor-dependent calcium flux, J Virol, 81 (2007) 1773-1785.
[218] I. al-Haitham, Ibn Al-Haitham: Proceedings of The Celebration of 1000th Anniversary Held Under the Auspices of Hamdard National Foundation, in: H.M. Said (Ed.) Celebration of 1000th Anniversary, Hamdard Academy, Karachi, Pakistan, 1969.